Anion Exchange Membrane Water Electrolyzer

Electrode Design, Lab-Scaled Testing System and Performance Evaluation

Xu, Qiucheng; Zhang, Liyue; Zhang, Jiahao; Wang, Jingyu; Hu, Yanjie; Jiang, Hao; Li, Chunzhong

Published in:
EnergyChem

Link to article, DOI:
10.1016/j.enchem.2022.100087

Publication date:
2022

Document Version
Publisher's PDF, also known as Version of record

EnergyChem 4 (2022) 100087

Contents lists available at ScienceDirect

EnergyChem

journal homepage: www.sciencedirect.com/journal/energychem

Anion Exchange Membrane Water Electrolyzer: Electrode Design, Lab-Scaled Testing System and Performance Evaluation

Qiucheng Xu [a,c,1,*], Liyue Zhang [a,1], Jiahao Zhang [a], Jingyu Wang [a], Yanjie Hu [a], Hao Jiang [a,b,*], Chunzhong Li [a,b,*]

[a] Key Laboratory for Ultrafine Materials of Ministry of Education, Frontiers Science Center for Materio-biology and Dynamic Chemistry, School of Materials Science and Engineering, East China University of Science and Technology, Shanghai 200237, China
[b] Shanghai Engineering Research Center of Hierarchical Nanomaterials, School of Chemical Engineering, East China University of Science and Technology, Shanghai 200237, China
[c] Surface Physics and Catalysis (Surf Cat) Section, Department of Physics, Technical University of Denmark, 2800 Kgs, Lyngby, Denmark

ARTICLE INFO

Keywords:
Anion-exchange membrane
Water electrolysis
Electrocatalysts
Gas diffusion electrode
Hydrogen evolution
Membrane electrode assembly

ABSTRACT

Green hydrogen produced by water electrolysis is one of the most promising technologies to realize the efficient utilization of intermittent renewable energy and the decarbonizing future. Among various electrolysis technologies, the emerging anion-exchange membrane water electrolysis (AEMWE) shows the most potential for producing green hydrogen at a competitive price. In this review, we demonstrate a comprehensive introduction to AEMWE including the advanced electrode design, the lab-scaled testing system establishment, and the electrochemical performance evaluation. Specifically, recent progress in developing high activity transition metal-based powder electrocatalysts and self-supporting electrodes for AEMWE is summarized. To improve the synergistic transfer behaviors between electron, charge, water, and gas inside the gas diffusion electrode (GDE), two optimizing strategies are concluded by regulating the pore structure and interfacial chemistry. Moreover, we provide a detailed guideline for establishing the AEMWE testing system and selecting the electrolyzer components. The influences of the membrane electrode assembly (MEA) technologies and operation conditions on cell performance are also discussed. Besides, diverse electrochemical methods to evaluate the activity and stability, implement the failure analyses, and realize the *in-situ* characterizations are elaborated. In end, some perspectives about the optimization of interfacial environment and cost assessments have been proposed for the development of advanced and durable AEMWE.

1. Introduction

Carbon neutrality and decarbonizing development tendency demand the construction of a new economic system based on clean and sustainable energy carriers [1–3]. Hydrogen as an ideal energy carrier with zero CO_2 emission feature shows a great application potential across heating, power supply, chemical industry, and transportation [4–6]. Currently, the incumbent technology for hydrogen production is natural gas reforming and coal gasification, however, they still rely on consuming fossil fuels and thus cause environmental pollution and abundant CO_2 emission [7,8]. On the other hand, hydrogen produced by water electrolysis *via* intermittent renewable energy (*e.g.*, solar, wind, geotherm, *etc.*) is one promising and alternative technical route [9,10]. To realize the price advantages of hydrogen from water electrolysis compared to traditional methods, many countries, such as the United States, Germany, China, *etc.*, have consecutively deployed the 'Hydrogen Development White Papers' to guide the domestic technology and industry development [11,12]. Some well-known international or national projects, such as the FCH JU projects from the EU, Hydrogen program from U.S. DOE, have achieved initial success [13,14].

Before discussing the state of art technologies, the development history of water electrolysis is briefly introduced, as displayed in Scheme 1. As early as 1789, Adriaan *et al.* used an electrostatic generator to decompose the water into hydrogen and oxygen, firstly realizing the generation of H_2 from electricity [15]. Afterwards, water-splitting reactions and electrolysis reactors were widely studied at the end of the

* Corresponding authors:
E-mail addresses: qiuxu@dtu.dk (Q. Xu), jianghao@ecust.edu.cn (H. Jiang), czli@ecust.edu.cn (C. Li).
[1] These authors contributed equally.

https://doi.org/10.1016/j.enchem.2022.100087

Available online 4 August 2022

19th century due to the vogue of electrochemistry. Starting from the mid-20th century, with the increasing demand for H_2 in the chemical industry, alkaline water electrolysis (AWE) became industrial commercialization; however, they were only utilized for a short period and then quickly displaced by the petrochemical industry. Because of the low market requirement, the water electrolysis technology was quiet and slowly developed for decades. In 1965, the new era of proton-exchange membrane (PEM) based water electrolysis begins [16]. With the evocation of using renewable energies at the initial of the 21st century, the PEM becomes famous due to its unique advantage of direct producing high pure and pressured hydrogen. In this decade, the anion-exchange membrane (AEM) started to be applied in water electrolysis. Nowadays, advanced water electrolysis technologies are competing in the same race for realizing carbon neutrality and a sustainable future.

As mentioned above, three main low-temperature water electrolysis technologies (*i.e.*, AWE, PEMWE, AEMWE) have been developed. Table 1 gives their technical parameters comparison. AWE is a mature technology with a long history. It employs a porous diaphragm membrane to separate the anode and cathode in the 30-40% KOH electrolyte [17]. Due to the high alkaline operating environment, it allows using the Ni plates as current collectors and noble metal-free materials as electrodes, thus enabling a low hardware cost and long durability (> 100000 h). However, it also has the drawbacks such as a low operating current density (< 0.5 A cm^{-2}) and the inability to produce high purity and pressured gas products. Commonly, the produced gas contains alkaline liquid and water vapor, which requires elimination by auxiliary equipment. Besides, it is difficult for AWE to start up quickly or change the load to adjust the speed of hydrogen production quickly, so it is poorly adapted to renewable energy generation (e.g., wind power generation, photovoltaic power generation). The PEMWE technology by using a solid polymer electrolyte allows for directly producing the high pure H_2 at high current density (~ 2 A cm^{-2}) in high-pressure working conditions from pure water [18]. Proton exchange membrane as a separator realizes the compact system design to largely reduce the ohmic loss across the electrolyzer, whereas it also provides a strong acidic interfacial environment so that the platinum group metals (PGM)-based catalysts and titanium-based bipolar plates (BPPs) are required. On the other hand, PEMWE operation is more flexible than AWE and can be powered by intermittent discontinuous renewable energy sources such as wind power and photovoltaic power. In the past decade, PEMWE to hydrogen products have been launched in the EU, the US and Japan to promote their application. However, PEMWE technology is only for small-scale applications due to its high initial capital expenditure and short investigated durability (< 10 kh) [19]. AEMWE technology is likely the combination of these two technologies, which employs an anion exchange membrane as a separator to provide an alkaline interfacial environment [20,21]. In principle, it allows for the utilization of the cost-efficient catalysts and hardware as the AWE and it can produce high-quality H_2 at a high current level as the PEMWE, thus showing a great promising future [22]. Since the AEMWE just emerged this decade, more efforts based on the materials design, component optimization and performance evaluation still need to be developed to make it competitive commercially.

Table 1
Comparison of the detailed technical parameters for AWE, PEMWE and AEMWE.

	AWE	PEMWE	AEMWE
Separation	Diaphragm (*e.g.*, Zirfon)	Proton exchange membrane (*e.g.*, Nafion)	Anion exchange membrane (*e.g.*, Sustinion)
Cathode	NiMo-based alloys	PGMs	Transition metal-based materials
Anode	NiCo-based alloys	IrO_x, RuO_x	Transition metal-based materials
Current collector	Ni plate	Copper plate	Copper plate
Bipolar plate	/	Graphite and Ti plate	Ni or Stainless Steel plate
Electrolyte	30-40 wt% KOH	Pure water	Pure water, alkali solution
Current density	< 0.5 A cm^{-2}	1~2 A cm^{-2}	1~2 A cm^{-2}
Operating temperature	60-90 °C	50-90 °C	40-80 °C
Gas purity	> 99.5%	> 99.999%	> 99.99%
Lifetime	~ 100 kh	< 10 kh	< 2 kh
Estimated cost	Low	High	Not available
Technology status	Mature	Commercial for small-scale	R&D

Advanced electrocatalyst and electrode design is always the core technique for developing AEMWE [25]. Due to the affinity, the applied electrode materials are generally achieved from the alkaline water-splitting reaction and optionally tested in the three-electrode configuration (*e.g.*, powder catalyst by rotating disk electrodes or substrate catalyst by electrode holder). However, many studies have pointed out the challenges of direct transmission of three-electrode cell achievements (activity & stability) to the two-electrode electrolyzer due to their discrepancy of interfacial environment and mass transfer [23, 26]. As shown in Fig. 1, the central component in the electrolyzer configuration is membrane electrode assembly (MEA), which is a layered structure where the membrane is sandwiched between two porous transport layers (PTL) with the coated anode or cathode catalysts. The function of PTL is to ensure the efficient mass transport of

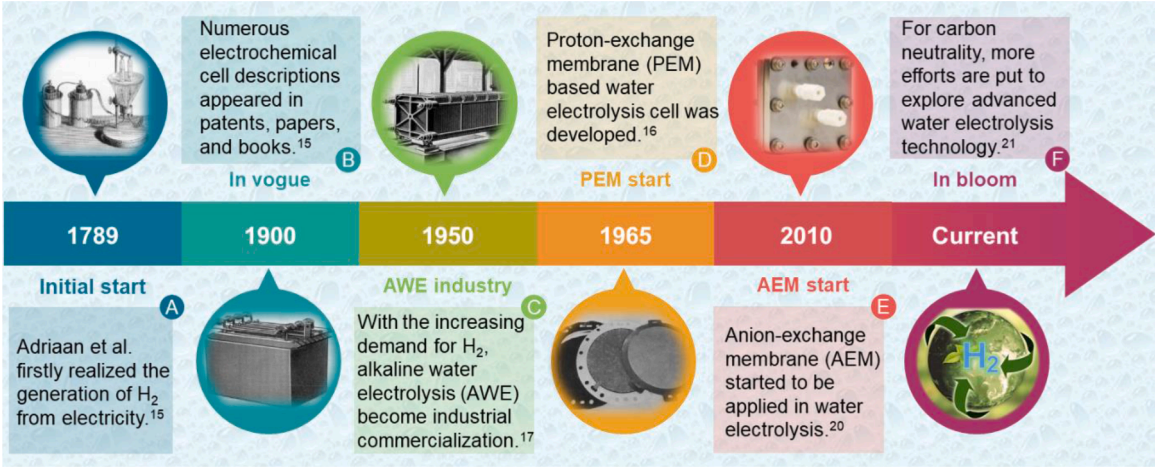

Scheme 1. The timeline for developing low-temperature water electrolysis technology. Inset images reproduced with permission. Reproduced with permission.[15] Copyright 2022, Elsevier.

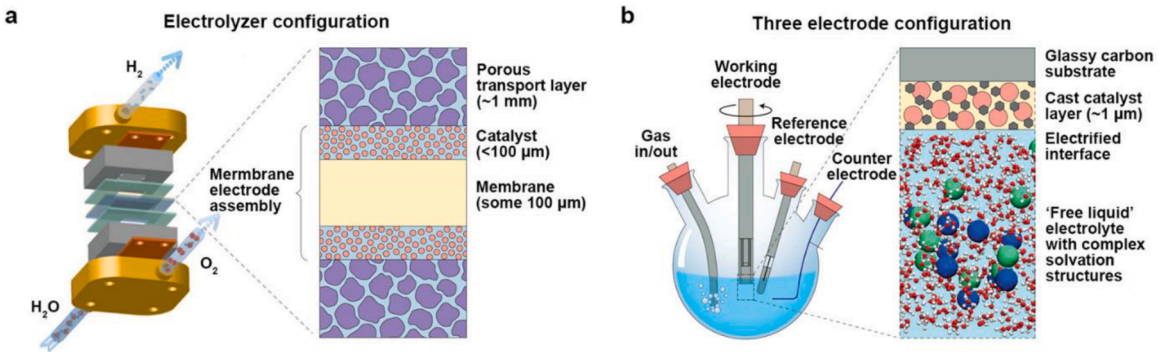

Fig. 1. Schematic of (a) the two-electrode electrolyzer configuration and (b) the three-electrode electrolyte configuration for performance evaluation. Reproduced with permission.[23] Copyright 2020, Springer Nature. Reproduced with permission.[24] Copyright 2020, American Association for the Advancement of Science.

water towards the catalyst layer (thickness of < 100 μm) and gas products away, thus the MEA allows for a much larger operating current density (~ 2 A cm^{-2}) than that of in the three-electrode configuration (~ 0.2 A cm^{-2}). This operation difference causes the poor transferability of performance at a large current [27]. Besides, the OH^- supply and transfer are also incomparable. For the three-electrode configuration, a thin catalyst layer (~ 1 μm) was deposited on the conductive substrate and then immersed in the electrolyte (*e.g.*, 1 M KOH), providing an optimal OH^- supply environment for exploring the intrinsic activity of the catalyst. However, the AEMWE in pure water operates a more rigorous reacting process that the OH- is *in-situ* generated by water dissociation at the cathode and then transfer *via* the ion-conducting polymers (ionomer and membrane) to the anode for oxygen evolution reaction (OER). Such a process depends on the combined behaviors of all components inside the MEA and thus it is much more complicated. As a result, the performance obtained in the alkaline electrolyte cell at a low current density range is more promising than those measured in a pure water AEM electrolyzer [28]. Based on those diverse features, we strongly advocate the community in the alkaline water-splitting field to use the MEA-based electrolyzer to implement the measurement in the early stages of catalyst, electrode, and other components development. However, to our knowledge, there is still a lack the related reviews to guide the establishment of the AEM testing system and benchmark the performance evaluation.

In this review, we thus provide a comprehensive introduction to AEMWE including the advanced electrode design, the lab-scaled testing setup establishment, and the electrochemical performance evaluation. Recent progress in developing the advanced transition metal-based powder electrocatalysts and self-supporting electrodes for AEMWE is firstly summarized. Afterward, two optimizing strategies of gas diffusion electrode (GDE) by regulating the pore structure and interfacial structure are concluded based on its interior synergistic transfer behavior. Importantly, we provide a detailed guideline for establishing the AEMWE testing system, selecting components inside the electrolyzer, customizing the spray-coating setup, etc. The influence of the MEA technologies and operation conditions on cell performance are also discussed. Furthermore, the electrochemical analysis methods, the performance evaluation protocols, and *in-situ* characterizations of AEMWE are elaborated. In end, some perspectives and critical suggestions are proposed for the further development of AEMWE.

2. High-efficiency AEM electrocatalysts/electrodes

AEM water electrolysis is similar to the alkaline water splitting reaction but more complex. Generally, water is provided at the cathode side and undergoes the hydrogen evolution reaction (HER) to generate H_2 and OH^-. Subsequently, the OH^- spontaneously diffuses across the AEM to the anode side for the oxygen evolution reaction (OER). The corresponding reaction formulas are shown in the below Equation (1–3). The thermodynamic potential for the overall reaction is ~1.23 V (at 25 °C). In practice, a much higher cell voltage is required to overcome the various polarizations caused by the reaction, resistance, mass transfer, *etc.*

$$\text{Anode: } 4OH^- \rightarrow O_2 + 2H_2O + 4e^- \quad (1)$$

$$\text{Cathode: } 4H_2O + 4e^- \rightarrow 2H_2 + 4OH^- \quad (2)$$

$$\text{Overall: } 2H_2O \rightarrow 2H_2 + O_2 \quad (3)$$

Electrocatalysts are used to decrease the reaction overpotentials by overcoming the intrinsic activation barrier [29,30]. The promising electrocatalysts for AEMWE require excellent activity, high-current-density tolerance, and long-term operational lifetime, while their natural abundance and preparation cost should also be considered. Additionally, the reasonable design of electrode structure is also important, which will directly affect the mass transfer and reacting interface during the electrolysis process. In this context, the transition metal-based materials (including powdery and self-supported catalysts) are firstly summarized to overcome the activity limitation of HER/OER, and then the design strategies regarding the pore structure, interface chemistry and so forth for high-efficient AEMWE are also elucidated.

2.1. Powdery transition metal electrocatalysts

Membrane-based water electrolysis has developed many MEA methods. Among them, the most mature method is the catalyst-coated substrate (CCS) technique. It requires evenly loading the powdery electrocatalysts onto the gas diffusion electrode. Due to the alkaline interfacial conditions, the AEMWE enables inexpensive transition metal-based materials (TMMs) and thus exhibits impressive economic and stability advantages. Numerous research works have been devoted to developing and applying the TMMs electrocatalysts. In this section, we summarized the recent progress of TMMs-based powdery as HER or OER electrocatalysts for the AEMWE, as shown in Table 2.

2.1.1. Powdery OER electrocatalysts

Oxygen evolution reaction has been considered a pivotal bottleneck in electrochemical water splitting, which possesses sluggish kinetics because of the four protons coupled electrons transfer process, resulting in a large reacting overpotential [31,32]. This inevitably enhances the electricity consumption and impedes the overall water splitting efficiency. Therefore, the interest in exploring cost-effective and high-efficient transition metal-based OER electrocatalysts has been aroused in recent years.

Transition metal oxides, such as the spinel family and the perovskite family, have been verified to have remarkable OER catalytic activity. This can be attributed to their flexible oxidation states and various coordination structures of metal centers, leading to the adjustable OER behavior [33,34]. Furthermore, transition metal oxides also have the

Table 2
The AWEME performance summary of the powdery transition metal electrocatalysts.

Type	Catalyst	Gas diffusion layer	Counter electrode	Testing conditions	Activity	Stability	Ref.
OER	$Cu_{0.95}Co_{2.05}O_4$	Ni foam	Pt-C/Carbon cloth	1 M KOH at 50 °C	1.54 A cm^{-2} at 1.8 V	500 mA cm^{-2} for 100 hrs	[37]
	$Cu_{0.5}Co_{2.5}O_4$	Ni foam	Pt-C/Carbon cloth	1 M KOH at 50 °C	1.3 A cm^{-2} at 1.8 V	400 mA cm^{-2} for 100 hrs	[38]
	$Ni_{0.9}Fe_{0.1}Co_{1.975}Li_{0.025}O_4$	Ni foam	Ni foam	10 wt% KOH at 50 °C	143 mA cm^{-2} at 1.85 V	225 mA cm^{-2} for 17 days	[61]
	NiFe-LDH	Carbon paper	Pt-C/Carbon paper	1 M KOH at 80 °C	1 A cm^{-2} at 1.59 V	1 A cm^{-2} for 6 hrs	[39]
	NiFe-LDH	Ni foam	Pt-C/Carbon paper	1 M KOH at 50 °C	1 A cm^{-2} at 1.7 V	1 A cm^{-2} for 50 hrs	[40]
	Cr-NiFe-LDH	Ni foam	NiMoCo/Ni foam	1 M KOH at 40 °C	1 A cm^{-2} at 2.11 V	1 A cm^{-2} for 50 hrs	[62]
	Fe-$NiMoN_x$	Carbon paper	$NiMoN_x$/Carbon paper	1 M KOH at 20 °C	1 A cm^{-2} at 1.77 V	500 mA cm^{-2} for 25 hrs	[50]
	$(NiCo)_3Se_4$	Ni foam	Pt-C/Carbon paper	1 M KOH at 60 °C	2 A cm^{-2} at 2.0 V	1 A cm^{-2} for 95 hrs	[41]
HER	NiCo/rGO	Carbon cloth	Co_3O_4-rGO/Carbon cloth	1 M KOH at 25 °C	100 mA cm^{-2} at 1.9 V	100 mA cm^{-2} for 10 hrs	[57]
	Ni-Fe-Co	Ni foam	Ni-Fe-O_x/Ni foam	1 M KOH at 60 °C	1 A cm^{-2} at 1.9 V	1 A cm^{-2} for 100 hrs	[63]
	NiCoO-NiCo/C	Carbon cloth	CuCoO/Ni foam	1 M KOH at 50 °C	504 mA cm^{-2} at 1.85 V	440 mA cm^{-2} for 10 hrs	[60]
	NiCu MMO/C	Carbon paper	Ir black/Au coated-Ti felt	1 M KOH at 50 °C	1.85 A cm^{-2} at 2.0 V	-	[64]

advantages of low cost, environmental friendliness and excellent alkali resistance, attracting many researchers to focus on their AEMWE application [35,36]. For instance, Kwon *et al.* developed a series of CuCo-based oxides by adjusting the Cu/Co ratio, in which the $Cu_{0.95}Co_{2.05}O_4$ sample with the highest ratio of Co^{3+} active center showed a prominent activity of 1.54 A cm^{-2} at 1.8 V in a single AEMWE cell [37]. Additionally, the spinel structure ensures superior alkali stability, performing impressive long-term stability at a high current density (500 mA cm^{-2}) over 100 h. Jang *et al.* designed a $Cu_{0.5}Co_{2.5}O_4$ nanowall electrocatalyst stacked with nanoscale particles (3-4 nm) by regulating the pH value during the co-precipitation process [38]. The nanosized structure provides the large electrochemically active surface area and fast bubble diffusion kinetics, endowing $Cu_{0.5}Co_{2.5}O_4$ electrode an excellent anodic catalytic activity of 1.3 A cm^{-2} at 1.8 V_{cell}. DFT

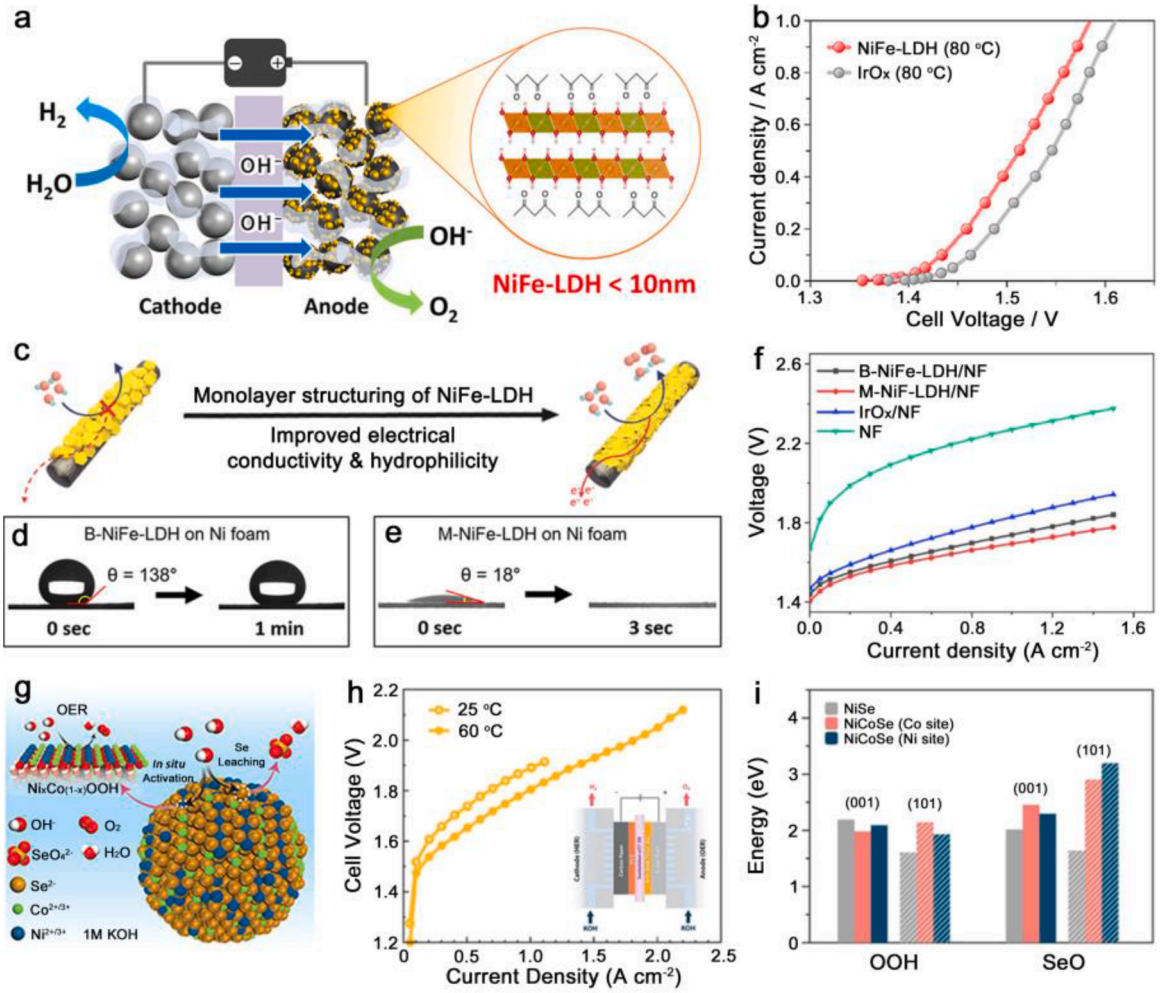

Fig. 2. (a) Schematic illustration of the NiFe-LDH structure and its application in an AEMWE cell. (b) Polarization curves of the NiFe-LDH and commercial IrO_x in AEMWE operation. Reproduced with permission.[39] Copyright 2020, American Chemical Society. (c) The design strategy of monolayer NiFe-LDH electrode. (d, e) Surface wettability of the bulk NiFe-LDH and monolayer NiFe-LDH. (f) Polarization curves of bulk NiFe-LDH/NF, monolayer NiFe-LDH/NF, IrO_x/NF and bare Ni foam in AEMWE operation. Reproduced with permission.[40] Copyright 2021, American Chemical Society. (g) Schematic illustration of the activation process for $(NiCo)_3Se_4$ alloys. (h) Polarization curves of activated $(NiCo)_3Se_4$ in AEMWE cell. (i) Energy comparisons of OOH formation and SeO desorption on (001) and (101) lattice plane. Reproduced with permission.[41] Copyright 2021, Wiley-VCH.

calculations disclose that the incorporation of Cu enables the Co sites an optimal adsorption strength for O*, thus effectively reducing the energy barrier of OH* → O* rate-determined step and imparting Co active sites the boosted OER catalytic activity.

Transition metal (oxy)hydroxides have also been demonstrated to exhibit remarkable OER electrocatalytic activity and commercial prospects for the AEMWE system [42,43]. Especially for NiFe-based (oxy) hydroxides, whose Ni sites have a strong OH^- bonding ability and Fe sites exhibit the optimal oxygen-containing intermediates adsorption, stand at the top of the OER performance volcano plot [44–46]. Recently, numerous researchers are aimed to reduce the thickness of 2D NiFe-based (oxy)hydroxides. For example, Koshikawa *et al.* constructed NiFe-LDH with a lateral size of < 10 nm (Fig. 2a) by adopting an acetylacetone (AcAc) chelating agent for suppressing excessive growth of the LDH crystal [39]. When the as-prepared NiFe-LDH is spray-coated on carbon paper to apply as an anode for AEMWE, the filmy catalyst layer is conducive to promoting the feed of OH^- and reducing ohmic losses. As exhibited in Fig. 2b, the electrolyzer required an ultrasmall cell voltage of 1.59 V and an energy conversion efficiency of 74.7% at 1.0 A cm^{-2}, surpassing the IrO_2 anode and other reported non-noble metal-based catalysts. Furthermore, Jeoh *et al.* demonstrated that the monolayer NiFe-LDH exhibits super-hydrophilicity, ensuring a facile mass transport, larger specific surface area and more accessible active sites (Fig. 2c) [40]. As shown in Fig. 2d, e, the monolayer NiFe-LDH electrode absorbed a droplet of 1.0 M KOH within 3 s, whereas the bulk NiFe-LDH was more hydrophobic with contact angles of 138° after 1 min. The improved surface hydrophilicity facilitates oxygen bubble diffusion without blocking active sites. As a result, the electrolyzer with monolayer NiFe-LDH/NF anode outputted an impressive current density of 1.0 A cm^{-2} at 1.7 V (Fig. 2f) and outstanding stability for over 50 h.

It has been widely validated that most transition metal-based electrocatalysts, including oxides, nitrides, fluoride, and chalcogenides, *etc.*, would *in-situ* reconstruct into highly active (oxy)hydroxides at OER applied potential [46–49]. For example, $NiMoN_x$ pre-catalyst was synthesized by Chen *et al.* through a one-step annealing process and derived into an OER catalyst by anodic oxidation in the presence of Fe^{3+} [50]. XPS and ICP-MS analyses confirmed that the original $NiMoN_x$ catalyst underwent a phase transition, where the reconstructed amorphous surface was proven to be FeOOH and NiOOH species. These catalysts were integrated into an AEM electrolyzer, which delivered 1.0 A cm^{-2} at 1.57 V at 80 °C, outperforming the commercial electrolyzer. Moreover, Abed *et al.* revealed that the Se ions leaching from $(NiCo)_3Se_4$ structure during OER (Fig. 2g) can facilitate the formation of coordinatively unsaturated sites and the hydration of Ni/Co sites, resulting in the evolvement of active Ni-Co (oxy)hydroxides [41]. As shown in Fig. 2h, the electrocatalysts yield an outstanding oxygen evolution performance (2 A cm^{-2} at 2.0 V at 60 °C) when integrated into an AEM device. According to the DFT calculations in Fig. 2i, the transformation from SeO into OOH species on the NiCoSe surface is more favored than that on the NiSe surface, confirming that Co-doping also plays a critical role in the dynamic surface reconstruction.

2.1.2. Powdery HER electrocatalysts

Exploiting efficient and robust transition metal-based HER electrocatalysts matched with the aforementioned OER electrocatalysts is also essential [51]. Ni-based materials have been widely perceived as the most promising alternatives to commercialized PGMs due to their high reactivity and corrosion resistance in alkaline solutions [52,53]. However, single-type Ni active species could not balance the relationship of H_2O adsorption, H_2O dissociation and H* adsorption, which impedes the HER kinetics and efficiency.

Alloying is an effective strategy to trigger the synergistic effect of multiple active sites for accelerating the alkaline HER process [54]. In details, the work function difference between Ni and other transition metals can induce electron rearrangement, and thus reasonable alloying can optimize the electronic structure and M-H bond strength for Ni atoms for improving intrinsic activities [55,56]. For instance, Kamali *et al.* screened out a potential NiCo/rGO electrocatalyst with a near-optimal ΔG_{H^*} among a series of Ni-M bimetallic alloys (M: Co, Fe, Mn, Cr, Cu and Zn) [57]. Meanwhile, the fantastic cauliflower-like structure of NiCo nanoparticles with porosity and roughness contributes to high surface area and effective performance. Impressively, NiCo/rGO as the cathode showed a Pt-like activity of 1.9 V_{cell} at 100 mA cm^{-2} and satisfactory stability within 10 h of continuous operation when coupled with Co_3O_4/rGO anode. This work deepens the understanding of designing efficient HER electrocatalysts by alloying strategy, which is expected to promote the commercial applications of transition metal electrocatalysts in AEMWE.

Moreover, oxygen-incorporated Ni-based composites have been extensively studied to improve both activity and durability of electrocatalysts due to their optimized adsorption-desorption of OH^- and the high Ni-O bond dissociation energy (392 kJ mol^{-1}) [56,58,59]. NiCoO-NiCo/C was proposed as the cathode in single-cell and stack cell AEMWE systems by Park *et al.* using a polyol approach followed a partial oxidation treatment under atmospheric circumstances [60]. The lattice defects induced by Co and the fast hydrogen spillover channels generated by oxides collaborated to boost the catalytic activity of NiCoO-NiCo/C, resulting in an appealing performance. The NiCoO-NiCo/C electrode showed an excellent performance in a single cell (504 mA cm^{-2} at 1.85 V_{cell}) and even better performance in a 5-cell stack (740.23 mA cm^{-2} at 9.25 V_{stack}). At 440 mA cm^{-2}, the NiCoO-NiCo/C electrode generates high purity hydrogen (99.995%) continuously for 150 hours with a deteriorated rate of less than 2 mV_{stack} h^{-1}, demonstrating its commercial potential in AEMWE systems. These findings would provide important information into the design of transition metal electrocatalysts from the academic to industrial levels.

2.2. Self-supported transition metal electrocatalysts

Self-supported electrocatalysts, which normally represent the active materials that are *in-situ* grown on a conductive substrate, have attracted increased attention in recent years. Compared to powdery electrocatalysts, self-supported electrocatalysts circumvent the employment of organic binders (*e.g.*, Nafion or PVDF), preventing them from inhibiting the exposure of active sites and the diffusion of gas bubbles [65,66]. Such tight anchoring also effectively enhances the long-term mechanical stability of self-supported electrocatalysts and ensures the electron transfer efficiency between active materials and the substrate [67,68]. Besides, the self-supported electrocatalysts would directly serve as the gas diffusion electrodes, which can remarkably reduce the electrode preparation process and production costs. Hence, self-supported electrocatalysts are more suitable for AEMWE systems towards high current density and long operating times. In this section, we summarize the high-performance self-supported OER and HER electrocatalysts for AEMWE. As shown in Table 3, transition metal alloys, oxides and (oxy) hydroxides were mostly used for the OER, while the transition metal sulfides and phosphides were applied for the HER. It is worth mentioning that the alkaline electrolyte was utilized in most of the cases, mainly because they are essential to expose the high surface area of the self-supported electrode.

2.2.1. Self-supported OER electrocatalysts

Transition metal alloys are regarded as a promising candidate for OER electrocatalysis due to their outstanding electrical conductivity and fantastic synergistic catalysis effect among multi-metal catalysis sites [65]. For instance, López-Fernández *et al.* prepared Ni-Fe bimetallic electrodes through a magnetron sputtering technique, in which the electronic structure of NiFe alloys was optimized by controlling the Ni/Fe atomic ratio [69]. Moreover, the nano-columnar thin-film structure grown on carbon paper brings high porosity and good conformality. Consequently, the 10.1-NiFe electrode displays the highest anodic specific activity (1.1 A mg^{-1} at 2.0 V) when applied to AEMWE. Wang *et al.*

Table 3
The AWEME performance summary of the self-supported transition metal electrocatalysts.

Type	Anode catalyst	Cathode catalyst	Testing conditions	Activity	Stability	Ref.
OER	10.1-NiFe/Carbon paper	Ni/Carbon paper	1 M KOH at 40 °C	400 mA cm^{-2} at 2.0 V	400 mA cm^{-2} for 47.5 h	[65]
			1 M KOH at 60 °C	600 mA cm^{-2} at 2.0 V	-	
	NiAl/Porous SS	NiAlMo/Porous SS	1 M KOH at 60 °C	2 A cm^{-2} at 2.486 V	1 A cm^{-2} for 154 h	[70]
	NiCoTi/Ti foil	NiCoTi/Ti foil	1 M KOH at RT	180 mA cm^{-2} at 2.0 V	100 mA cm^{-2} for 13 h	[71]
	$CuCo_2O_4$/Ni foam	Pt-C/Carbon cloth	1 M KOH at 45 °C	1.4 A cm^{-2} at 1.9 V	500 mA cm^{-2} for 12 h	[72]
	$Ni_{0.75}Fe_{2.25}O_4$/Ni foam	Pt-C/Ni foam	1 M KOH at 42~45 °C	2 A cm^{-2} at 1.9 V	500 mA cm^{-2} for 21 h	[74]
	$Cu_xCo_{3-x}O_4$/Carbon paper	Ni/Carbon paper	1 M KOH at 40 °C	100 mA cm^{-2} at 2.0 V	25 mA cm^{-2} for 18 h	[105]
	1.8-CuCoO/Carbon paper	Ni/Carbon paper	1 M KOH at 40 °C	150 mA cm^{-2} at 2.0 V	25 mA cm^{-2} for 45 h	[106]
	$NiCo_2O_4$/Ni foam	Ni foam	10 wt% KOH at 50 °C	135 mA cm^{-2} at 1.85 V	225 mA cm^{-2} for 135 h	[107]
	$CoSb_2O_6$/Ni foam	Pt-C/Carbon paper	1 M KOH at 60 °C	800 mA cm^{-2} at 1.9 V	-	[73]
	CuCo-oxide/Ni foam	Pt-C/Carbon cloth	1 M KOH at 45 °C	1.39 A cm^{-2} at 1.8 V	500 mA cm^{-2} for 64 h	[37]
	NiFeV LDH/Ni foam	Pt-C/Ni foam	1 M KOH at 50 °C	2.1 A cm^{-2} at 1.8 V	500 mA cm^{-2} for 100 h	[80]
	NiFeOOH/SS paper	Pt-C/Carbon paper	1 M KOH at 70 °C	3.6 A cm^{-2} at 1.9 V	500 mA cm^{-2} for 100 h	[81]
	NiFeOOH/Carbon paper	$MoNi_4/MoO_2$/Ni foam	Ultra-pure water at 50 °C	250 mA cm^{-2} at 1.88 V	2 V for 240 h	[108]
	NiCoFe-NDA/Ni foam	Pt-C/Ni foam	0.1 M KOH at 50 °C	325 mA cm^{-2} at 1.8 V	1.8 ~ 2 V for 100 h	[84]
	NiFe LDH-NiS/Ni foam	Ni mesh	30 wt% KOH at 80 ~ 85 °C	400 mA cm^{-2} at 2.01 V	400 mA cm^{-2} for 80 h	[85]
	NiFe LDH-MoS_x/Ni-Fe foam	Pt-C/Carbon paper	1 M KOH at 60 °C	1 A cm^{-2} at 1.95 V	-	[84]
HER	$Cu_{0.81}Co_{2.19}O_4$/Ni foam	Co_3S_4/Ni foam	1 M KOH at 45 ~ 48 °C	431 mA cm^{-2} at 2.0 V	500 mA cm^{-2} for 12 h	[88]
	IrO_2/Carbon paper	Ni-Co-S/Carbon paper	1 M KOH at 50 °C	1.7 A cm^{-2} at 2.4 V	400 mA cm^{-2} for 8 h	[89]
	IrO_2/Carbon paper	Cu-Co-P/Carbon paper	1 M KOH at 50 °C	700 mA cm^{-2} at 1.9 V	500 mA cm^{-2} for 24 h	[94]
	NiFeCo LDH/Ni foam	$NiFeCoP_x$/Ni foam	1 M KOH at 50 °C	500 mA cm^{-2} at 1.72 V	500 mA cm^{-2} for 40 h	[95]
	IrO_2/Ni foam	$Fe_{0.2}Ni_{0.8}$-$P_{0.5}S_{0.5}$/Ni foam	1 M KOH at 60 °C	2.5 A cm^{-2} at 2.0 V	1 A cm^{-2} for 300 h	[96]

assembled an AEM electrolyzer based on the self-supported NiAl anode and NiAlMo cathode synthesized by the plasma-spraying strategy [70]. This low-cost electrolyzer requires only 2.49 V to achieve 2 A cm^{-2}, close to the efficiencies of commercial PEMWE systems. In addition, the rapid electrochemical deposition method has also been exploited by Ganesan *et al.* to prepare NiCoTi alloy on Ti substrate [71]. The resulting electrodes exhibit excellent catalytic activities towards alkaline HER (125 mV at 10 mA cm^{-2}) and OER (331 mV at 100 mA cm^{-2}) with outstanding long-term stability for over 150 h. This work shows the applied potential of a dual-functional electrode in the AEMWE device.

According to the Pourbaix diagram, most transition metal oxides, hydroxides and (oxy)hydroxides tend to be chemical stability in the alkaline solution under oxidation potential. Therefore, substantial research efforts have been devoted to developing self-supported electrocatalysts based on these materials for the AEMWE. For example, Park *et al. in-situ* synthesized $CuCo_2O_4$ electrocatalysts on Ni foam substrate through a two-step strategy of hydrothermal and calcination [72]. As illustrated in Fig. 3a, a unique chestnut-burr-like nanostructure is constructed, where the thorns are densely tightly packed with $CuCo_2O_4$ crystals (~ 10 nm). Benefitting from the enriching nanopores, the $CuCo_2O_4$/NF electrode gains the rapid mass transfer channels and the fully exposed active sites during the oxygen evolution process, therefore achieving an ultrahigh AEMWE current density of 1.4 A cm^{-2} at only 1.9 V_{cell}. Furthermore, Lee *et al.* demonstrated that 3D porous Ni foam could be applied to directly produce cost-effective and large-area anodes for high-performance AEM water electrolysis *via* the aqueous-phase corrosion strategy [74]. The as-prepared $Ni_{0.75}Fe_{2.25}O_4$ electrocatalysts require a super-small cell voltage of 1.9 V to deliver 2 A cm^{-2} after coupling with Pt/C, far surpassing the state-of-the-art IrO_2 catalyst and other reported AEM water electrolyzers. Density functional theory (DFT) calculations disclose that the unique surface structure and plentiful Fe^{3+} significantly reduce the OER energy barrier of $Ni_{0.75}Fe_{2.25}O_4$ nanoparticles, which play a key role in enhancing their oxygen evolution activity.

It is well known that oxygen vacancy is ubiquitous in transition metal oxides, which is of vital importance for the modulation of their valence electron structure and surface properties. Accurately regulating the concentration of oxygen vacancy can improve the conductivity of transition metal oxides and is promising to achieve the optimal surface adsorption behaviors during electrocatalysis, thus greatly improving their OER performance [75–77]. Ham *et al.* successfully constructed the tri-rutile $CoSb_2O_6$ electrocatalysts with abundant oxygen vacancies through the sol-gel method. The evolution of the Co oxidation state and coordination structure of electrocatalysts during OER were observed by the *in-situ* X-ray absorption near edge structure (XANES) spectra [73]. As exhibited in Fig. 3b-d, most Co^{2+} could be oxidized to Co^{3+} before OER potential, while the pivotal function of oxygen vacancy is to accelerate the OH^- adsorption kinetics for further converting Co^{3+} to real active site Co^{4+}. As a result, the self-supported $CoSb_2O_6$ electrode outputs an impressive current density of 800 mA cm^{-2} at 1.9 V (Fig. 3e) and provides a high AEMWE hydrogen production efficiency of 88% at 1.7 V (Fig. 3f). Besides, Park *et al.* developed a chemical etching approach for introducing enriching oxygen defects into transition metal oxides [78]. The as-prepared Cu-Co oxide electrode showed an excellent AEMWE performance (1.39 A cm^{-2} at 1.8 V_{cell}). Further first-principle calculations confirm that abundant oxygen vacancies significantly reduce the energy barrier of the rate-determined HOO* → O_2 step, making Cu-Co oxide maintain the advantages of low mass transfer resistance and easy removal of O_2 even at high current densities.

Transition metal hydroxides and (oxy)hydroxides are grown on the conductive substrate and usually possess a nanosheet or nanowire array structure, which is ideal for constructing self-supporting electrodes with large electrochemical surface area, desired wettability and fast bubble diffusion channels [79]. For instance, Lee *et al.* found that the conventional Ni foam electrode could be converted into a high-performance NiFeV LDH nanosheets array by surface corrosion under the co-existence of Fe^{3+} and V^{3+} [80]. DFT calculations indicate that vanadium is the key to enhancing the OER activity, which effectively reduces the Gibbs free energy of the potential-determined step (OH^- → *OH). Self-assembled AEM water electrolyzer can reach current densities up to 2.1 A cm^{-2} under only 1.8 V_{cell}, which is 0.9 A cm^{-2} higher than the state-of-the-art IrO_2/Pt-C electrocatalytic pair. This work provides a facile and low-cost strategy to produce high-performance anodic electrodes. For transition metal oxyhydroxide, Park *et al.* developed a unified AEMWE anodic electrode by directly electrodepositing NiFeOOH on the gas diffusion layer (GDL), resulting in a loose three-dimensional porous structure that is different from conventional electrodes [81]. Profiting from such structural features, the NiFeOOH electrode exhibits an ultra-high current density of 3.6 A cm^{-2} at the working voltage of 1.9 V, which is the highest among the reported AEMWE electrocatalysts to date.

Previous research has demonstrated that many transition metal electrocatalysts would undergo surface reconstruction during the OER activation process in alkaline electrolytes, forming low-crystallinity or

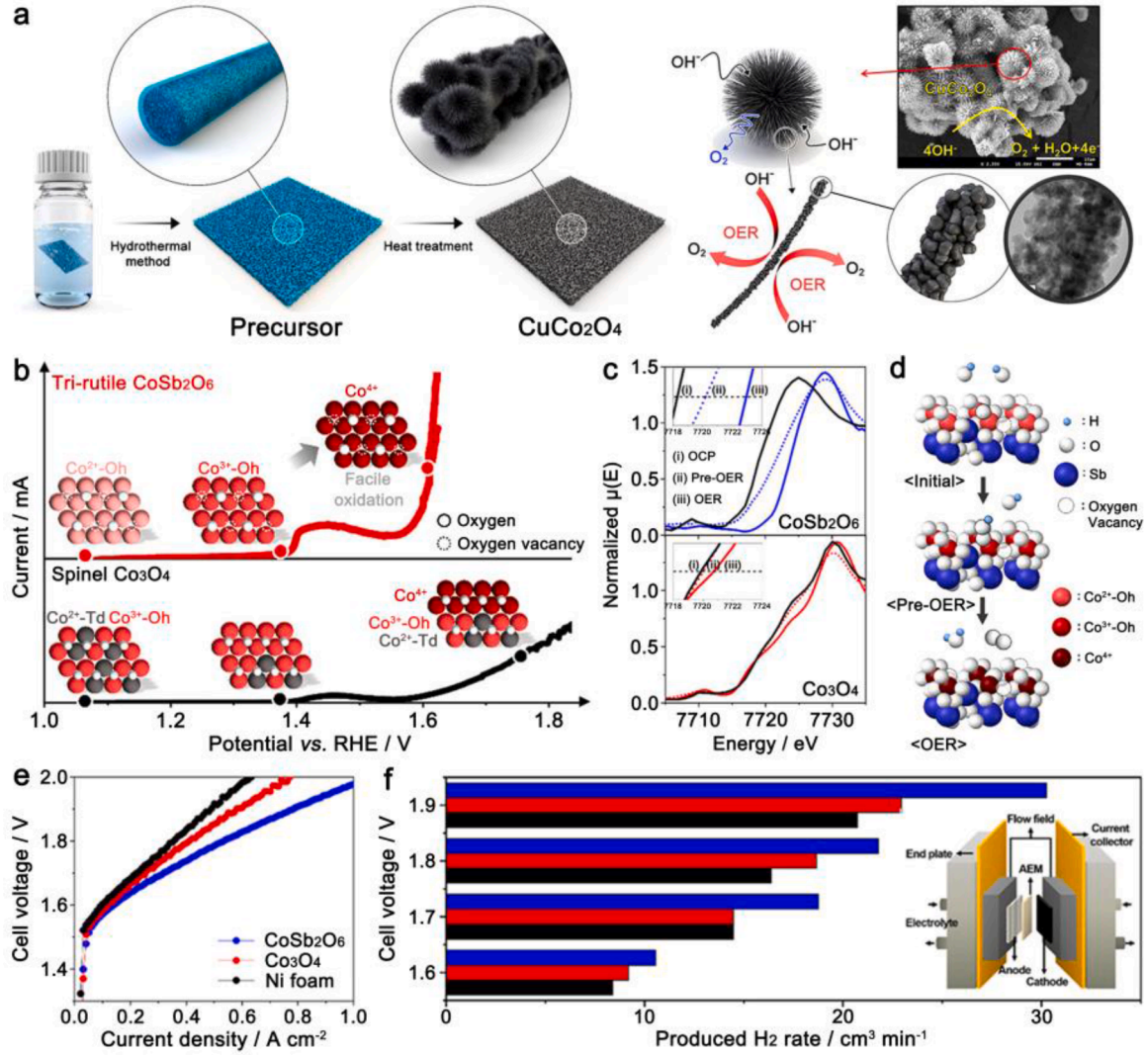

Fig. 3. (a) Schematic illustration of the synthesis for $CuCo_2O_4$/NF electrode and its chestnut-burr-like nanostructure. Reproduced with permission.[72] Copyright 2020, American Chemical Society. (b) Schematic diagram of Co oxidation state and coordination structure evolution of $CoSb_2O_6$ and Co_3O_4 during OER process. (c) *In-situ* XANES spectra in Co K-edge of $CoSb_2O_6$ and Co_3O_4. (d) Proposed scheme during increasing the anodic potential of $CoSb_2O_6$. (e) Polarization curves and (f) H_2 production rates of $CoSb_2O_6$, Co_3O_4 and bare Ni foam in AEMWE operation. Reproduced with permission.[73] Copyright 2021, American Chemical Society.

amorphous metal (oxy)hydroxides with abundant defect microstructures [82,83]. Yue *et al.* reported an ultrathin trimetallic organic framework (NiCoFe-NDA) nanosheets array as the pre-catalyst for OER, as shown in Fig. 4a. After electrochemical activation, NiCoFe-NDA was proved to have gone through the *in-situ* topological phase transformation [84]. The surface reconstructed NiCoFe-NDA inherits the nanosheets structure but triggered enriching low-coordination metal (oxy)hydroxides as the highly active species for OER. Consequently, the t-NiCoFe-NDA/NF electrode exhibited excellent catalytic properties in a home-made AEMWE, requiring only 1.8 V to realize a current output of 325 mA cm^{-2} (Fig. 4b), and can operate continuously for over 100 hours. DFT calculation results (Fig. 4c) indicate that the unsaturated surface coordination environment and the trimetallic coupling effect of NiCoFe-NDA effectively homogenize the free energy of the multi-step reaction in OER, therefore performing an outstanding activity.

Transition metal (oxy)hydroxides are also used to construct heterojunctions with metalloid transition metal compounds, such as chalcogenides, phosphides, *etc.* Their huge band energy difference induces strong electron interactions at the heterointerface, which often leads to dramatic electrocatalytic properties [83,86]. As illustrated in Fig. 4d, Wen *et al.* constructed a strongly coupled NiFe LDH/NiS Schottky heterojunction [85]. The d-band center of NiFe active species is well-tuned through interfacial charge transfer, resulting in the optimized oxygen-containing intermediate adsorption for obtaining an accelerated OER kinetics. Additionally, the ultrathin NiS nanosheet arrays can facilitate electrolyte infiltration and O_2 release even under a large current. The scaled-up NiFe LDH/NiS electrode (20 cm^2) was applied in an industrial-grade AEMWE device that can maintain a stable cell voltage of 2.01 V under an ultrahigh current of 8 A for 80 hours, saving 0.215 kWh electricity for producing per cubic meter H_2 compared with the commercial Raney Ni electrode (Fig. 4e, f). Similarly, Zhang *et al.* prepared a self-supported NiFe LDH-MoS_x hierarchical structure through solvothermal and galvanic replacement reactions [84]. The AEM water electrolyzer with NiFe LDH-MoS_x anode outputted the current density of 400 mA cm^{-2} at 1.67 V_{Cell} with an energy conversion efficiency up to 71.8%. Further research disclosed that the MoS_x component not only improves the conductivity of the self-supported electrode but also well-modulates the electronic configuration of NiFe LDH, endowing it with a significantly enhanced oxygen evolution activity.

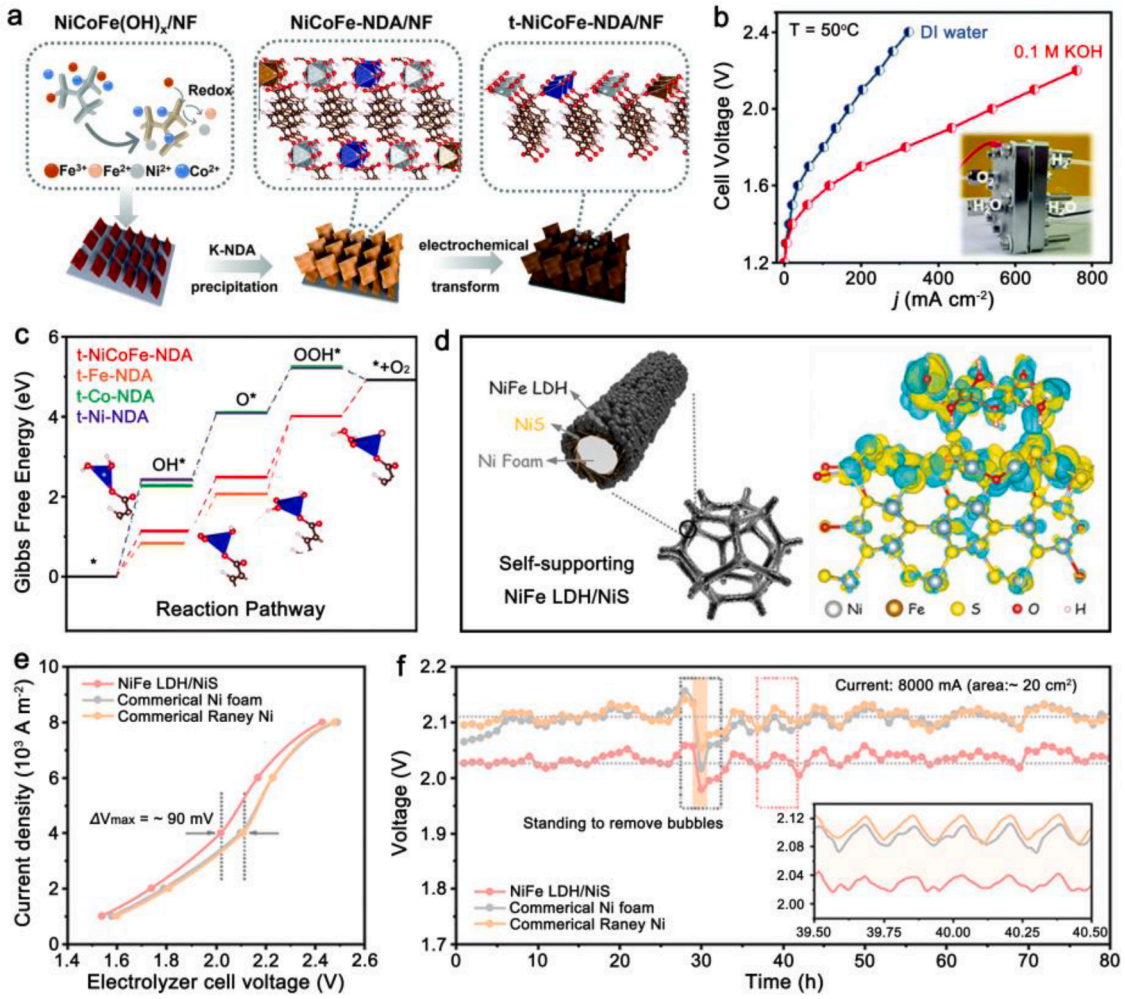

Fig. 4. (a) Schematic illustration of the ion-exchange preparation and topological transformation process of the NiCoFe-NDA/NF. (b) Polarization curves of the NiCoFe-NDA/NF in AEMWE cell. (c) Gibbs free energy diagram of the NiCoFe-NDA. Reproduced with permission.[84] Copyright 2021, Royal Society of Chemistry. (d) Schematic illustration of the heterostructure and the electron density difference of NiFe LDH/NiS electrodes. (e) Polarization curves and (f) chronopotentiometry curve of the NiFe LDH/NiS-based electrolyzer at 80~85 °C. Reproduced with permission.[85] Copyright 2021, Wiley-VCH.

2.2.2. *Self-supported HER electrocatalysts*

In recent years, the application of transition metal sulfides (TMSs) as self-supported HER electrocatalysts has attracted extensive attention owing to their cost-effectiveness and excellent electrical properties [87]. For example, Park *et al.* synthesized a self-supported Co_3S_4 NS/NF electrode by manipulating the sulfurization process, in which the crimped Co_3S_4 nanosheets are packed evenly and densely on the Ni foam substrate, enabling it to fully contact with the electrolyte and ensuring the diffusion of produced H_2 [88]. The AEMWE device with Co_3S_4 NS/NF cathode shows a cell voltage of 2.0 V to deliver the current density of 431 mA cm^{-2} with good mechanical durability. Guo *et al.* reported a rapid method for preparing bimetallic Ni-Co-S catalysts and investigated the effect of electrodeposition parameters on the intermetallic coupling [89]. The optimized Ni-Co-S/CP cathode is coupled with IrO_2/CP anode for driving the AEM water electrolyzer, which can gain a current density up to 1.7 A cm^{-2} at 2.4 V_{cell}, outperforming the commercial Pt/C electrocatalyst.

Transition metal phosphides (TMPs) are also widely applied in assembling AEMWE devices, where the locally electron-rich P sites are skilled in capturing the protons, thus remarkably promoting HER [90–93]. Moreover, TMPs generally exhibit outstanding thermal and electrochemical stability owing to the strong M-P bonds in their crystal structure. Guo *et al.* demonstrated a Cu-Co-P/CP self-supported electrode, which only required an operating voltage of 1.9 V to reach 0.7 A cm^{-2} in an AEMWE single cell and provides excellent stability for 24h with a negligible voltage rise [94]. Inspired by the above, Lee *et al.* proposed a chemical transformation route for preparing scaled-up ternary NiFeCo phosphide electrode (180 cm^2) through corrosion engineering and subsequent phosphating process, as illustrated in Fig. 5a. [95] The self-supported $NiFeCoP_x$/NF showed a high activity towards alkaline HER, requiring an ultra-small overpotential of 37 mV to output 10 mA cm^{-2}, comparable to the state-of-the-art Pt/C catalysts. The intermediate product, *i.e.*, NiFeCo LDH/NF electrode, is verified to be suitable for electrochemical oxygen evolution in alkaline media (η_{10} = 170 mV). Consequently, the AEM water electrolyzer based on the NiFeCo LDH//$NiFeCoP_x$ couple required only 1.72 V_{cell} (without *IR*-compensation) to realize the current density of 500 mA cm^{-2} with an energy efficiency of 73% (Fig. 5b). Such hydrogen production performance surpasses most of the reported AEM water electrolyzers based on transition metal catalysts (Fig. 5c).

Furthermore, Wan *et al.* developed the *in-situ* synthesis of Fe-Ni-P-S catalysts on Ni foam with controllable morphology and composition by a one-step electrodeposition method, which integrated the advantages of M-S bonds and M-P bonds, therefore realizing the dual-regulation of intrinsic activity and mass transport [96]. Impressively, the $Fe_{0.2}Ni_{0.8}$-$P_{0.5}S_{0.5}$ electrode shows superhydrophilic and aerophobic properties (Fig. 5d), which significantly accelerate the diffusion of electrolyte and bubbles at high current densities. As a result, the

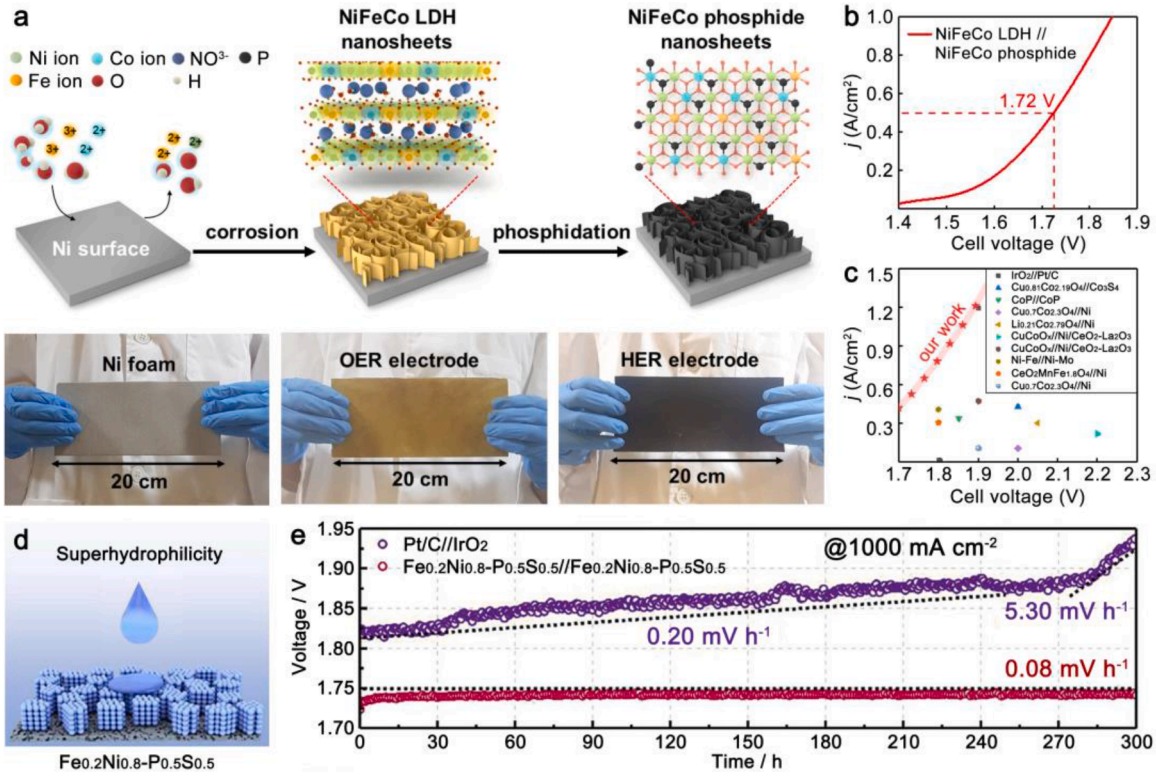

Fig. 5. (a) Schematic illustration for the preparation of NiFeCo LDH and $NiFeCoP_x$ nanosheets, below are the corresponding photographs. (b) Polarization curves and (c) performance comparison of the NiFeCo LDH//$NiFeCoP_x$ AEM water electrolyzer. Reproduced with permission.[95] Copyright 2021, Elsevier. (d) Schematic diagram of the super hydrophilic $Fe_{0.2}Ni_{0.8}$-$P_{0.5}S_{0.5}$ electrode. (e) The long-term stability at 1 A cm^{-2} of the AEM water electrolyzers based on $Fe_{0.2}Ni_{0.8}$-$P_{0.5}S_{0.5}$//$Fe_{0.2}Ni_{0.8}$-$P_{0.5}S_{0.5}$ and Pt-C//IrO_2 pairs. Reproduced with permission.[96] Copyright 2022, Elsevier.

self-supported $Fe_{0.2}Ni_{0.8}$-$P_{0.5}S_{0.5}$ electrode as a high-efficient dual--functional catalyst exhibited an excellent performance of only 2 V to achieve 2.5 A cm^{-2}. Meanwhile, it can operate stably for continuous 300 h under 1 A cm^{-2} with a voltage rise rate of 0.08 mV h^{-1} (Fig. 5e), much lower than the 5.3 mV h^{-1} of the commercial Pt-C//IrO_2 couple.

2.2.3. *Different types of novel electrocatalysts*

The above sections mainly introduce the electrocatalysts based on their chemical constituents and whether are self-supported. In brief, transition metal-based catalysts with low prices and high alkali resistance are the best candidates for AEMWE application. Self-supported catalysts with higher surface area and better mechanical stability normally show a high-performance superior to the powdery catalysts, however, the alkaline electrolyte seems to be essential for them to evoke activity and keep long-term stability. On contrary, powdery catalysts with a wider material library have a larger applied range than self-supported catalysts. The MEA technology and design strategies of powdery catalysts are also able to be transferred from the fuel cell and PEMWE fields. Depending on the operation condition (electrolyte, temperature, *etc.*), an industrial community can choose the appropriate type of electrocatalyst for application.

Furthermore, some novel types of advanced electrocatalysts are worth to be mentioned. Single-atomic and alloy-cluster electrocatalysts with ultra-high atomic utilization emerge as a vital research direction to improve HER/OER activities at high current densities. The rational construction of carbon-supported single-atom and cluster structures can maximize the active metal centers inside catalysts, offering sufficient spatial accessibility for intermediates to facilitate reaction kinetics. For example, Su *et al.* fabricated a novel single-atom catalyst (SAC) that rich Pt_1–C_2N_2 active centers that were strongly coupled in N-doping carbon substrate, showing a high mass activity of 3350 A g^{-1} at 232 mV for OER [97]. Similarly, Shui and co-workers developed a phosphate functioned IrMo clusters on macro-porous N-doped carbon (IrMoP/MNC) with high noble metal utilization for HER [98]. It renders a high mass activity of 18.58 A mg_{Ir}^{-1} at an overpotential of only 100 mV. However, this type of electrocatalyst normally has high surface energy, tending to agglomerate and inactivate during the long-term catalytic process, so there are still few related reports for the AEMWE application. Effectively constructing hybridization of a single atom/cluster with the functionalized carbon to generate strong interfacial interactions will be the key to obtaining electrocatalysts with both ultra-high activity and outstanding stability in the future.

Defect and interface engineering of catalysts has attracted great attention and developed rapidly in recent years. In general, defects in the electrocatalyst comes from the dopants, vacancies, and grain boundaries. By introducing defective structures, the intrinsic electronic structure of nearby defects can be altered, resulting in the optimization of reaction intermediates adsorption and enhancing reaction kinetics [99–101]. Chen *et al.* recently synthesized a kind of cationic defects enriched iron-based oxides catalyst by the novel electrochemical reduction etching method [102]. The introduced Fe vacancies not only enhance the Ni-O covalency but also moderate oxygen intermediate species adsorption, thus largely increasing water oxidation activity. Similarly, Park *et al.* introduced oxygen vacancies into the Cu-Co oxides catalyst [78]. The as-prepared electrode achieved a high current density of 1.39 A cm^{-2} at 1.8 V_{cell} for the AEMWE. This work shows the huge potential of defect engineering to increase the cell performance of AEMWE with high energy conversion efficiency. On the other hand, interface engineering enables to overcome of the performance limitation of electrocatalyst by the electron effect and ensemble effect, which can optimize the reaction pathways and balance the adsorption energy of reaction intermediates, respectively [103]. Some heterointerface engineered electrocatalysts such as NiFe LDH/NiS, NiFe LDH-MoS_x, and Pt-decorated $Ni(OH)_2$/CeO_2 have been reported to achieve excellent

water electrolysis performance [84,85,104]. In the future, defect and interface engineering holds promise for the development of efficient electrocatalysts and electrodes for AEMWE.

2.3. Advanced gas diffusion electrode design

The GDE is the core component of AEMWE. It includes the catalyst layer (CL) and the GDL, as exhibited in Fig. 6. The GDL further comprises a macro-porous substrate (MPS) and a microporous layer (MPL). The CL is typically formed by depositing powder catalyst particles on the MPL, therefore the structure of MPL affects catalyst loading, distribution and also interfacial contact [109]. In addition, the porosity and thickness of CL, as well as the ionomer content, impact the catalyst performance [110–112]. The transportation capabilities of porous GDL, which is used for the delivery of reactants and products, are deeply affected by its morphology, microstructure, and physical characteristics [113–115]. In an integral GDE, the water, gas, and catalyst come into intimate contact forming a triple-phase interface, in which the synergistic function of all components decides the performance of the electrochemical reaction [116]. In this section, we firstly elaborated on the combined transfer behavior in the GDE and then summarized the strategies by designing pore and interfacial structures to improve GDE performance.

2.3.1. Synergistic transfer behavior in the GDE

A completed reaction process in the GDE containing the synergistic transfer behavior of electrons, ions, water, and gas. Specifically, the electrons and ions (*i.e.,* charge) transfer process would form a closed-loop circuit. Fig. 6 takes the cathodic GDE side as an example. The HER firstly takes place on the reacting interface of CL with the formation of OH^- and consumption of e^- by the proton-coupled electron transfer process (Eq. 2). The consumed e^- (yellow curve) is achieved from the external circuit through the BPP, the GDL and the conductive CL. Meanwhile, the generated OH^- (orange curve) transforms to the anodic reacting interface *via* anion-exchange polymers (*i.e.,* ionomers and AEM). Although the OH^- transfer capability is primarily determined by the conductivity of the AEM and ionomer, with a basic electrolyte, the conductivity of the OH^- will be greatly enhanced [28,117,118].

Water and gas transfer is another important pair of transport behaviors. In Fig. 6, the water, which is transported through the pores of the GDL (blue curves), is split into H_2 gas on the CL. which is transported through the pores of the GDL (blue curves). Bubbles form when the total dissolved gases ultimately achieve a specific concentration that exceeds the supersaturation threshold [119,120]. The gas bubbles (gray bubbles embedded in the GDE) are successively diffused through the void pores within the CL and GDL and ultimately released from the cell through the flow-field channels within the BPP. As surface aerophobicity is positively correlated with hydrophilicity, the hydrophilicity/hydrophobicity trade-off is crucial for the balance of water supply and gas removal [121]. In addition, the GDL pore structure is influential in the growth and removal behavior of gas bubbles during the electrochemical reaction [122].

Based on the above, transfer behaviors in the GDE are quite linked to its intrinsic structure. An ideal GDE should have gradient pore size, high porosity, proper hydrophilicity, and electric conductivity to achieve rapid water supply, gas removal, and electron transfer. In addition, a smooth MPL surface is also required to acquire intimate contact with the catalyst and the membrane for high catalyst utilization and fast reaction kinetics. Strategies for obtaining high-performance GDEs by designing pore and interface structures and their impact on synergistic transport behaviors are summarized below.

2.3.2. Pore structure design

A delicate balance of trade-off between water supply and gas removal is essential in cell operation. To address the gas removal, many studies explored the mechanism of bubble nucleation, growth, and detachment in GDL [126–128]. These findings revealed that bubble nucleation occurs at the triple-phase boundary, where the bubbles undergo spherical growth within the surrounding pore walls and rapidly detach when it grows up to the critical size. Generally, a small pore size provides higher breakthrough pressure for bubble diffusion. However, Grigoriev *et al.* found that in the sample with the smallest pore size, the increased capillary pressure and the related increased bubble pressure on the electrode surface brought about a larger additional cell voltage [129]. As a result, a medium pore size of 10-12 μm was selected. Additionally, Yang *et al.* investigated the bubble removal behavior on three types of nickel electrodes and found that nanofiber felt (NF), despite having a higher surface area than microfiber felt (MF), was more likely to induce bubble snap-off due to its larger D_{pore}/D_{throat} value, resulting in bubble entrapment and lower fluid flow permeability (Fig. 7a) [123]. Hence, the pore size must be in excess of the pore height to avoid gas accumulation.

The pore size and porosity of GDL are two related parameters. Some studies have demonstrated that the high porosity of GDL allows for efficient gas and water transport; however, other studies suggest that the high porosity increases in-plane resistance and contact resistance [129,130]. In this way, there are the optimum values for the pore size and porosity of the GDL to maintain a balance between the contact with CL and the mass transfer properties. For example, Kang *et al.* fabricated a novel thin/well-tunable titanium-based GDL and observed the microbubble dynamics along the rim of each pore by a high-speed and

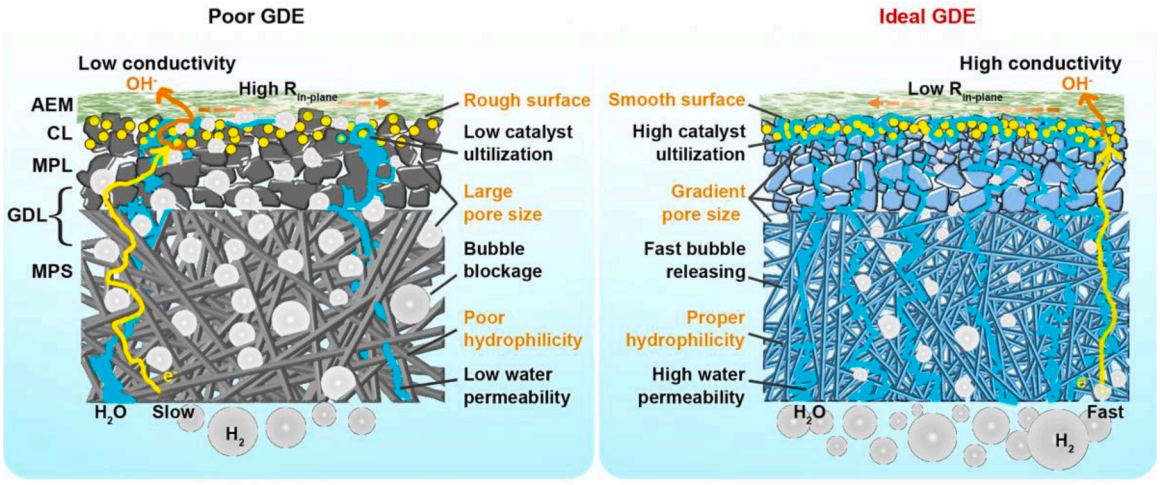

Fig. 6. Schematic illustration of transport behavior difference between poor and ideal GDE for AEMWE.

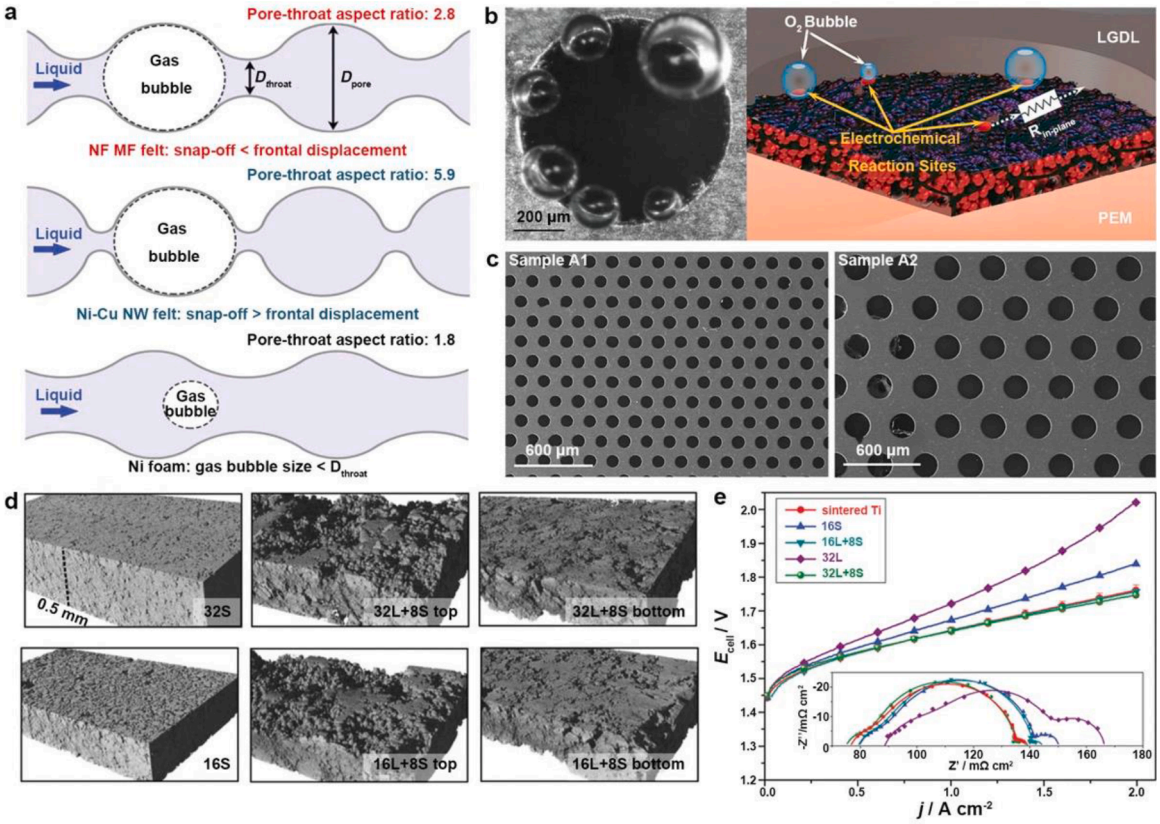

Fig. 7. (a) Diagram of gas bubbles traveling through the pores with different pore-throat aspect ratios. Reproduced with permission.[123] Copyright 2020, Wiley-VCH. (b) Visualization and schematic of the electrochemical reaction at the pore scale. (c) SEM images of typical thin/well-tunable titanium GDL. Reproduced with permission.[124] Copyright 2017, Royal Society of Chemistry. (d) 3D reconstruction of the GDL from the X-ray computer tomography (CT) analysis. (e) Polarization curves. The inset shows the Nyquist diagrams of the corresponding electrochemical impedance spectroscopy (EIS) measurements. Reproduced with permission.[125] Copyright 2017, Royal Society of Chemistry.

micro-scale visualization system (Fig. 7b) [124]. The GDL (Fig. 7c, left) with larger porosity and smaller pore size shows decreased ohmic losses, activation losses, and diffusion losses, allowing rapid bubble detachment. Similarly, in a recent study, Lee *et al.* added patterned through-pores above a commercial sintered titanium powder-based GDL, which minimized the mass transfer overpotential of the electrolyzer up to 76.7% compared to commercial GDL materials [37].

Further, a single dispersed pore structure is not preferable to the two-phase transport of water and gas [131] On the one hand, the GDL with only a single macropore is not favorable for the detachment of oxygen or hydrogen bubbles on the surface of the CL due to insufficient capillary pressure. On the other hand, the GDL containing a single type of micropores is not conducive to the water supply due to limited pathways. Thus, the mass transfer can be improved by designing graded pore structures and taking advantage of the different pore sizes on the transfer behavior of gas and water [132]. For example, Lin *et al.* made up for the problem of insufficient micropores in Acetylene Black carbon and the low number of mesopores and small pores in Vulcan XC-72 by fabricating a composite carbon black GDL [131]. The new GDL with a more rational pore structure met the excellent water and gas transmission. In another study, Lettenmeier *et al.* produced a new type of pore-graded GDL *via* vacuum plasma spraying (VPS) (Fig. 7d) [125]. The pore-graded samples of 16L + 8S and 32L + 8S exhibited comparable performance to the state-of-the-art sintered Ti-GDL (Fig. 7e), which was largely attributed to the mitigation of the mass transport limitations in the pore-graded GDL, as shown by the more minor low-frequency arc (inset of Fig. 7e). Moreover, in a recent study, Paliwal *et al.* modeled the water-oxygen distribution in GDL and found that the gas saturation at the MPL/CL interface decreases as the porosity of the GDL gradually increases from the membrane to the flow field, which reduces mass transfer loss and ohmic resistance loss [133]. That means, in addition to the design of the overall pore size distribution of the GDL, the interface design of GDL/CL, such as the design of the MPL pore structure, can greatly improve cell performance.

2.3.3. *Interfacial structure design*

The MPL, commonly a thin layer between the MPS and CL, is added to the GDL to strengthen the interfacial connection, protect the delicate AEM from perforation, and serve as a substrate for deposited catalyst particles. An optimized MPL design with suitable thickness, porosity, pore size, and morphology can yield an ideal gas/liquid/solid three-phase interface, achieving high catalyst utilization and low mass transport loss [138–140]. For example, Razmjooei *et al.* developed a novel GDL by introducing nickel-based microporous layers *via* air-plasma spraying (APS), as shown in Fig. 8a [134]. This lower tortuosity of NiMPL-GDL decreases the capillary pressure and bubble point, which minimizes mass transfer losses. Meanwhile, the lower interfacial contact resistance (ICR) induced by improving the contact area between the GDE and the AEM, helps to upgrade catalyst utilization. In another study, Schuler *et al.* fabricated a series of GDLs with three different MPLs [135]. They found that the tailored surface of GDL with small MPL particles provides a high interfacial contact area, resulting in less deformation of the membrane and higher catalyst utilization (Fig. 8b). In addition, MPL thickness is a parameter that is fundamental to overall cell performance, as thicker MPLs may lead to mass transfer limitation due to the prolongation of the diffusion pathways, while an ultra-fine MPL fails to given desired interfacial properties and accommodating the deposited catalyst particles [113]. In general, the thickness of MPL

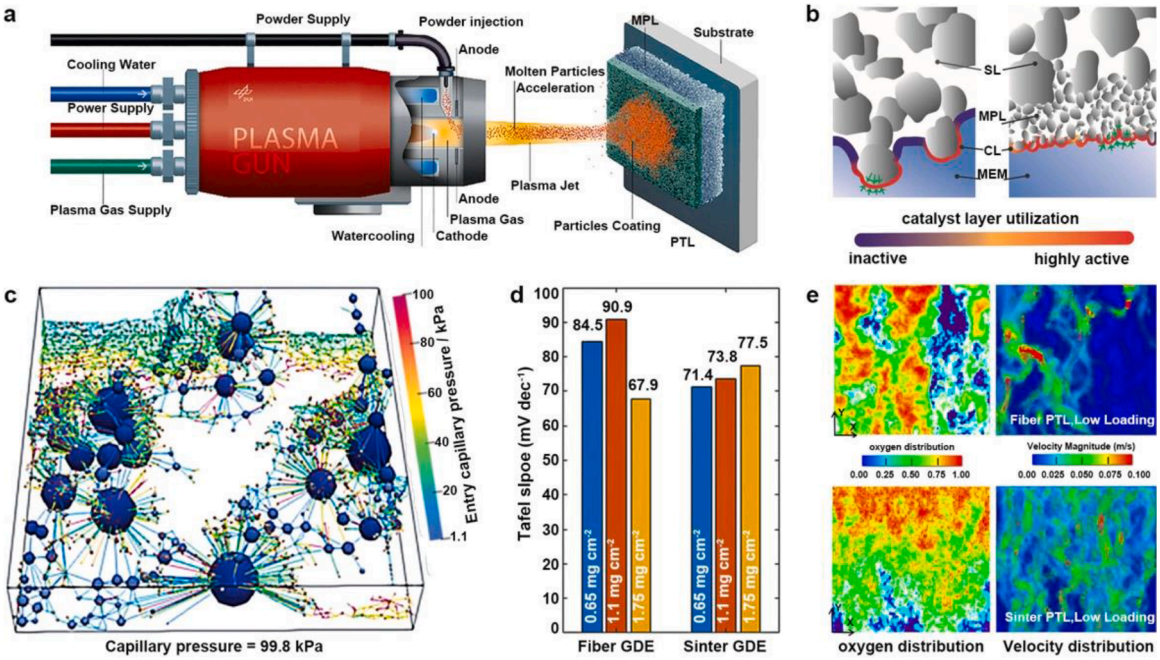

Fig. 8. (a) Schematic illustration of APS coating of NiMPL on GDL. Reproduced with permission.[134] Copyright 2021, Elsevier. (b) Visualization of the microporous layer effect. Reproduced with permission.[135] Copyright 2019, Wiley-VCH. (c) Drainage characteristics generated from the pore network simulation results in the coated GDL invading pores and throats at capillary pressures of 99.8 kPa. Reproduced with permission.[136] Copyright 2022, Royal Society of Chemistry. (d) Tafel slopes. (e) Modeling prediction of oxygen flow and corresponding velocity profiles in a high loaded sintered GDL and low loaded sintered GDL. Reproduced with permission.[137] Copyright 2022, Elsevier.

should preferably not exceed 20 μm [141].

Surface coating such as Ir, Nb, or Ti can not only significantly improve cell performance but also protect the GDL against corrosion [85,142]. For example, Stiber *et al.* developed a non-precious metal coating of Nb/Ti on stainless steel (SS) mesh [136]. The high ICR is ensured by the well-defined electrical connection between the Nb/Ti coating and the CL, while the small pores in the Nb/Ti coating offer additional pathways for reactant transport, thus boosting the reaction kinetics (Fig. 8c). Sintering is another common method to improve the surface structure of GDL as the sintered structure possesses a unique microporous layer [129,143]. For example, Leonard *et al.* compared the morphology of two commercially used sintered titanium and fiber titanium GDL and found that Ti fiber GDL despite having higher porosity and lower pore tortuosity, exhibited an uneven surface structure, resulting in inferior performance to the sintered GDL [144]. The study of Kulkarni *et al.* also observed that sintered GDL showed faster reaction kinetics (Fig. 8d) [137]. As shown in the 3D modeling prediction of oxygen flow, the sintered GDL surface presented a more uniform oxygen distribution within the GDL (Fig. 8e), which accounts for the higher performance than the fiber GDL at low catalyst loading. Superior surface properties can also be realized by using chemical etching or surface coating for proper hydrophobic and low ionic contact resistance [145–147].

In summary, driven by the success of numerous studies on the structural design of GDLs, an increasing number of GDLs with various materials, pore structures, and surface structures are being developed commercially. We consider that for future research it is essential to select the most suitable GDL from the available GDLs to ensure stable and good cell performance. In addition, benefiting from the ever-advancing characterization technologies, the water/gas transport properties of GDE and the reaction kinetics of the catalysts can be analyzed in an *operando* state to provide us with a depth understanding of the GDE structure.

3. Lab-scaled AEMWE system construction and operation conditions

3.1. Lab-scaled AEMWE testing system

To promote the development of AEMWE, a standardized lab-scaled testing system (LSTS) and electrode coating system are essential. In this section, we first demonstrate a general configuration of LSTS with the detailed establishment guideline. Then, diverse electrolyzer reactors and components differences are elaborated. To guide the electrode preparation based on the powdery catalyst, a home-made and low-price coating setup is introduced. Besides, some mature testing systems and coating systems in commercial companies are also displayed.

3.1.1. AEMWE testing system configuration

The lab-scaled AEMWE testing system is required to fulfill the functions of (i) evaluating the activity and stability of the electrolyzer, (ii) exploring the influence of different operation conditions (*e.g.*, temperature, electrolyte concentration, liquid feed type, *etc.*), and (iii) simulating industrial application scenarios. Generally, an AEMWE LSTS needs to include the following hardware: computer, AEM electrolyzer, liquid bucket, gas tank, liquid/gas separator, potentiostat, pump, heater, temperature controller, back pressure regulator, mass flow controller, and gas chromatography (GC), as depicted in Fig. 9. The whole testing system can be divided into the water/gas loop systems, heating system, and control system.

The water/gas loop systems are constructed by connecting the pipes between different components to realize the liquid circulation and gas collection. Valves are installed in the piping to quickly switch the water/gas loop on and off. All connectors are recommended to use 1/4-inch quick connectors, which facilitates the regular inspection and replacement of piping. For the liquid pathway, the electrolyte flows from the liquid bucket into the electrolyzer through the adjustable speed pump. Here we recommend the KNF diaphragm liquid pump [148]. By coupling with the adjustable voltage power adapter, it can effectively

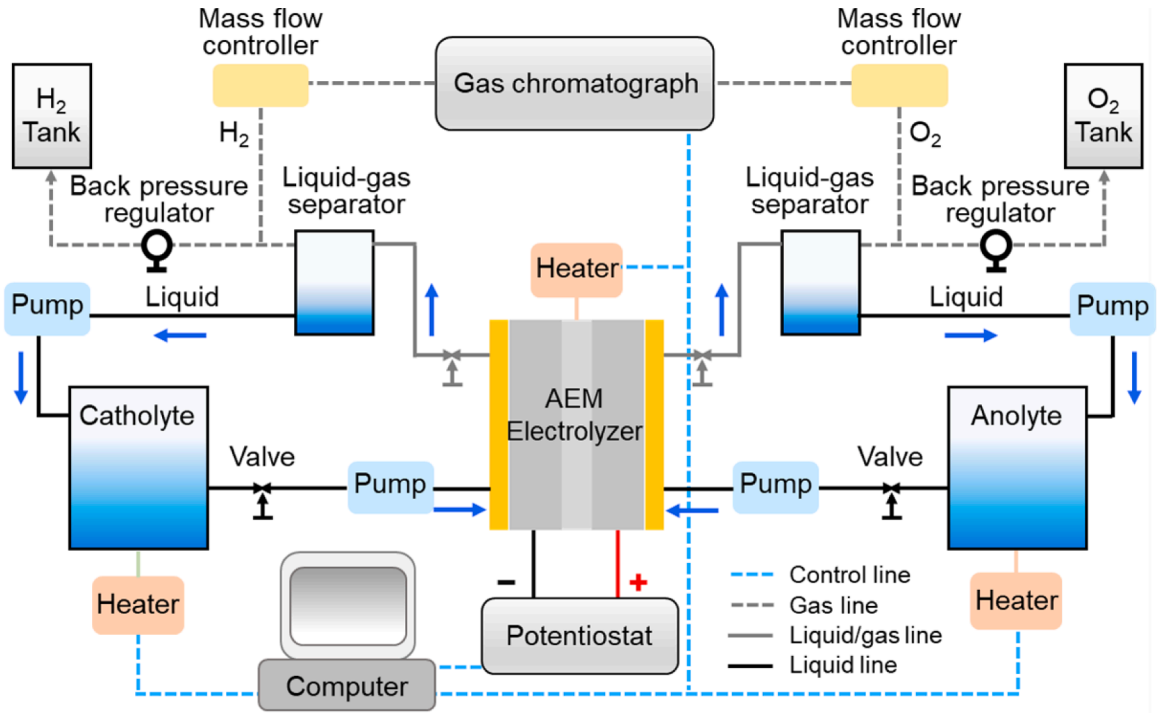

Fig. 9. Schematic of the AEMWE lab-scaled testing setup (LSTS).

control the water flow rate. The water inlet flow should be mounted at the lower position of the electrolyzer compared to the outlet flow, which gives a pressure to let water permeate into GDE and gas release in an updraft. The electrolyte/gas products mixture from the outlet of the cell requires to be separated by respective water/gas separators. The circulation of liquid along the liquid channel can reduce the electrolysis cost.

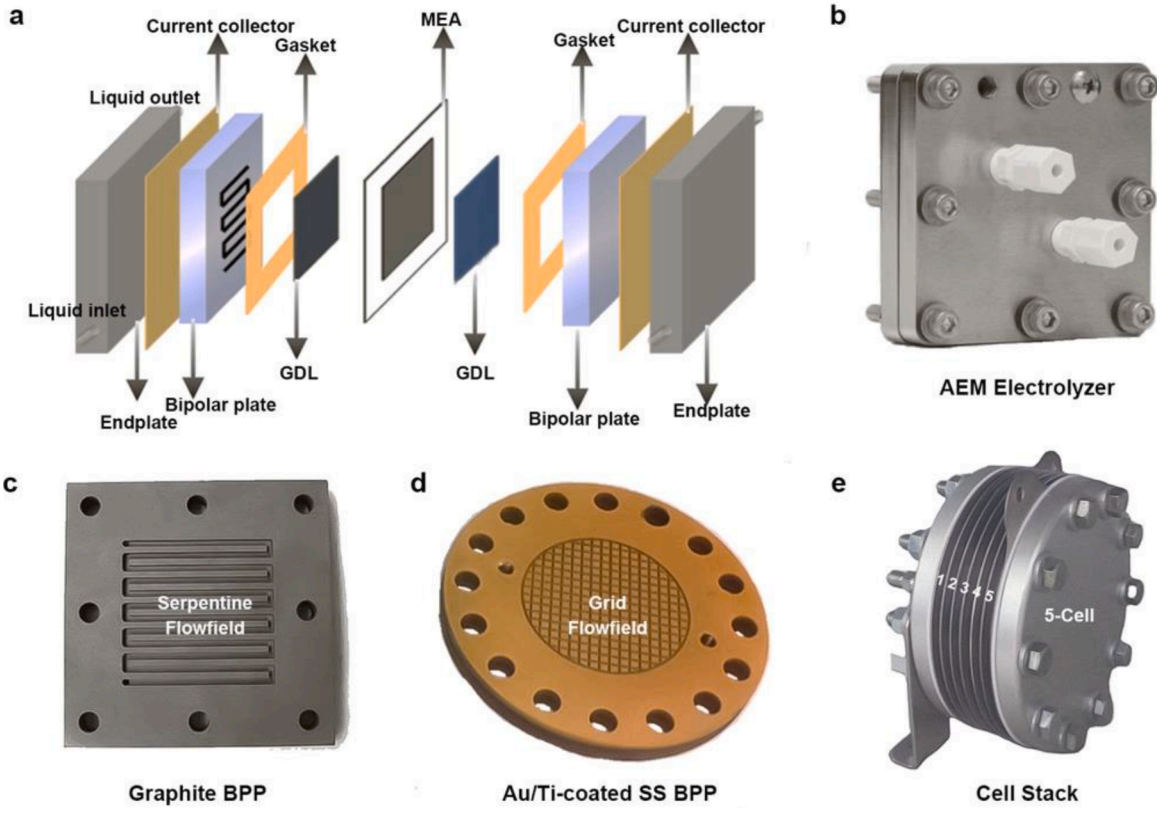

Fig. 10. Configuration and actual images of typical AEM electrolyzers and flow field. (a) Schematic diagram of an AEM electrolyzer. Reproduced with permission. [149] Copyright 2021, Nature Publishing Group. (b) Typical square AEM electrolyzer. Reproduced from [150]. (c) Square Graphite BPP with the single-serpentine flow field. (d) Circle Au/Ti-coated SS BPP with the grid flow field. Reproduced with permission.[151] Copyright 2014, IOP Publishing. (e) Cell stack of five single cells.

The separated gases would pass through a back pressure regulator and then be stored in a gas tank or enter the GC to verify the purity and calculate the Faraday efficiency.

The heating system is another important system. The cell is normally heated by a heating rod inserted into the cell or by a heating sheet attached to the cell. The electrolyte supplied to the cell is also heated to the same temperature as the cell. Depending on the size of the liquid bucket, it can be heated by a Teflon-coated immersion heater or heating jacket. These heaters equipped with PID controllers can precisely control the temperature. In addition, keeping the piping temperature constant is also crucial. For instance, in wintertime when the difference between the room temperature and test temperature is considerable, a large temperature fluctuation would occur due to the loss of heat in the piping. Therefore, it is advisable to wrap the pipes with insulation to keep the electrolyte temperature.

Ideally, the control system can be a computer with a feasible interface to integrate control of the potentiostat, GC, flow rate controller, temperature controller, pressure controller, *etc.* In this process, different sensors, relays, and electronic devices such as microcomputers (Raspberry Pi) are supposed to be enabled simultaneously. More complex control systems can be built by cooperating with professionals. Certainly, the functionality of the control system depends on the project target for different research groups.

3.1.2. AEM electrolyzer and inner components

The AEM electrolyzer as a reaction generator directly determines the cell performance. A typical AEM electrolyzer is composed of the MEA, GDLs, gaskets, BPPs with flow field, current collector plates, and endplates, as depicted in Fig. 10a [149]. In this context, we will focus on introducing the design and selection of the gasket, BPP, current collector plates, and endplates.

The commonly used AEM electrolyzers in the lab-scaled are square (Fig. 10b), polygonal, and circular. Due to the highest materials utilization of circle shape, the industrial PEMWE adopts circular cell stacks. The gaskets added between the membrane and the BPP are used to relieve uneven pressure in the cell due to the thickness of the GDL and prevent internal leakage and membrane tears. The pressure distribution over the MEA is greatly impacted by the overall gasket thickness thus it is very important to adjust gasket thickness to get a relatively uniform pressure distribution and ensure proper sealing. In practice, the number of gaskets is determined by adding or removing a gasket until the maximum performance is obtained. Normally, the thickness of the gasket is aligned flush with the surface of the GDL. Gasket materials are polyethylene terephthalate (PET) clear films with a thickness of 0.005∼0.025 inches and are laser cut or hand-cut to the required shape and size [152]. When operating under alkaline conditions, corrosion-resistant materials perfluoroalkoxy (PFA) and fluoro-ethylene polymer (FEP) are recommended.

The BPP with the flow field is the transmission channel for gas releasing and water circulation, representing more than 40% of the stack cost [153]. Under the conditions of an AEM electrolyzer, BPP must possess material qualities such as low cost, high conductivity, and chemical stability. Generally, cheap graphite (Fig. 10c) is used for cathode BPP, while an expensive Ti plate is required for anode BPP because of the exposed harsh environment of oxygen-rich, high temperature, and polarization voltage. To reduce the manufacturing cost of electrolyzer, stainless steel BPP, nickel BPP, and a small amount of precious metal coated BPP (Fig. 10d) have also been developed [151, 154,155]. The flow field structure affects the pressure of the electrolyzer, which is vital for mass transfer [156–158]. Typical shapes include squares and circles, as well as different channel configurations such as single serpentine (Fig. 10c), multi-serpentine, parallel, and grid (Fig. 10d) flow fields [151,159]. There is no consensus about the performance of these flow fields. One claim is that circular-shaped flow fields are superior to other flow fields as they can create a more uniform pressure across the active region. Nevertheless, others claim that water distribution becomes challenging when water is spread over higher surface areas in circular-shaped flow fields [160]. Majasan *et al.* found the parallel flow field performed better, as the long gas slugs formed in the serpentine flow field hinder water access [158]. In contrast, Li *et al.* found the single-serpentine flow field showed superior performance, as the highest ohmic resistance of the parallel flow field [161]. Considering the machining process, cost, and performance, we recommend a single serpentine flow field.

The current collector plates, commonly made of copper, are inserted between the BPPs and end plates of the anode and cathode. It should be noted that copper plates are prone to corrosion in alkaline conditions. Therefore, it is imperative to ensure the unit is sealed to prevent the alkaline solution from penetrating from the edge of the electrolyzer to the current collector plates.

The major role of the endplate is to provide uniform pressure distribution between various components of the electrolyzer (GDL, BPP, *etc.*) and thus reduce the contact resistance between them [162]. Ideal endplate materials entail properties of low density, high rigidity, and enough electrochemical stability. Metal materials such as titanium, aluminum, and stainless steel are often used as endplates, especially for the cheapest aluminum. Usually, eight evenly spaced bolts connect and compress the endplates and the other components, and these bolts are tightened to a fixed torque by a torque wrench to ensure no liquid/gas leakage and short/open circuit.

The stack of the electrolyzer (Fig. 10e) is constructed by a single electrolyzer combination, which can amplify the current and explore the feasibility of industrialization. The stack setup has the advantage of only configuring the collector plate and endplate on two sides, which can save material and reduce the system cost. However, the structure of BPP in the stack has a more complicated flow field design and is normally related to practical applications. Therefore, electrolyzer stacks are more used in industrial research and need to be coupled with multi-physics field calculations. Here we recommend several companies that can customize single and stack electrolyzer hardware and components, Dioxide Materials™, Mainz Hydrogen Energy, and Suzhou Sinero Technology Co.

3.1.3. Spray-coating electrode setup

Currently, the powder catalysts are still the mainstream for MEA, thus the preparation of electrodes is a non-negligible procedure for the AEMWE. Dispersion of catalyst particles, ionomer, and solvent, known as ‘catalyst ink’, is deposited onto the porous gas diffusion layer to form a GDE or on an anion exchange membrane to form an MEA. The electrode properties are strongly linked to the fabrication method.

Hand spraying the ink on the substrate with a spray gun is a straightforward method for electrode fabrication, as shown in Fig. 11a. A thin CL would be formed on the substrate when the sprayed ink solvent evaporates on the hot plate before the next turn. However, due to the uncontrollability of the manual operation, the obtained catalyst particles are not uniformly distributed, and such an electrode is a poor detector for assessing the actual catalyst performance. Fig. 11b shows an SEM image of the ideal electrode, where the catalyst is uniformly distributed on the surface of carbon fibers [163].

Sonicated spraying is a novel technique for electrode preparation, which can precisely control the loading and distribution of the catalyst. The catalyst ink is atomized into a fine mist at the nozzle tip. The atomization capability determines the distribution of the catalyst. Compared to the hand-spray method, the ultrasonic spraying method provides a more uniform distribution of the catalyst ink, allowing for better utilization of the catalyst, which is more apparent at lower catalyst loadings. Fig. 11c is a commercial spraying machine from Sono-Tek Corporation, model ExactaCoat Inert, which is at a high price.

Apart from that, our group has built a simple and low-cost coating setup, as presented in Fig. 11d. This program-controlled spray device can produce a more uniform CL than hand spray. Certainly, the catalyst sprayed by this coating device cannot match the performance of

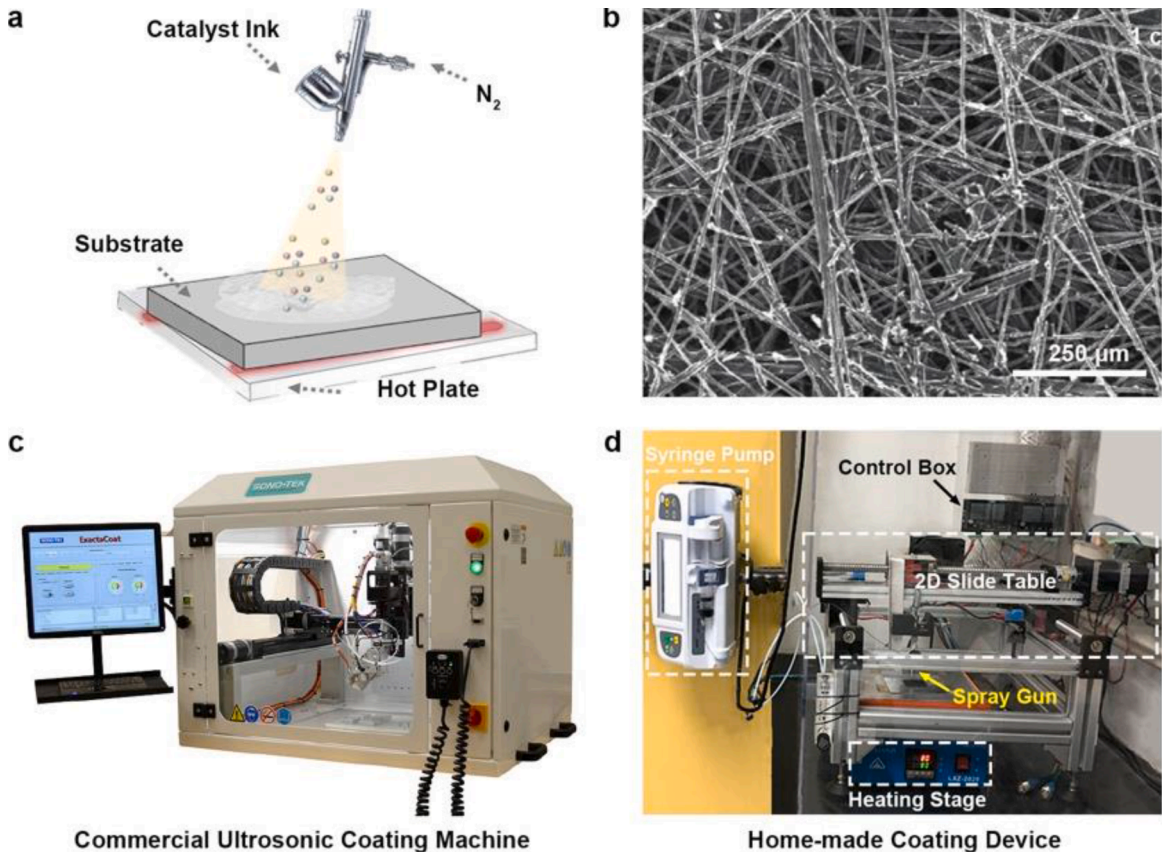

Fig. 11. (a) Schematic diagram of manual spraying. (b) SEM image of the carbon paper coated with catalysts. Reproduced with permission.[163] Copyright 2010, Global Digital Central. (c) Commercial Ultrasonic coating machine.[164] Copyright 2022, Sono-Tek Corporation. (d) Home-made coating device.

commercial spraying machines, but it is sufficient for the earlier stage of AEMWE research at a lab-scaled. The device is mainly composed of three parts: the heating stage plays a heating role to accelerate the volatilization of solvent in ink, the syringe pump is used to control the ink flow rate, and the 2D slide prompted by the control box makes the spray gun moving at a uniform speed on the XY axis. The obtained electrodes can be observed directly with a high-resolution digital camera.

The composition of the ink is another essential factor worth considering in electrode preparation [165–167]. The ionomer (*e.g.*, FAA3-50, Fumion, Sustainion® XA-9) is commonly used to enhance OH^- conduction from the electrocatalytic metallic surface towards the AEM. The variation of ionomer content in ink has been one of the most analyzed parameters. There is a consensus that the ionomer content is 10~15 wt% of the coating catalyst [168,169]. Different solvent systems impact the dispersion of ionomer and catalyst particles. Moreover, the residual solvent that had not evaporated during the spraying process

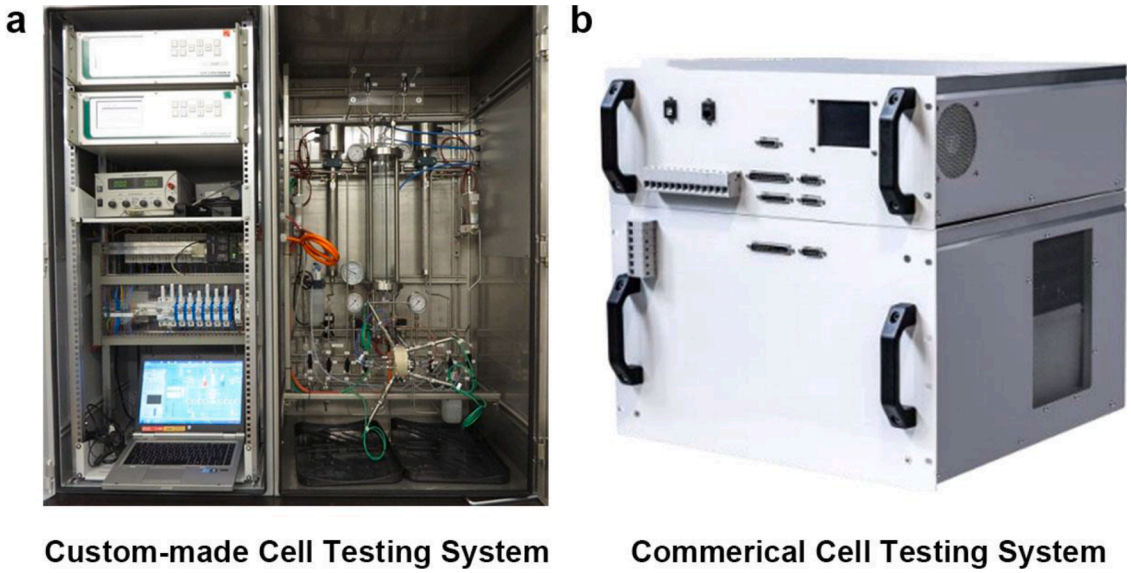

Fig. 12. (a) Custom-made cell testing system.[171] Copyright 2017, ICE2017. (b) Commercial cell testing system.[172] Copyright 2022, Enapter.

would affect the surface area, hydrophobicity, and capillarity of the electrode [170]. Methanol, isopropanol (IPA) and ethanol are the commonly used solvents. We recommend using IPA/H_2O (3:1, w/w) [83]. In addition, it is recommended that ink be freshly prepared, sonicated as much as possible to achieve uniform dispersion of the catalyst particles and ionomer, and then sprayed on the substrate timely.

3.1.4. Custom-made and commercial testing system

In the above section, the construction of a lab-scaled AEMWE testing system has been introduced. When all the hardware and auxiliary components are effectively integrated, a test system like the one in Fig. 12a is established. This is the system from Vogt's group, with which they can implement functionalization tests under high pressure (30 bar), high temperature (80°C), and scale-up work area (19.6 cm^2) [171].

Benefitting from the maturity of PEMWE, the commercial AEM cell test systems with an intelligent control platform (Fig. 12b) have also been developed, which provides the conditions for the AEMWE system from a lab-scaled to a commercial scale [172]. For example, ACTA S.p.A. (now Enapter) developed an AEMWE device that can generate 100-1000 L of high purity H_2 per hour at 3 MPa without mechanical drying or compressing apparatus [173]. The company also offers clean energy products and environmental catalysts such as ACTA 4030 and ACTA 3030, which were developed earlier and are used in HER and OER [174]. Proton OnSite known as one of the largest PEMWE companies in the world has started to focus on AEMWE research, working on building a more economical water electrolysis system. Proton Onsite demonstrated an electrolyzer stack with a $LiCoO_2$ anode and Pt/C cathode that can produce 400 mA cm^{-2} at a cell voltage of 2.0 V and operate stably for 1000 h [175]. Nevertheless, researchers new to this field, it is more advisable to start with a self-built test system and gradually advance to a more commercial scale.

3.2. Electrolyzer assembly and operation conditions

3.2.1. State-of-the-art MEA technology

MEA is the core component in the AEMWE electrolyzer, normally sandwiched by two BPPs. Due to the symmetric structure of MEA, it normally can be simplified as the layered structure of GDL/CL/AEM at either anode or cathode sides. Among them, GDL is responsible for water, gas products and electron transport; CL is dedicated to the related HER or OER; AEM mainly focuses on hydroxide transfer and cathode/anode separation. All these reactants and components work together as a fully coupled reaction-diffusion process. Fig. 13 illustrates the structure-activity relationship in the MEA, in which the intrinsic characteristics of each component would affect their interfacial interactions and finally decide the reaction performance. For example, a three-phase interface (TPI) would be formed between the ionomer-covered catalyst, gas product bubble and electrolyte [176]. If the ionomer has a bad gas permeability, the gas product bubble would be stuck on the catalyst surface, which then triggers off a chain of negative effects (such as blocking active sites and impeding electrolyte transport), and finally, reduce the reaction performance. Therefore, many studies have proposed to improve the interface interactions in the MEA by regulating the fabrication methods and designing the advanced CL structure [85,177,178].

Currently, three MEA fabrication processes have been mainly utilized and developed in the field of AEMWE, *i.e.*, the catalyst-coated substrate (CCS), catalyst-coated membrane (CCM) and the direct membrane deposition (DMD) [179–181]. As the most common one, the CCS process requires firstly coating the catalyst on the conductive substrate (*e.g.*, GDE) and then hot-press it with a dry membrane. This process is also called the decal transfer technique. It can realize the large-scale MEA fabrication in the industry, but it usually possesses a low catalyst utilization due to the huge waste of catalysts when they are immersed inside the GDE [137]. On the other hand, the CCM process, which deploys by wet-spraying catalysts on the membrane, shows a higher catalyst utilization due to the direct attachment [182]. Accordingly, the MEA fabricated by this method requires less catalyst loading and meanwhile exhibits a higher electrochemical performance. However, its operating condition is rigorous and thus it is mostly applied in the laboratory. Similarly, the DMD process also allows good contact between catalyst and membrane but can only be prepared on a small scale [183]. It is developed based on the CCS process by further depositing an ultrathin layer of membrane on the CL. Such *in-situ* formed membrane layer realizes the incorporation of nano-structured catalyst for the maximum usage of catalyst. In general, suitable MEA fabrication methods can efficiently improve the interfacial interactions for reaching excellent AEMWE performance.

To utilize the advantage of different MEA fabrication methods, the reasonable design of the CL structure has also been reported in recent years [187]. Fig. 14a exhibits the development tendency of CL from the conventional structure to the gradient and ordered structure [184]. At the initial stage, the conventional CL is prepared by simply depositing the powdery catalyst with an ionomer on either GDE or membrane. The single distribution of ionomer and pore structure in the CL structure is hard to satisfy the different interfacial requirements in the MEA, leading to a low catalyst utilization and a high mass transfer resistance. In principle, the CL interface to the membrane should contain an abundant micropore structure with a rich ionomer and good interfacial contact, meanwhile, the CL interface to the GDE needs to have a rich macropore

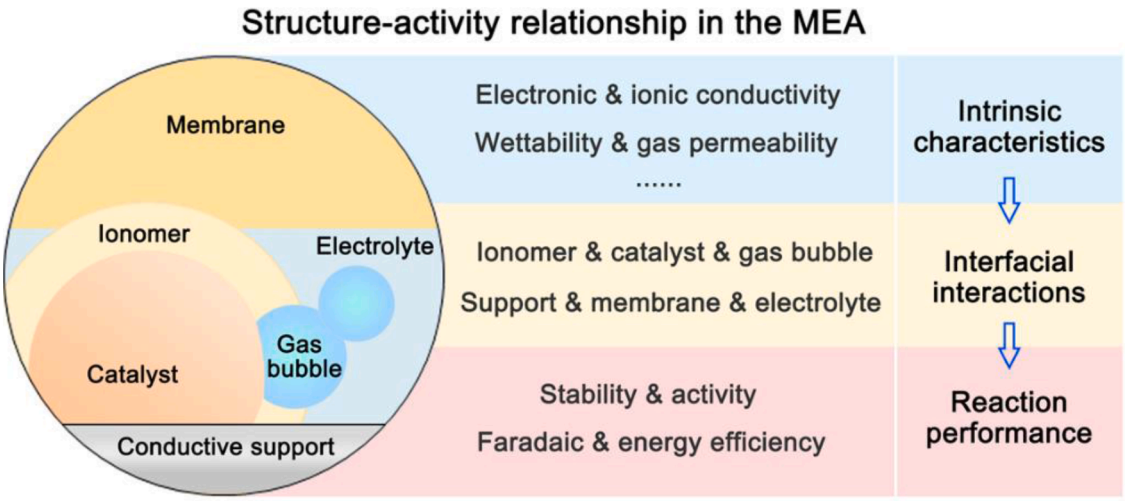

Fig. 13. Schematic illustration of structure-activity relationship in the MEA.

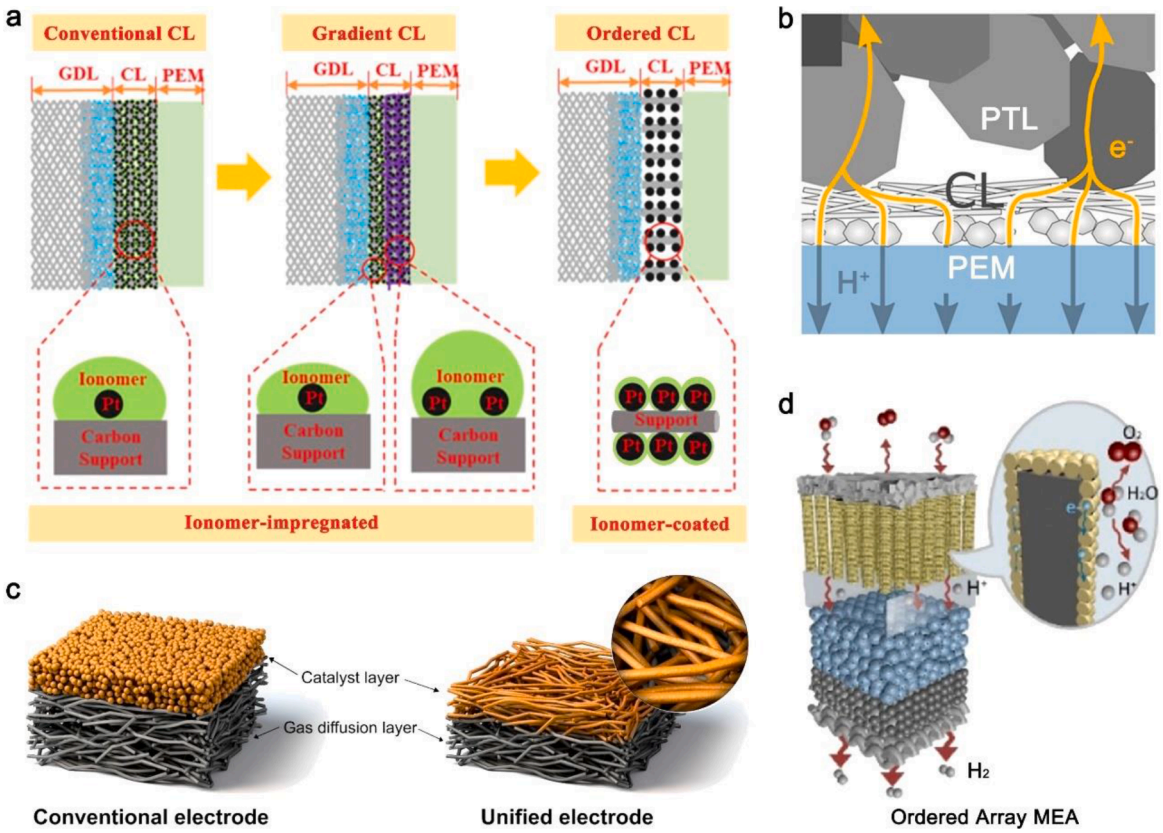

Fig. 14. (a) Schematic diagram of the development tendency of CL from conventional structure to ordered structure. Reproduced with permission.[184] Copyright 2020, Elsevier. (b) Diagram of a gradient IrO_2 layer design by the combination of nanofibers with the nanoparticle. Reproduced with permission.[185] Copyright 2020, American Chemical Society. (c) Diagram of a three-dimensional unified electrode with a gradient porous structure. Reproduced with permission.[81] Copyright 2022, American Chemical Society. (d) Diagram of an ordered and hierarchical array electrode supported MEA. Reproduced with permission.[186] Copyright 2021, American Chemical Society.

structure with good mass transfer capability. Afterward, the gradient CL structure is developed to construct the diverse microstructures to meet the discrepant requirements in interfacial environments [184]. Steven and coworkers developed a CL structure with a graded distribution of ionomer contents [188]. They found that a high ionomer content at CL/membrane interface and a low ionomer content at GDL/CL interface were respectively beneficial for optimizing the ionic flux and gaseous flux in their responding region. As a result, the CL with judicious control of ionomer composition exhibits a much higher current density by comparing with the CL with uniform ionomer content. Besides, the gradient catalyst loading and gradient structure were also wildly studied [189,190]. Fig. 14b shows a gradient IrO_2 layer design by the combination of nanofibers with nanoparticles as anode CL [185]. Such structure effectively utilizes the good electric contact and high porosity of nanofibers and high surface area of nanoparticles; thus it shows a largely improved water electrolysis performance. This gradient structure also helps to decrease the catalyst loading so which reduces the MEA cost. Furthermore, a three-dimensional unified electrode with a gradient porous structure was constructed by Park *et al.*, as shown in Fig. 14c, where the NiFeOOH catalyst was uniformly electrodeposited on the Ti paper [81]. Compared to the conventional electrode from CCS, this unified electrode has a hierarchical porous structure that the macropore owing to the GDL and mesopore/micropore formed during electrodeposition. As a result, it displayed an outstanding AEMWE activity (3.6 A cm^{-2} at 1.9 V) and good stability in 1 M KOH, superior to most AEMWE studies.

In principle, an ideal CL should have a hierarchical and ordered structure that a high surface area exposed nanoparticles catalysts densely loaded on the three-dimensional conductive framework and then coated with an ultrathin ionomer layer to conduct hydroxide, diffuse water, and release gas products. With the great progress of materials science in this decade, various fashion nanostructures have been constructed by advanced synthesis methods, which make the fabrication of the ordered CL structure achievable [187,191]. One group of successfully ordered electrodes was developed by the 3M company, named the nanostructured thin film (NSTF). [192] This kind of electrode has a similar composite structure in which the metal alloys are sputtered on the oriented crystalline organic pigment whiskers (PR-149). By changing the electrocatalyst materials, various electrochemical applications can be operated. Apart from this, many other ordered nanoarrays CL structures have been explored [184]. Based on the materials, they can be separated into carbon-based, conductive polymer-based, metal alloy-based and oxides-based array structures [193,194]. For example, Jiang *et al.* reported the fabrication of an ordered and hierarchical array electrode that defective Ir nanoparticles film (~ 70 nm) was decorated on the WO_x nanorods by the electrodeposition (Fig. 14d) [186]. On the one hand, the uniform Ir film not only serves as the electrode transfer pathway but also largely increases the catalyst utilization. On the other hand, the WO_x nanoarrays help to fix the Ir coating and give a fast mass transport channel. Consequently, this novel electrode allowed a large current density of 2.2 A cm^{-2} at 2.0 V with a loading of only 0.14 mg_{Ir} cm^{-2}. Although the above results have shown a great improvement in MEA performance by regulating the fabrication methods and designing advanced CL structures, we still encourage the researcher to explore more parameter optimization strategies in this emerging AEMWE field.

3.2.2. *Operation factors*

Electrolyzer operation conditions also play a significant influence on

the AEMWE performance. Many studies have reported the regulation of cells to assemble torque, temperature, and pressure to optimize the interfacial interaction and reaction kinetics in the MEA for improving activity [134,195-199]. Below, we will give a detailed discussion of how each variable affects the cell performance.

Normally, the electrolysis cell is assembled by sandwiching the MEA, which is surrounded by sealing gaskets, between two BPPs. The materials of gasket need to have a strong acid/alkali resistance and a high fusion point (> 200 °C), such as Teflon, PFA, *etc.* The thickness of gaskets should also be thinner (Δd > 50 μm) than the MEA so that a uniform pressure can be applied to MEA and controlled by the torque wrench [200]. In general, the applied torque should at least high enough to prevent electrolyte leakage. A higher assemble torque was reported that can reduce the electric contact resistance between MEA and current collector [201]. However, too high torque may also cause mechanical damage to MEA and short circuit of the cell due to the in-built pressure during operation. Thus, forcing a suitable cell to assemble torque is essential before testing. The most common torque value reported in the literature is 2∼6 N·m, which is related to the electrode area of MEA and the uniformity of forces.

The AEMWE performance is generally improved at an elevated temperature due to the accelerated electrode reaction kinetics and the promoted electron, ion, and mass transportation. The thermodynamic potential of the water-splitting reaction also reduces ∼8.5 mV per 10 °C. [201] These reasons make the elevated temperature (below the boiling point of electrolyte) AEMWE very charming. Park *et al.* optimized the operating temperatures of AEM cells from 50 to 70 °C in the 1 M KOH [202]. They found that higher temperature gives better performance. At 70 °C, an ultrahigh current density of 1.5 A cm^{-2} can be achieved at only 1.9 V. By applying the EIS, they further verified the decrease of ohmic resistance in the cell with the increase of temperature. However, most current AEMs cannot operate at a temperature above 70 °C for a long time, mainly because of their poor thermal stability, which limited their further development. Recently, Yan and coworkers developed a poly (aryl piperidinium)-based AEM with a low swelling ratio that can realize the continuous and stable operation at 80 °C for > 160 h [202]. With the cooperation of a self-supported F-NiFeOOH anode, they achieved a brilliant performance of ∼1 A cm^{-2} at 1.8 V for pure water electrolysis.

Furthermore, AEM electrolysis to direct produce high purity and pressurized hydrogen is promising since it can reduce the cost of the follow-up procedures. Currently, the successful operation of AEMWE at pressure < 10 bars has been verified by Ito *et al.*[203] Their experiment found that increasing H_2 pressure to 8.5 bars at only the cathode side during operation would not affect the electrolysis performance but help to reduce the humidity of the produced H_2. Besides, they also did theoretical analyses based on the mechanical robustness of each component in the cell to confirm the feasibility of operating the pressurized PEM/AEM water electrolysis technology at around 10 bars [204]. However, limitations and risks appear when the pressure further raises up to 10 bars [43]. First, the H_2 cross-permeation through the membrane becomes a serious problem. With the increase of partial pressure difference of H_2 between anode and cathode, the amount of H_2 crossover will also raise, which causes the unavoidable hydrogen oxidation reaction (HOR) at the anode. Second, each component of the hardware, including the cell, tubing, gas collection and all their connections, needs to meet higher requirements for the harsh operating condition. For example, the membrane and electrode must have a stronger mechanical strength to prevent to be damage. Those elevated-temperature and high-pressure studies help to narrow the gap between lab and industrial-scale production of cost-efficient hydrogen, therefore more efforts and breakthroughs remain in demand.

3.2.3. Electrolyte and feed mode

The electrolyte is the core component active in various interfacial interactions in the MEA. Its ingredient and feed mode change would significantly influence the AEMWE performance. To make AEMWE a cost-competitive technology, diverse solutions such as pure water, KOH, K_2CO_3, *etc.* have been wildly studied [28,205,206]. Their discrepancy advantages and feedbacks cause controversy in the academic and industrial community, *i.e.*, which one is suitable to be used in future development. Some discussions based on this are given below.

Pure water electrolysis is the most desired solution in AEMWE because it can dramatically reduce the capital cost for the operation hardware; however, using it as feed would bring some challenges, like the low ionic conductivity, and the high ohmic resistance and instability of AEM ionomer [206]. These shortcomings lead to a relatively high applied voltage and bad durability of the cell. In this case, the change of input solution to the alkaline electrolyte (KOH or K_2CO_3) would extremely accelerate the ion transfer inside the MEA for reducing ohmic resistance and enhancing reaction kinetics. Normally, the AEMWE shows a better activity in the electrolyte with higher pH, whereas the capital cost may increase accordingly due to the enhanced causticity [207]. To realize a balance between activity and cost, the mild alkaline solution shows a superior choice. Nakano and coworkers compare the electrolysis performance of KOH or K_2CO_3 under mild alkaline conditions (pH around 12) [208]. They found the 10 wt% K_2CO_3 solution has better activity than the 10 mM KOH solution due to its lower cell resistance. Similarly, Kiessling also reported that carbonates solution outperformed hydroxides solution at the same pH and a high current density due to a self-purging effect [118]. Nevertheless, the long-term stability of AEMWE in this emerging mild alkaline condition is still unknown.

Furthermore, electrolyte feed mode is another famous research field in the AEMWE. Due to the intrinsic reaction kinetics difference for the HER at the cathode and OER at the anode, the change of electrolyte at each side separately becomes very creative. Based on our summary, the electrolyte feed mode can be classified as conventional symmetric mode and novel asymmetric mode [211–214]. For the latter, it can be further divided into double-side feed or single-side feed. Fig. 15a demonstrates a typical asymmetric electrolyte feed mode, which was operated by Dresp *et al.* to explore the direct seawater electrolysis strategy [209]. In their experiment, two kinds of salt solutions (NaCl and KOH) were used to mimic seawater. A total of six feed modes were attempted, and their water electrolysis performance was compared in Fig. 15b. It shows the symmetric feed (1a) of 0.5 M KOH can achieve a good activity but degrade with operating time, whereas the asymmetric feed (1f) of 0.5 M NaCl at the cathode and 0.5 M KOH at the anode realizes a balance between activity and stability. Moreover, the excellent selectivity of the NiFe-LDH anode maintains the ∼100% faradaic efficiency of OER in this asymmetric feed even when the Cl^- crossover. Since the dissolved Cl^- triggers a competitive chloride oxidation reaction (ClOR), which would release undesired chlorine-containing byproducts (e.g., Cl_2, HClO), Yu *et al.* screened out an anionic electrolyte additive that can facilitate a stable OER under seawater electrolyte. It revealed that phosphate ions promoted excellent performance stability, which resulted from repelling Cl^- and preventing transition metal dissolution alleviating catalyst degradation, and serving as a local pH buffer to compensate for the rapid OH^- depletion under high current electrolysis [215]. These results open a new research possibility in the alkalinized seawater electrolysis. For the single-side feed mode, its working principle is based on the Grotthuss mechanism that ion diffusion occurs along with the water in the membrane [216,217]. Thus, the ion can freely move during single-side feed only if the abundant water content is in the membrane. Some advantages of single anode feed mode have been reported recently [174]. Cho *et al.* operated the single anode KOH feed to achieve an enhanced activity of ∼1.1 A $cm^{-2@1.8\ V}$ and long-term stability for AEMWE. During the reaction, H_2O from the anolyte first transfer to the cathode for the HER and then the generated OH- return to the anode for the OER. In this case, the cathode interface will have a neutral pH that is beneficial for catalyst stability. Moreover, high purity H_2 with low humidity can be produced. However, single feed mode may also be limited by the water transfer speed in the AEM, especially at high current density. Except for the

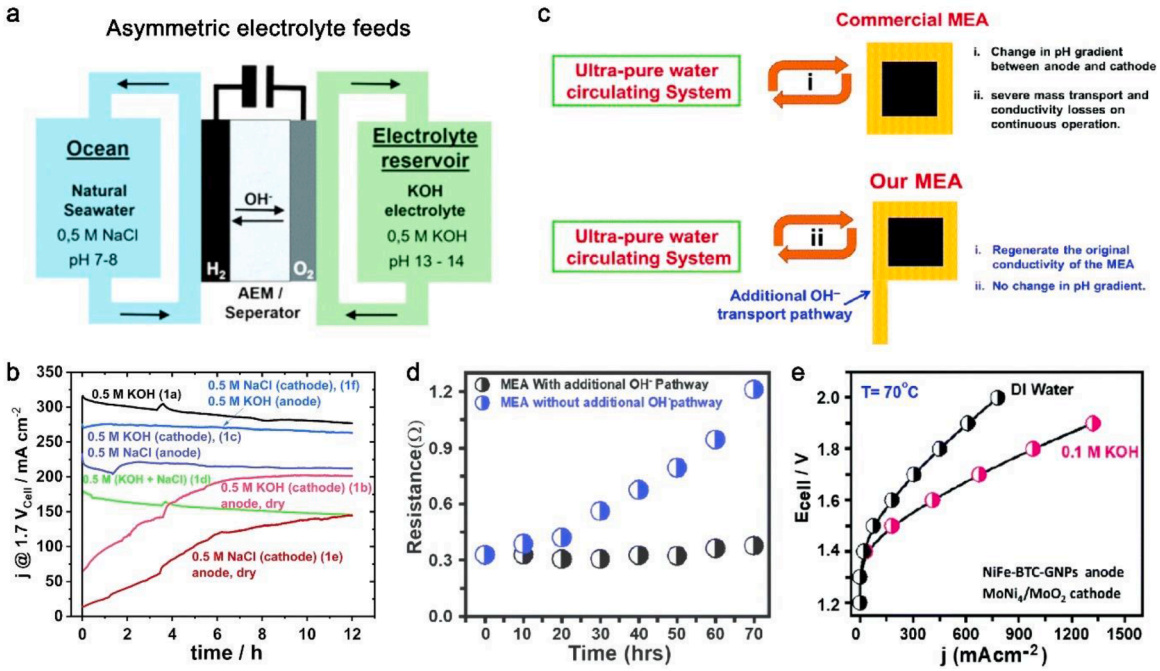

Fig. 15. (a) Diagram of asymmetric electrolyte feed mode to mimic seawater electrolysis. (b) Water electrolysis performance comparison at different electrolyte feed modes. Reproduced with permission.[209] Copyright 2020, Royal Society of Chemistry. (c) Schematic diagram of commercial MEA and modified MEA configurations, (d) cell resistance change during long-term stability, (e) polarization curves comparison of modified MEA measured in DI water or 0.1 M KOH. Reproduced with permission.[210] Copyright 2020, Royal Society of Chemistry.

above feed mode, one novel KOH-assisted-membrane feed mode was reported by Thangavel *et al.*[210,211]. As shown in Fig. 15c, they developed an amazing strategy to provide extra OH^- supply inside MEA by extending AEM into 0.1 M KOH. By comparing with conventional MEA, the additional OH^- feed can relieve the conductivity loss and pH gradient change during continuous operation in pure water, as verified in Fig 15d. Moreover, the performance improvement of AEMWE when switching pure water to 0.1 M KOH was exhibited in Fig 15e, where a high current density of 1.15 A cm^{-2} was reached at 1.85 V. In sum, much interesting science and fundamental research still wait to be exploited by modulating electrolyte and their feed mode

3.2.4. *Commercial GDEs and membranes*

AEMWE is an emerging research field requiring good cooperation between interdisciplinary scientists. It would make a high threshold if research groups had to complete the flow scheme of AEMWE including catalyst, membrane and GDE preparation, cell assembly and performance evaluation. Fortunately, matured GDE products can be acquired from the PEM water electrolysis field, and many commercial AEMs have been developed by the pioneers [141,201,218]. In this section, we will introduce the mainstream and commercial GDEs and membranes in the AEMWE field.

Commercial GDEs are normally used to load, deposit, or grow catalysts. In general, they can be classified as carbon-based GDEs and metal-based GDEs. Among them, carbon-based GDEs, including carbon fiber, carbon paper and carbon cloth, are wildly used as cathode substrates in the AEMWE. Substrate preparation companies such as CeTech, AvCarb, Sigracet, Freudenberg, Toray, *etc.* have developed many mature carbon-based substrates for water electrolysis or fuel cell [218,219]. Normally, the company would develop a series of products based on the type of substrate or preparation method with varying technical properties. Table 4 listed some representative products with their technical properties. The crystallinity, thickness and structure of the carbon layer decide the electronic conductivity and resistivity of GDEs. polytetrafluoroethylene (PTFE) content and microporous layer structure respectively influence the hydrophilic feature and interfacial contact. These different features of GDEs work together to establish an effective connection between the flow field and MEA. On the other hand, metal-based GDEs are commonly reported to be used as anode substrates [123,141,152]. For example, Ni-based foams or Ti-based mesh, which are stable in the alkaline condition under strong oxidation, were the most reported substrates to be used in the AEMWE. Besides, many companies with the mature preparation technique to fabricate the metal fiber or metal mesh, such as DeNora, Bekaert, *etc.*, meet new opportunities to apply their products in the AEMWE [201,220,221]. In short, researchers need to select suitable substrates for their fundamental studies and provide more feedbacks to substrate preparation companies for future development.

The anion-exchange membrane is the key component of the MEA. It not only acts as the only OH^- transfer pathway between anode and cathode but also separates the gas crossover during the electrolysis process. Typically, an ideal AEM should possess a low-area-specific

Table 4
Commercial carbon-based GDEs and their technical properties.

Company	Product series	Thickness (μm)	Resistivity (mΩ cm^2)	PTFE	Microporous Layer	Reference
CeTech	Carbon cloth (W1S1010)	365	< 14	Yes	Single sided	Technical data sheet
	Carbon Fiber (GDS210)	210	< 6	No	No	
AvCarb	Carbon Fiber (GDS2230)	275	< 14	Yes	Single sided	
Sigracet	Carbon Fiber 39BB	315	< 13	Yes	Single sided	
Freudenberg	Carbon Fiber (H24C5)	270	8	Yes	Single sided	
Toray	Carbon Fiber (TGP-H-060)	190	5.8	Yes	No	

resistance, a high ionic conductivity, robust thermal and mechanical stability, and superior chemical stability. Depending on the polymer backbone structure and functional groups, different AEMs show variable properties. Polyaryl ethers, such as polysulfone (PSF), polyphenylene ether (PPO) and polyaryl ether ketone (PAEK), are commonly used as polymeric frameworks in anion exchange membranes due to their low cost. However, the main chain structure of polyaryl ether AEM contains heteroatoms (O, S, *etc.*), which are prone to fracture under the attack of OH^-, resulting in a decrease in AEM toughness [222]. Besides, Bea *et al.* reported that the electron-withdrawing groups near the aryl ether bond accelerate the chemical degradation of the ether bond [223]. In contrast, polymer backbones composed entirely of hydrocarbon bonds, such as polyolefin backbones or polyaryl backbones, can improve the long-term alkaline resistance of the membrane. To further improve the stability of polyolefin AEMs, an AEM prepared by Vengatesan *et al.* employing styrene and vinylbenzyl chloride copolymerization in a quaternary amination method exhibited excellent stability for 200 h in AEMWE [224]. Compared to polyolefin backbone structures, ether-free polyarylene-based main chain polymers have high glass transition temperatures, high structural rigidity, and superior dimensional stability. Therefore, an increasing number of researchers have devoted themselves to the study of ether-free polyarylene-based AEMs [225,226].

Many state-of-art AEMs products were commercialized, including Fumasep® FAA3, Tokuyama A201, Aemion™, Sustainion® 37-50, DURION TM1, PiperION [227–232]. Their detailed technical properties are exhibited in Table 5. In general, they can be directly utilized as the alkaline electrolyzer after a feasible pretreatment in the KOH. Some excellent AEMWE performance has been reported based on these commercial membranes. For example, Kaczur*et al.* realized an AEM electrolyzer to reach 1 A cm^{-2} at a low cell voltage of 1.63 V based on the precious metal electrode by using a Sustainion® 37-50 and feeding 1 M KOH at 60 °C [233]. Such activity is comparable to the benchmark activity of PEMWE. However, to the best of our knowledge, the commercial AEMs still cannot realize long-term stability at 1 A cm^{-2} for > 3000 h (except for one report [234] from Motealleh *et al.*), which is mainly due to their chemical stability. In a strongly alkaline environment, the hydroxides tend to attack the backbone and functional groups of AEMs by various mechanisms such as nucleophilic substitution reactions and Hofmann elimination, leading to chain scission, deactivation, and degradation. Therefore, recent AEM research more focused on developing stable backbones (*e.g.*, aliphatic, or mixed aromatic/aliphatic, *etc.*), and reaching a balance between the ionic conductivity and functional groups stability.

4. Electrochemical analysis methods and characterizations of AEMWE

4.1. Polarization curve

The above sections have mentioned that the AEMWE performance largely depends on the inner factors such as catalyst, MEA configuration, *etc.*, and outer conditions including temperature, liquid flow rate, pressure, *etc.* Therefore, an AEM electrolyzer requires to be well-assembled and tested in a stable state to achieve repeatable performance. A sufficient cell pre-condition is also necessary before performance evaluation (detailed discussion is given in Section 4.5). For the AEMWE, the galvanostatic method (*i.e.*, chronopotentiometry, CP) has more advantages in precisely evaluating performance than the cyclic voltammetry (CV) and linear sweep voltammetry (LSV) methods (normally measure catalyst performance in three-electrode liquid cell systems with more favorable diffusion and transfer conditions). To be specific, at a high current density condition (> 0.2 A cm^{-2}), the cell performance measured by CV with a fast scan rate > 10 mV s^{-1} would be limited by the relative slow mass transfer process, where the fast voltage change doesn't allow the reacting system being stable, thus showing an inaccurate and less reproducible current-voltage real-time response. In contrast, the CP records the potential as a function of time at a fixed current, which can provide enough time for the potential to be stable. By applying multiple CPs to record the stable current-voltage response, the polarization curve of the cell can be achieved. It is worth mentioning that when the sweep speed of CV is slow enough (*e.g.*, 0.5 mV s^{-1}), it can fulfill the requirements of accurate performance evaluation, however, it may spend several hours to record one curve.

Fig. 16a shows the typical polarization curve of AEMWE (black dot-line curve), which is measured in the two-electrode electrolyzer by applying the galvanostatic method at variable current density steps (0.01-5 A cm^{-2}) and each step maintains 0.5~2 min to achieve a stable potential response [235]. The predicted cell voltage distribution is further plotted in Fig. 16a and divided into the reversible cell voltage (also called thermodynamic potential, 1.229 V at the normal condition), ohmic overpotential, and anode/cathode activation overpotentials. Among them, ohmic overpotential reflects the electrical and ionic resistance loss of membrane including the electrode, BPP, current collector, wire, *etc.*; anode and cathode activation overpotentials mainly depend on the catalyst activity and MEA behavior [78,89,236]. Based on the current density (j), the polarization curve can be further classified into three characteristic regions: (i) when $j < 0.2$ A cm^{-2}, the anode and cathode activation losses dominate the voltage loss; (ii) when $0.2 < j < 4$ A cm^{-2}, the resistance losses increase with the j and become significant; (iii) when $j > 4$ A cm^{-2}, the strong impact of mass-transport losses appears. Consequently, the vital insight of AEMWE can be acquired by establishing a relationship between the optimized inner/outer factors and the polarization curve in different regions.

4.2. Electrochemical impedance spectroscopy analysis

Electrochemical impedance spectroscopy (EIS), which records the impedance of an AEMWE system at different frequencies, can be used to identify and quantify the various losses that determine cell performance, such as ohmic loss, charge transfer loss, and mass transport loss [237]. EIS measures the frequency dependence of the impedance by applying a small alternating current/voltage in galvanostatic/potentiostatic mode. Nyquist plots are often used to evaluate electrochemical impedance data. Fitting the Nyquist plot yields an equivalent circuit (EEC), which gives a visual indication of the relative magnitude between the different resistances of the cell [237,238]. Generally, on the basis of the physical processes in the AEM electrolyzer, an appropriate EEC model is selected.

A typical ECC and its Nyquist plot with the fitting arcs of an AEMWE are shown in Fig. 16b [125]. The ECC is composed of an ohmic resistance (R_0) in series with an inductor (L) and three circuits (R_1, HER

Table 5
Commercial AEMs and their technical properties.

Company	Product series	Thickness (μm)	IEC (meq g^{-1})	Conductivity (mS cm^{-1})	ASR (Ω cm^2)	Reference
Fumatech	Fumasep® FAA3	25~75	1.39~2.1	> 40	0.3~2.5	Technical data sheet
Tokuyama	Tokuyama A201	28	1.8	42	na	
Ionomr	Aemion™	25~50	1.4~2.5	15~80	0.063~0.67	
Dioxide Materials	Sustainion® 37-50	50	1.2	80	0.045	
Orion Polymer	DURION TM1	5~50	2~2.3	>60	na	
Versogen	PiperION	15~80	2.35	150	na	

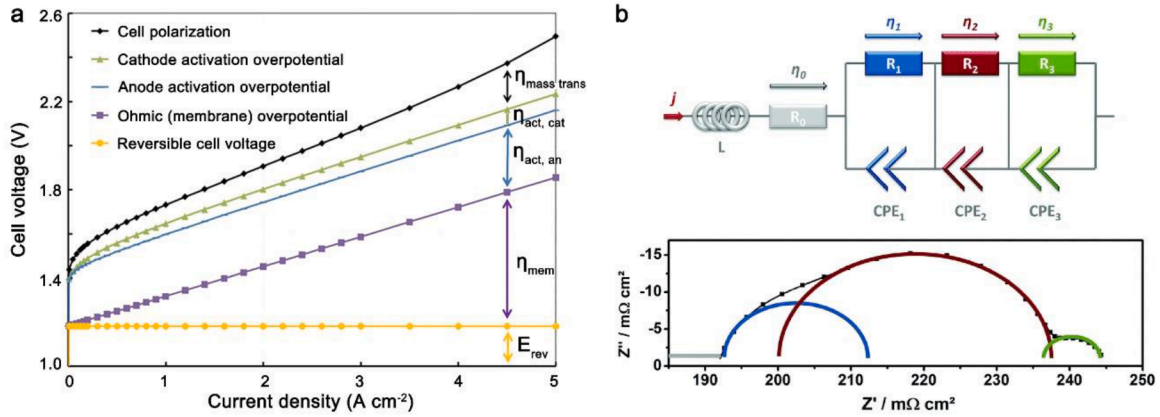

Fig. 16. (a) Potential distribution of polarization curves. Reproduced with permission.[235] Copyright 2017, Elsevier. (b) Equivalent circuit for analysis of the EIS. Reproduced with permission.[125] Copyright 2017, Royal Society of Chemistry.

charge transfer resistance, R_2, OER charge transfer resistance, and R_3, mass transport resistance, each in parallel with a resistor-constant phase element, CPE). L is related to cables and wires [134]. The CPE is linked to the double layer capacitance of the HER and the OER [134]. The R_0, the intercept point of the Nyquist plot with the x-axis at high frequencies, stands for the internal ohmic resistance of the cell, which is the sum of the contributions from the membrane, electrodes, GDLs, BPPs, and contact resistances [239]. The R_1 and R_2 obtained from fitting the semicircle in the middle frequency range of the Nyquist plot represent the charge transfer resistances for HER and OER, respectively [240]. The sluggish four-electron process of OER engenders a higher charge transfer resistance ($R_2 > R_1$). R_3 indicates the mass transfer limit, which is the small semicircle at the low frequency of the Nyquist plot. The mass transport issue is mainly subject to water/gas management dominated by the GDL structure [241]. A lack of efficient water delivery to the MEA and delayed removal of the generated gas will not only contribute to an uplifted mass transfer resistance but also entails high contact resistance and active site blockage, which in turn will add to the ohmic and charge transfer resistance, thus negatively damaging the cell performance [202]. Accordingly, the analysis of EIS can unveil the electrochemical reaction kinetics of the AEM electrolyzer, which can help to gain insight into the reaction mechanism and develop the next generation of AEMWE.

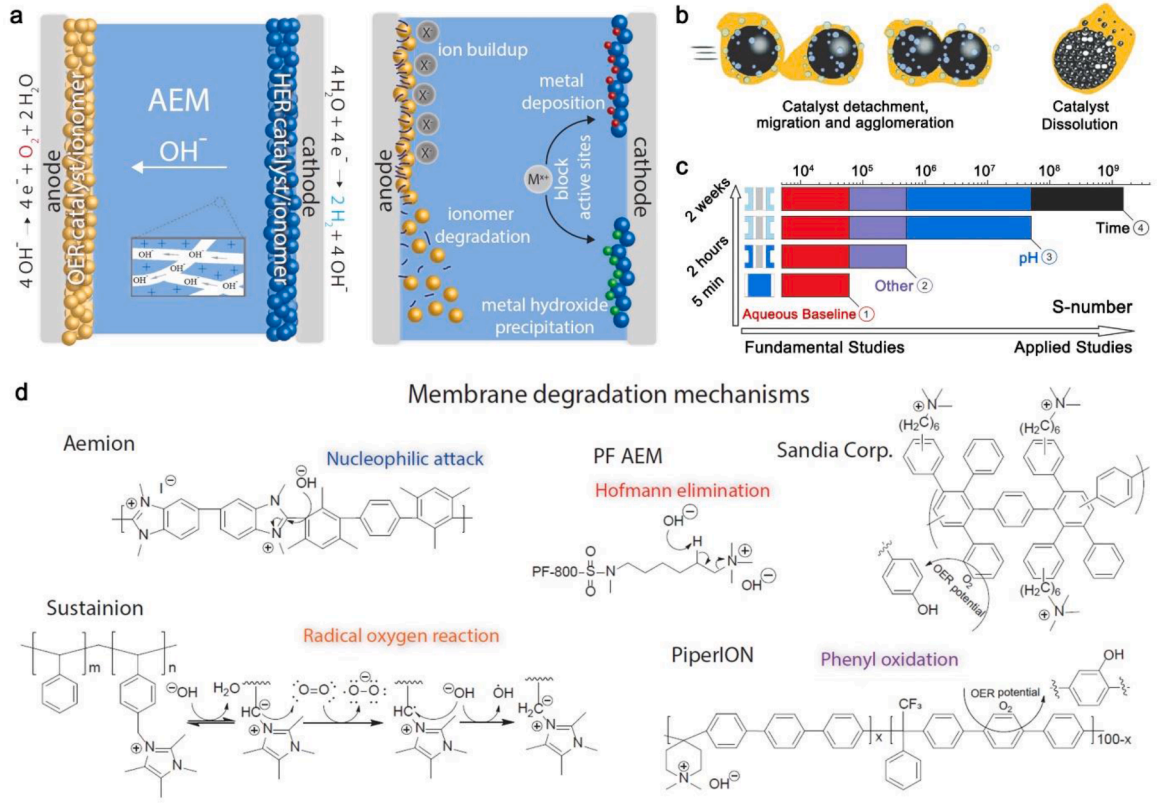

Fig. 17. (a) Degradation mechanisms in the AEM water electrolysis. Reproduced with permission.[242] Copyright 2020, Elsevier. (b) Catalyst degradation pathways under AEMWE operating conditions. Reproduced with permission.[207] Copyright 2021, Royal Society of Chemistry. (c) The scheme on the proposed main contributors to the dissolution discrepancy. Reproduced with permission.[27] Copyright 2021, Nature Publishing Group. (d) Possible anion-exchange membrane degradation mechanisms. Reproduced with permission.[242] Copyright 2020, Elsevier.

4.3. Stability and degradation mechanisms

Currently, the large-scale application of AEMWE is still impeded by its relatively poor durability. The best reported long-term stability was obtained by Motealleh *et al.* that their electrolyzer stably worked in 1.0 M KOH at 1 A cm^{-2} for > 11000 h with a degradation rate of 0.7 μV h^{-1} [234]. However, except this, all the other reported longevity of AEMWEs is no longer than 3000 h, indicating a long research way before reaching the commercialization threshold of AEMWE. Many durability-limiting factors and degradation mechanisms in the MEA have been proposed. Fig. 17a exhibits the potential degradation mechanisms in the MEA-based cell, such as catalyst degradation, membrane/ionomer degradation, *etc.* [242] At the anode side, different anions would buildup on the catalyst surface to prevent the OER and the strong oxidation conditions of OER would also cause the chemical instability of membrane and ionomer. On the cathode side, the catalyst inactivation including the *in-situ* electrochemical deposition of metal and the chemical precipitation of metal hydroxide would block active sites of catalysts. Moreover, catalyst degradation regarding the dissolution, detachment, migration, and agglomeration occurs on both sides due to the weak interaction at the catalyst-support interface and bad chemical stability of the catalyst, as shown in Fig. 17b [207]. At large current density, the fast formation, growth and evolution of H_2 and O_2 bubbles would apply strong capillary force to the adjacent catalyst, leading to the catalyst detachment and the activity loss. These detached nanoparticles subsequently migrate with the flow of electrolyte and may agglomerate to block the active sites, further aggravating the degradation. Catalyst dissolution is another severe problem in the AEMWE, especially for the anode. Some transition metals (Ni, Fe and Co) based catalysts and noble metal (Ir and Ru) based catalysts have been reported to dissolve in the alkaline and inactive during the operation [84,243]. Carbon-based supporting materials should avoid being used at the anode because they are easily oxidized and physically damaged under oxidation condition [244]. To qualify the catalyst degradation, an S-number metric, which was firstly developed in the acid OER field to compare the oxygen evolution content to the Ir dissolution content, was then further applied in the MEA field to evaluate the durability of the catalyst. A larger S-number suggests better durability of the catalyst. Cherevko and co-workers found the S-number measured in the MEA is an order of magnitude better than its value in the aqueous model systems, indicating the interfacial environment of MEA plays an important role in stabilizing the catalyst [27]. Furthermore, the influence of the electrolyte and the reading time on the S-number was explored, as displayed in Fig. 17c. They concluded that properly regulating the pH of electrolyte and timescale would extend catalyst durability as well as the S-number.

Furthermore, depending on the operating conditions (*e.g.,* electrolyte-feed and impurity), the AEMWE stability also causally changes according to the evolution of degradation mechanisms. Li *et al.* summarized and compared the durability-limiting factors for AEMWEs in three feed conditions (pure water, concentrated KOH and K_2CO_3) [207]. For the pure water-fed condition, the ionomer-related degradations including detachment and oxidation mainly determine the stability. In detail, the ionomeric binder with high water affinity would be flooded over reacting time and its phenyl groups inside the structure tend to be electrochemically oxidized. For the KOH-fed condition, the membrane-related degradations become the main contributor. Fig. 17d shows the possible AEM degradation mechanisms, such as a nucleophilic attack, Hofmann elimination, phenyl oxidation, and radical oxygen reactions, in differently structured membranes [242,245-248]. For the K_2CO_3-fed condition, more complicated degradation mechanisms are shown due to its combined environment with ample anions of OH and CO_3^{2-}/HCO_3^-. For example, the buffer effect of CO_3^{2-}/HCO_3^- would facilitate a local pH gradient in the MEA, causing an increase in relative polymer oxidation rate [249]. Besides, the impurity of electrolytes would also raise the risk of cell degradation. The cationic contaminants (Mg^{2+}, Ca^{2+}) would deposit on the cathode leading to the active sites block and mechanical failure [250]. The anionic contaminants (Cl^-, Br^-) could occur in the oxidation reaction at the anode due to the thermodynamical preference, competing with OER [251,252]. Therefore, developing catalysts and electrolysis systems with high tolerance to impurities could also improve the lifetimes of AEMWE.

4.4. In-situ electrochemical characterizations

To achieve an AEMWE system with high activity and long stability, *in-situ* electrochemical characterizations become crucial to analyze the failure cause of electrolyzer and explore a more advanced system [84,255,256]. For example, to evaluate the dissolution of catalysts, the online inductively coupled plasma mass spectrometry (ICP-MS) technique has been developed in recent years. Fig. 18a depicts an electrochemical scanning flow cell-based ICP-MS system that was established by Cherevko group [253]. This system can realize the simultaneous analyses of the CV curve and dissolution spectrogram of catalyst. Based on the multi-elemental analysis, weak metal elements in the alloy catalyst can also be quantified. Afterward, they further developed a GDE half-cell-based ICP-MS system to simulate the real conditions as close as possible. Their experiments found that low catalyst loading and the MEA technique both help to relieve the catalyst dissolution [257]. Moreover, the monitoring electrode potential is the most efficient way to proceed with the failure analysis. Normally, the potential distribution of an MEA-based electrolyzer can be achieved by introducing reference electrodes (REs) at each-side inlet flow of the electrolyte, thus the anodic reaction potentials, cathodic reaction potential and potential drop of the membrane can be separately recorded. In these cases, the concentrated electrolyte with the negligible solution resistance is required to feed in the system, assuming the potential signals of RE at the inlet are equal to that of at the electrode interface. However, for pure water electrolysis, the RE cannot be applied at the inlet because the liquid has no ionic conductivity. To overcome this, Xu *et al.* developed a pure-water AEMWE system that can integrate a reference electrode with the MEA, as shown in Fig. 18b [141]. The reference electrode is ionically "wired" into the membrane by an extended membrane strip to attach to the AEM edge. By using this technique, the anode and cathode potentials of the electrolyzer as well as their impedance were independently monitored. They reported that properly increasing the internal pressure of MEA is beneficial to both anode and cathode.

Furthermore, the *in-situ* X-ray absorption spectroscopy (XAS) technique gives the opportunity to detect the catalyst evaluation and functional state at the atomic level during the operating process [258–260]. Ampurdanés *et al.* designed an *operando* X-ray transparent electrolyzer by modifying the traditional one so that it can be used to probe the catalyst state [254]. Its scheme is shown in Fig. 18c. An ultrathin Kapton® (polyimide, 75 μm) film is served as an X-ray transparent window. Some regular pores also need to be drilled on the endplates, current collector and GDL. Based on these modifications, the X-ray can investigate the anode or cathode catalyst layer through either transmission or fluorescence mode. They explored the Co_3O_4-based materials as cathode catalysts in the electrolyzer. A dynamic conversion between Co^{3+} and Co^{2+} was observed to contribute to the improvement of HER performance. Besides, the *operando* X-ray computed tomography (CT) and X-ray radiography are useful to characterize the catalyst distribution, porosity of GDL and the water/gas bubble evolution during operation. An example of the custom-made micro-CT operando cell was displayed by Leonard *et al.*, as shown in Fig. 18d [144]. The MEA can be fully exposed to X-ray sources in both the in-plane and through-plane orientations. Micro-CT images verified that the better interfacial contact of CCM in contrast to that of CCS decreased the cell voltage by ~0.2 V at 1 A cm^{-2}.

4.5. Testing procedure

To reliably reproduce and compare single-cell AEMWE performance

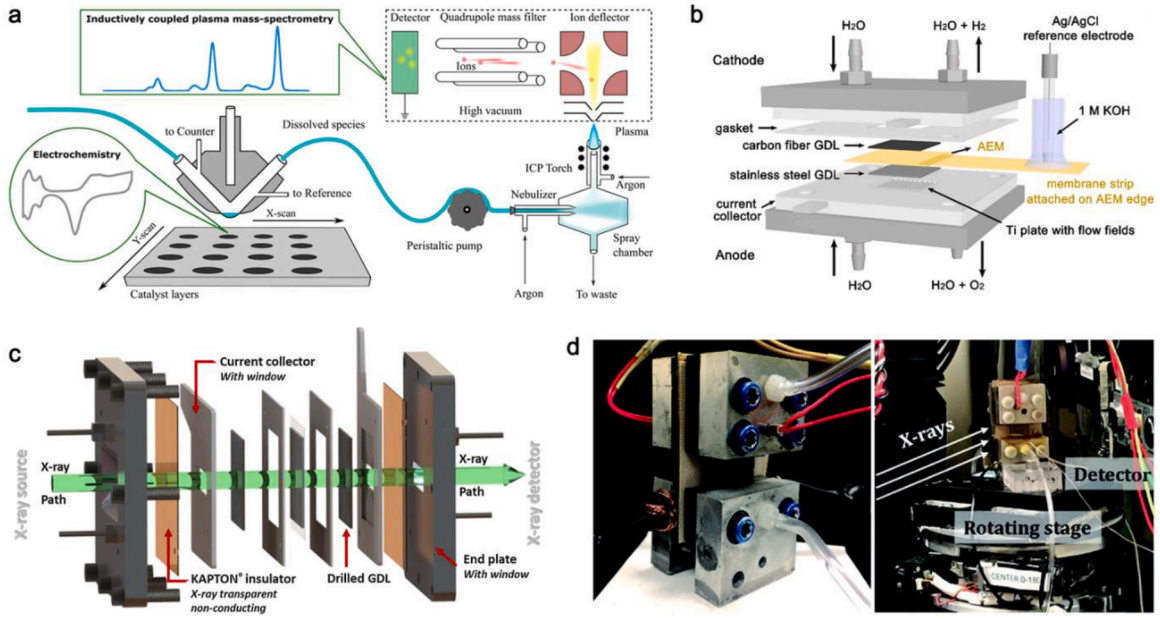

Fig. 18. (a) (a) A scheme of the scanning flow cell-based ICP-MS system. Reproduced with permission.[253] Copyright 2019, Wiley-VCH. (b) Schematic illustration of the integration of the reference electrode in the AEMWE system. Reproduced with permission.[141] Copyright 2021, American Chemical Society. (c) Kapton windows equipped electrolyzer to investigate the catalyst materials by *operando* XAS. Reproduced with permission. [254] Copyright 2019, Elsevier. (d) Digital photo of the micro-CT operando cell. Reproduced with permission.[144] Copyright 2020, Royal Society of Chemistry.

data between studies, we propose a protocol for single-cell AEMWE testing in this section [200,261]. A recommended testing flow diagram is illustrated in Fig. 19. The first is to assemble the AEM electrolyzer. Each component of MEA and hardware needs to be placed horizontally on the workbench and assembled layer by layer according to their relative position and orientation. Next, insert screws to fix the electrolyzer. Finally, connect the corresponding hardware according to Fig. 9 to construct water flow channels, gas flow channels, and electric circuits. Before operating the electrolyzer, N_2 is recommended to bubble into the liquid bucket to minimize the influence of CO_2 contamination; the electrolyte requires flowing through the electrolyzer to warm up the system to reach the target temperature; the electrolyte leakage, gas leakage, and electrical isolation need to be checked for safety [69,207]. The test can proceed when the temperature of the cell reaches a balanced state, and the open current voltage of the cell is at the normal level (at least > 1 mV). In the case of an open or short cell circuit being encountered during the test, the cell assembly can be modified considering the gasket thickness and screw torque. This is because these

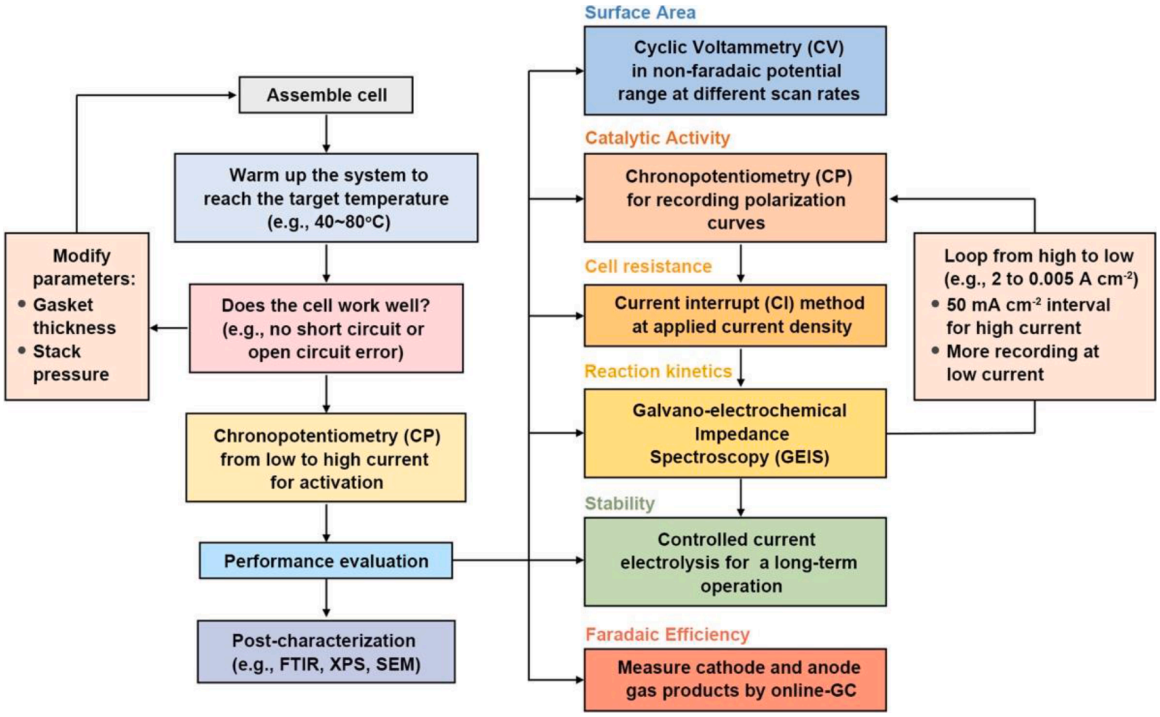

Fig. 19. A testing flow diagram for the lab-scaled AEM water electrolysis.

problems are caused mainly by the uneven internal pressure of the cell. A torque wrench is commonly used to tighten the screws to a fixed torque, and the proper size and number of gaskets are chosen to match with the GDL to ensure the even pressure of the stack [141].

The activation procedure is necessary for any MEA to properly humidify the electrolyte membrane and bring the performance to its highest and steady-state level [262]. The AEM electrolyzer is activated either by a multi-current test (typically 100 mA cm^{-2} to 1 A cm^{-2}, in 100 mA steps, for holding time 1-5 min at each step) until the voltage is relatively stabilized (variation < 1 mV min^{-1}) or by applying a constant voltage (typically in the range of 1.6-2.5 V) until the current is stabilized (variation < 1 mA min^{-1}) [118]. After pre-activation, some performance evaluation objects can be performed, including electrochemical active surface area, catalytic activity, cell resistance, reaction kinetics, stability, and faradaic efficiency. The surface area (SA) of the electrodes is normally estimated based on the electrochemical double-layer capacitance of the electrode (CDL) [263]. By using the reference electrode, adopting cyclic voltammetry tests in a non-faradaic potential range at different scan rates can evaluate the CDL of either anode or cathode. In addition, SA can also be evaluated by measuring the N_2 adsorption/-desorption isotherm with a specific surface area analyzer and calculating the specific surface area of the sample using the Brunauer-Emmett-Teller (BET) method. Current interrupt (CI) is a straightforward method to obtain cell resistance. The current-voltage polarization curve is the most direct response to the performance of the cell and is essential for any AEMWE. CP is recommended to obtain the polarization curve (specific reasons are explained in Section 4.1). Recording EIS data while measuring voltage-current response can shed better light on the reaction kinetics reflected by the polarization curve data points [206]. The following parameter settings are provided as a reference for readers: CP test in 2000 to 100 mA cm^{-2} (50 mA cm^{-2} interval), 80, 60, 50, 40, 20, 10, 5, mA cm^{-2}, held at each point for 2 minutes while measuring EIS with an amplitude of 5%×applied current density and from 100 kHz to 100 mHz [118,141,152]. More data are recorded at low currents in an attempt to evaluate the intrinsic activity of the catalyst. As a key metric for AEMWE, the stability of AEMWE is typically evaluated by the rate of voltage change during long-term CP testing (at least >10 h) or by accelerated stress testing (AST) with degradation acceleration parameters (*e.g.,* higher operating temperature, high current density).[64,207]. Faradaic efficiency of the cathode and anode gas products can be measured via *on-line* GC.

Post characterizations of electrodes, membranes, and solutions are necessary for analyzing and verifying the changes in cell performance [21]. For example, Fourier Transform Infrared Spectroscopy (FTIR) analysis of membranes can estimate the contribution of membrane degradation to performance [264]. By comparing the electrode morphology and surface chemical state before and after the test by scanning electron microscopy (SEM) and X-ray photoelectron spectroscopy (XPS) analysis, it can be inferred whether structural transformation, ion leaching and active phase conversion occurred during the catalyst reaction [60,259]. ICP-MS can help to evaluate the performance loss related to catalyst dissolution and contaminations.

5. Summary and outlooks

AEMWE emerging in this decade shows a great potential to produce green hydrogen. Although many signs of progress have been made, there is still a long way for AEMWE to realize commercialization. To allow researchers to enter this field easier and faster, in this review, we provided a comprehensive introduction to state-of-art AEMWE including the high-efficiency AEM electrocatalysts and electrode design, lab scaled testing system construction and operation guidelines, electrochemical analysis methods and evaluation protocols, *etc.*

Transition metal-based materials are low cost, environmentally friendly, and alkali resistant, rendering them commercially promising to substitute the PGMs as OER and HER catalysts in AEMWE applications. Regulating the oxidation state of transition metal oxides, constructing the layered structure of transition metal hydroxides, and designing transition metal (oxy)hydroxides based on surface reconstruction are effective strategies for designing powder OER catalysts. Alloying and constructing oxygen-incorporated composites are effective strategies to trigger high HER intrinsic activities. Moreover, the *in-situ* growth of electrocatalysts on conducting substrates to construct self-supported electrodes is a new trend for designing novel GDEs with high performance. On the other hand, advanced GDEs design with the optimized pore and interfacial chemistry has been wildly reported for pure water electrolysis. We conclude that an ideal GDE should have a smooth MPL surface, gradient pore size, high porosity, proper hydrophobicity, and electric conductivity for efficiently utilizing the catalyst and enhancing reaction kinetics.

For promoting the healthy development of AEMWE, a standardization process regarding the testing system and performance evaluation is necessary and urgent. Therefore, based on our summary and understanding, we provide a guideline for establishing the AEMWE system and a testing protocol to evaluate the cell performance. Detailed information containing the testing system configuration, electrolyzer and component selection, and ink-electrode preparation are elaborated. The influence of operating conditions such as the assemble torque, the pressure, temperature and the electrolyte and feed mode on cell performance are also discussed. Moreover, the function of normal electrochemical analysis methods and advanced *in-situ* characterizations for evaluating the activity and stability of the AEMWE were demonstrated. In the end, a testing flow diagram including pre-activation, troubleshooting cell assembly, measuring performance and post-characterizations is given to guide the beginner in this field.

In the future, two main challenges to impede the AEMWE progress need to be carefully considered, *i.e.,* how to reduce hydrogen price lower than \$2 kg^{-1} and improve cell performance superior to 1 A $^{cm-2@1.8}$ V and >10 kh durability [266]. Only if the AEMWE meets these requirements, it can be a cost-competitive technology compared to the incumbent technology and PEMWE. Based on the H2A analysis production model, many cost assessments about the AEMWE system were reported. [267] Lagadec and Grimaud analyzed the electrolysis system and electrolyzer stack cost change by scaling the system size and production, as shown in Fig. 20a [23]. For a normal system, the stack and balance of plant (BOP) respectively account for half the cost at a small scale. Among them, the BOP cost includes the power electronics, external circulation, and gas processing systems cost; the stack cost contains the endplates, MEA, BPPs and PTLs costs. When the system size and production rate increase, the total cost for both stack and system would decrease, indicating the great scalability of electrolysis technology. Moreover, the stack cost is dictated by the MEA and PTLs cost at a large scale, suggesting the high demands for developing high-performance and cost-efficient MEA and PTLs. Ionomr company wrote a White Paper focusing on the hydrogen production cost of AEMWE [265]. They investigated the reduction of the Levelized cost of hydrogen (LOCH) by optimizing the AEMWE system (Fig. 20b). It shows the current AEMWE baseline cost for producing hydrogen is ~\$3.7 kg^{-1}. This value can be optimized to ~\$3.2 kg^{-1} when reducing the 25% BOP cost and utilizing the non-platinum-group materials (non-PGM) as anode and cathode. Furthermore, by combining the electrolysis system with low-cost electricity from intermittent renewable energy, the LOCH can drop down to lower than ~\$1.8 kg^{-1} depending on the capacity factors (CF). In principle, the cell performance also has a large impact on the produced hydrogen cost. High activity with low applied voltage can decrease the electricity consumption and long durability can reduce the long-term unamortized expenses. Abbasi *et al.* studied the cost tradeoff based on performance and electrocatalyst (HER or OER) [20,43]. As shown in Fig. 20c, d, the lower overpotential and materials cost of electrocatalyst would largely reduce the hydrogen price. Their studies also showed that the NiFe LDH and Mo-based materials are the most potential non-PGM electrocatalysts for OER and HER, respectively. Besides, some feasibility analyses of AEMWE based

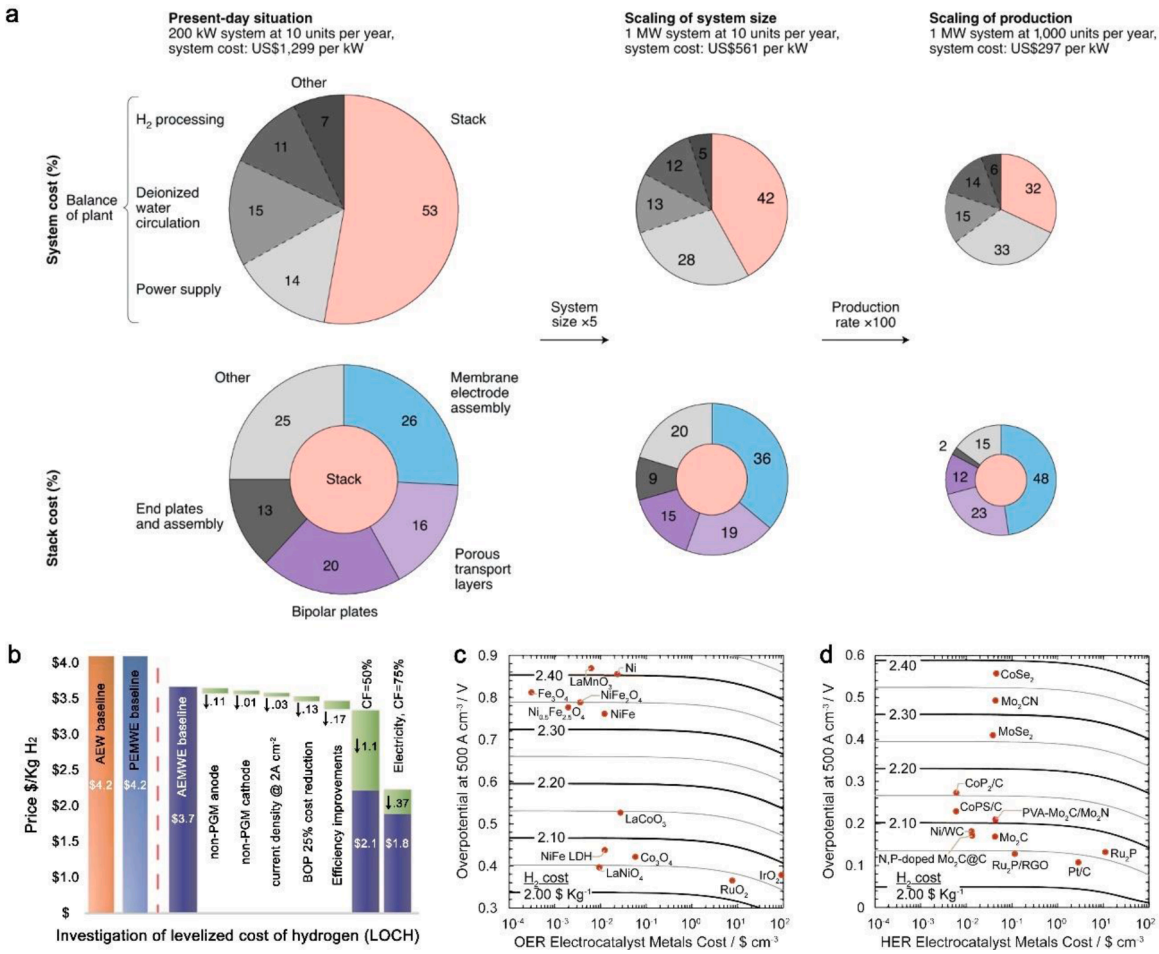

Fig. 20. (a) Breakdown of system and stack cost by scaling the system size and production. Reproduced with permission.[23] Copyright 2020, Nature Publishing Group. (b) Cost reduction of hydrogen production by optimizing the AEMWE system.[265] Copyright 2020, Ionomr Innovations Inc. (c, d) Contour plots of hydrogen production cost with the OER and HER electrocatalysts prices. Reproduced with permission.[20] Copyright 2019, Wiley-VCH.

on the utilization of low-purity water were reported [242,250,268]. This technical pathway expects to use impure water (*e.g.,* tap water, surface water or even seawater), which can extremely reduce the BOP cost and stack materials cost.

Further improving the cell performance (activity and stability) requires not only developing more superior membrane, catalyst and GDEs materials but also exploring and optimizing interfacial interaction between them. Anion-exchange ionomer (AEI) serving as ionic conductor and binder is the most important bridge across the AEM-catalyst layer interface. An ideal ionomer distribution and content help to make the electrolyzer display its best possible performance. Li *et al.* developed an ammonium-enriched AEI to extremely improve the pure water AEMWE performance (2.7 A cm^{-2} at 1.8 V) with the use of NiFe-based OER catalysts, reaching the state of art PGM-based PEMWE [269]. They concluded that such excellent performance comes from the high interfacial pH environment created by the AEI, which is favorable for both HER and OER. However, the stability of this cell is not as expected. The author speculated that ionomer degradation caused the catalyst particles' detachment during continuous operation. Moreover, Krivina *et al.* discussed the possible degradation mechanism of three commercial AEIs (Sustainion, Aemion, and PiperION) in several supporting electrolytes with different bulk pH [249]. They found that the ionomer conductivity, redox potential, and pH tolerance together governs the ionomer stability during OER. Therefore, more alkaline stable ionomers with robust polymer backbones and a high interfacial pH environment need to be further exploited. On the other hand, the electrochemical reconstruction of an anode catalyst during electrolysis would also influence the electrode interface. Many studies have reported that the transition-metal-based electrocatalysts (*e.g.,* chalcogenides, pnictides, and carbides) tend to be oxidized and reconstructed at the anode during the AEMWE (alkaline electrolyte, low-temperature, and current density < 0.2 A cm^{-2}), where the 'true' catalysts (normally are metal oxides/(oxy)hydroxides) would in-situ generate and play a positive effect on the performance [82]. However, such a conclusion may be not applicable when varying operation conditions (*e.g.*, anodic potential, electrolyte and reacting temperature) since the steady state component in the corresponding Pourbaix diagram would be changed accordingly. Recently, Boettcher and co-authors explored the degradation of five commercial anode catalysts for pure-water AEMWE [270]. They found the dynamic reconstruction of anode catalyst in the pure water would lead to the loss of active metal sites and thus enhance the degradation rates. The above discussions suggest more research should focus on in-situ monitoring of the real state evolution of catalysts and ionomer/catalyst interaction during electrolysis under different conditions.

In the above cases, although good interface and active catalysts are established initially, there still lacks *operando* characterization technology to precisely probe the interfacial structure inside the MEA and then implement the failure analysis. Therefore, we advocate developing more *in-situ* MEA-based electrochemical characterization reactors. Many advanced reactors in the fuel cell, PEM-based system and CO_2 reduction (CO_2R) field can be learned such as the *in-situ* Raman flow cell, *on-line* differential electrochemical mass spectroscopy (DEMS) cell, *etc.*[243, 271]. Besides, mass-transfer computations based on a multi-physic field (*e. g.* COMSOL) are an efficient strategy to guide the optimization of

MEA configuration and operation conditions for preventing useless experiments [272]. For example, by utilizing an MEA-based calculation modeling, Stanislaw *et al.* discovered that replacing electrolytes from KOH to K_2CO_3 decreased the catalyst utilization at the anode and thus results in an additional voltage loss [214]. In sum, we believe that the AEMWE has a bright future for producing green hydrogen while much more progress is still urgently needed.

CRediT authorship contribution statement

Qiucheng Xu: Writing – original draft, Writing – review & editing, Supervision. **Liyue Zhang:** Writing – original draft, Writing – review & editing. **Jiahao Zhang:** Writing – original draft. **Jingyu Wang:** Writing – review & editing. **Yanjie Hu:** Investigation, Writing – review & editing. **Hao Jiang:** Supervision, Writing – review & editing, Funding acquisition. **Chunzhong Li:** Supervision, Writing – review & editing, Funding acquisition.

Declaration of Competing Interest

There is no conflict of interest.

Acknowledgments

This work was supported by the National Natural Science Foundation of China (21838003), The National Program for Support of Top-Notch Young Professionals, and the Fundamental Research Funds for the Central Universities.

References

[1] B. Obama, The irreversible momentum of clean energy, Science 355 (2017) 126–129.
[2] P. De Luna, C. Hahn, D. Higgins, S.A. Jaffer, T.F. Jaramillo, E.H. Sargent, What would it take for renewably powered electrosynthesis to displace petrochemical processes? Science 364 (2019) 3506.
[3] J. Wei, R. Yao, Y. Han, Q. Ge, J. Sun, Towards the development of the emerging process of CO_2 heterogenous hydrogenation into high-value unsaturated heavy hydrocarbons, Chem. Soc. Rev. 50 (2021) 10764–10805.
[4] M. Ball, M. Wietschel, The future of hydrogen–opportunities and challenges, Int. J. Hydrog. Energy 34 (2009) 615–627.
[5] M. Chatenet, B.G. Pollet, D.R. Dekel, F. Dionigi, J. Deseure, P. Millet, R.D. Braatz, M.Z. Bazant, M. Eikerling, I. Staffell, Water electrolysis: from textbook knowledge to the latest scientific strategies and industrial developments, Chem. Soc. Rev. 51 (2022) 4583–4762.
[6] The Future of Hydrogen: Seizing Today's Opportunities, International Energy Agency, Paris, France, 2019.
[7] P. Sun, B. Young, A. Elgowainy, Z. Lu, M. Wang, B. Morelli, T. Hawkins, Criteria air pollutants and greenhouse gas emissions from hydrogen production in US steam methane reforming facilities, Environ. Sci. Technol. 53 (2019) 7103–7113.
[8] T. Bacquart, K. Arrhenius, S. Persijn, A. Rojo, F. Auprêtre, B. Gozlan, N. Moore, A. Morris, A. Fischer, A. Murugan, Hydrogen fuel quality from two main production processes: Steam methane reforming and proton exchange membrane water electrolysis, J. Power Sources 444 (2019), 227170.
[9] M. Carmo, D.L. Fritz, J. Mergel, D. Stolten, A comprehensive review on PEM water electrolysis, Int. J. Hydrog. Energy 38 (2013) 4901–4934.
[10] M.W. Kanan, Y. Surendranath, D.G. Nocera, Cobalt–phosphate oxygen-evolving compound, Chem. Soc. Rev. 38 (2009) 109–114.
[11] The national hydrogen strategy, German Federal Ministry for Economic Affairs and Energy, Berlin, Germany, 2020.
[12] M. Menezes, D. Simmons, S. Winberg, R. Baranwal, P. Hoffman, C. Fall, S. Gentaowski, Department of energy hydrogen program plan, US Department of Energy (USDOE), United States, 2021.
[13] M. Atanasiu, D. Tsimis, L. Boillot, Overview on the European FCH Joint Undertaking Projects & Activities in PEM Fuel Cells and Electrolysis, ECS Meet, Abs. 38 (2019), 1762-1762.
[14] A. Majumdar, J.M. Deutch, R.S. Prasher, T.P. Griffin, A framework for a hydrogen economy Comment, Joule 5 (2021) 1905–1908.
[15] T. Smolinka, H. Bergmann, J. Garche, M. Kusnezoff, The history of water electrolysis from its beginnings to the present. Electrochemical Power Sources: Fundamentals, Systems, and Applications, Elsevier, 2022, pp. 83–164.
[16] R.S. Nicholson, Theory and application of cyclic voltammetry for measurement of electrode reaction kinetics, Anal. Chem. 37 (1965) 1351–1355.
[17] K. Zeng, D.K. Zhang, Recent progress in alkaline water electrolysis for hydrogen production and applications, Prog Energ Combust 36 (2010) 307–326.
[18] P. Trinke, B. Bensmann, R. Hanke-Rauschenbach, Experimental evidence of increasing oxygen crossover with increasing current density during PEM water electrolysis, Electrochem. Commun. 82 (2017) 98–102.
[19] C. Spoeri, J.T.H. Kwan, A. Bonakdarpour, D.P. Wilkinson, P. Strasser, The stability challenges of oxygen evolving catalysts: towards a common fundamental understanding and mitigation of catalyst degradation, Angew Chem Int Edit 56 (2017) 5994–6021.
[20] R. Abbasi, B.P. Setzler, S.S. Lin, J.H. Wang, Y. Zhao, H. Xu, B. Pivovar, B.Y. Tian, X. Chen, G. Wu, et al., A Roadmap to Low-Cost Hydrogen with Hydroxide Exchange Membrane Electrolyzers, Adv Mater 31 (2019), 1805876.
[21] N. Du, C. Roy, R. Peach, M. Turnbull, S. Thiele, C. Bock, Anion-Exchange Membrane Water Electrolyzers, Chem. Rev. (2022).
[22] Y. Liu, P. Vijayakumar, Q. Liu, T. Sakthivel, F. Chen, Z. Dai, Shining Light on Anion-Mixed Nanocatalysts for Efficient Water Electrolysis: Fundamentals, Progress, and Perspectives, Nanomicro Lett 14 (2022) 43.
[23] M.F. Lagadec, A. Grimaud, Water electrolysers with closed and open electrochemical systems, Nat Mater 19 (2020) 1140–1150.

This work highlighted how to accelerate the fundamental research of water electrolysis to achieve industry-scale deployment

[24] S.Z. Oener, M.J. Foster, S.W. Boettcher, Accelerating water dissociation in bipolar membranes and for electrocatalysis, Science 369 (2020) 1099–1103.
[25] L. Sun, Q. Luo, Z. Dai, F. Ma, Material libraries for electrocatalytic overall water splitting, Coord. Chem. Rev. 444 (2021), 214049.
[26] T. Lazaridis, B.M. Stuhmeier, H.A. Gasteiger, H.A. El-Sayed, Capabilities and limitations of rotating disk electrodes versus membrane electrode assemblies in the investigation of electrocatalysts, Nat Catal 5 (2022) 363–373.
[27] J. Knöppel, M. Möckl, D. Escalera-López, K. Stojanovski, M. Bierling, T. Böhm, S. Thiele, M. Rzepka, S. Cherevko, On the limitations in assessing stability of oxygen evolution catalysts using aqueous model electrochemical cells, Nat. Commun. 12 (2021) 2231.
[28] N.U. Hassan, Y. Zheng, P.A. Kohl, W.E. Mustain, KOH vs Deionized Water Operation in Anion Exchange Membrane Electrolyzers, J. Electrochem. Soc. 169 (2022), 044526.
[29] Z.W. Seh, J. Kibsgaard, C.F. Dickens, I.B. Chorkendorff, J.K. Norskov, T. F. Jaramillo, Combining theory and experiment in electrocatalysis: Insights into materials design, Science 355 (2017) eaad4998.
[30] D. Siegmund, S. Metz, V. Peinecke, T.E. Warner, C. Cremers, A. Greve, T. Smolinka, D. Segets, U.P. Apfel, Crossing the Valley of Death: From Fundamental to Applied Research in Electrolysis, JACS Au 1 (2021) 527–535.
[31] F.Y. Chen, Z.Y. Wu, Z. Adler, H.T. Wang, Stability challenges of electrocatalytic oxygen evolution reaction: From mechanistic understanding to reactor design, Joule 5 (2021) 1704–1731.
[32] X.H. Xie, L. Du, L.T. Yon, S.Y. Park, Y. Qiu, J. Sokolowski, W. Wang, Y.Y. Shao, Oxygen Evolution Reaction in Alkaline Environment: Material Challenges and Solutions, Adv Funct Mater 32 (2022).
[33] N.T. Suen, S.F. Hung, Q. Quan, N. Zhang, Y.J. Xu, H.M. Chen, Electrocatalysis for the oxygen evolution reaction: recent development and future perspectives, Chem. Soc. Rev. 46 (2017) 337–365.
[34] K.K. Huang, Y. Sun, Y. Zhang, X.Y. Wang, W. Zhang, S.H. Feng, Hollow-Structured Metal Oxides as Oxygen-Related Catalysts, Adv Mater 31 (2019), 1801430.
[35] F. Song, L.C. Bai, A. Moysiadou, S. Lee, C. Hu, L. Liardet, X.L. Hu, Transition Metal Oxides as Electrocatalysts for the Oxygen Evolution Reaction in Alkaline Solutions: An Application-Inspired Renaissance, J Am Chem Soc 140 (2018) 7748–7759.
[36] K.X. Zhang, R.Q. Zou, Advanced Transition Metal-Based OER Electrocatalysts: Current Status, Opportunities, and Challenges, Small 17 (2021), 2100129.
[37] C.Y. Kwon, J.Y. Jeong, J.C. Yang, Y.S. Park, J. Jeong, H. Park, Y.D. Kim, K.S. Moon, S.M. Choi, Effect of Copper Cobalt Oxide Composition on Oxygen Evolution Electrocatalysts for Anion Exchange Membrane Water Electrolysis, Front Chem 8 (2020), 600908.
[38] M.J. Jang, J. Yang, J. Lee, Y.S. Park, J. Jeong, S.M. Park, J.Y. Jeong, Y.D. Yin, M. H. Seo, S.M. Choi, et al., Superior performance and stability of anion exchange membrane water electrolysis: pH-controlled copper cobalt oxide nanoparticles for the oxygen evolution reaction, J Mater Chem A 8 (2020) 4290–4299.
[39] H. Koshikawa, H. Murase, T. Hayashi, K. Nakajima, H. Mashiko, S. Shiraishi, Y. Tsuji, Single Nanometer-Sized NiFe-Layered Double Hydroxides as Anode Catalyst in Anion Exchange Membrane Water Electrolysis Cell with Energy Conversion Efficiency of 74.7% at 1.0 A cm^{-2}, ACS Catalysis 10 (2020) 1886–1893.
[40] S.S. Jeon, J. Lim, P.W. Kang, J.W. Lee, G. Kang, H. Lee, Design Principles of NiFe-Layered Double Hydroxide Anode Catalysts for Anion Exchange Membrane Water Electrolyzers, Acs Appl Mater Inter 13 (2021) 37179–37186.
[41] J. Abed, S. Ahmadi, L. Laverdure, A. Abdellah, C.P. O'Brien, K. Cole, P. Sobrinho, D. Sinton, D. Higgins, N.J. Mosey, et al., In Situ Formation of Nano Ni-Co Oxyhydroxide Enables Water Oxidation Electrocatalysts Durable at High Current Densities, Adv Mater 33 (2021), 2103812.
[42] Y.H. Song, B.S. Xu, T. Liao, J.J. Guo, Y.C. Wu, Z.Q. Sun, Electronic Structure Tuning of 2D Metal (Hydr)oxides Nanosheets for Electrocatalysis, Small 17 (2021), 2002240.
[43] C. Li, J.-B. Baek, The promise of hydrogen production from alkaline anion exchange membrane electrolyzers, Nano Energy 87 (2021), 106162.
[44] M.Q. Zhao, Q. Zhang, J.Q. Huang, F. Wei, Hierarchical Nanocomposites Derived from Nanocarbons and Layered Double Hydroxides - Properties, Synthesis, and Applications, Adv Funct Mater 22 (2012) 675–694.

[45] J. Yu, F. Yu, M.F. Yuen, C.D Wang, Two-dimensional layered double hydroxides as a platform for electrocatalytic oxygen evolution, J Mater Chem A 9 (2021) 9389–9430.

[46] Z.Y. Yu, Y. Duan, X.Y. Feng, X.X. Yu, M.R. Gao, S.H. Yu, Clean and Affordable Hydrogen Fuel from Alkaline Water Splitting: Past, Recent Progress, and Future Prospects, Adv Mater 33 (2021), 2007100.

[47] S.W. Zuo, Z.P. Wu, H.B. Zhang, X.W. Lou, Operando Monitoring and Deciphering the Structural Evolution in Oxygen Evolution Electrocatalysis, Adv Energy Mater 12 (2022), 2103383.

[48] Q. Xu, H. Jiang, X. Duan, Z. Jiang, Y. Hu, S.W. Boettcher, W. Zhang, S. Guo, C. Li, Fluorination-enabled reconstruction of NiFe electrocatalysts for efficient water oxidation, Nano Lett 21 (2020) 492–499.

[49] Q. Xu, M. Chu, M. Liu, J. Zhang, H. Jiang, C. Li, Fluorine-triggered surface reconstruction of Ni_3S_2 electrocatalysts towards enhanced water oxidation, Chem. Eng. J 411 (2021), 128488.

[50] P.Z. Chen, X.L. Hu, High-Efficiency Anion Exchange Membrane Water Electrolysis Employing Non-Noble Metal Catalysts, Adv Energy Mater 10 (2020), 2002285.

[51] X.X. Zou, Y. Zhang, Noble metal-free hydrogen evolution catalysts for water splitting, Chem. Soc. Rev. 44 (2015) 5148–5180.

[52] M. Gong, D.Y. Wang, C.C. Chen, B.J. Hwang, H.J. Dai, A mini review on nickel-based electrocatalysts for alkaline hydrogen evolution reaction, Nano Res 9 (2016) 28–46.

[53] Y. Zheng, Y. Jiao, A. Vasileff, S.Z. Qiao, The Hydrogen Evolution Reaction in Alkaline Solution: From Theory, Single Crystal Models, to Practical Electrocatalysts, Angew Chem Int Edit 57 (2018) 7568–7579.

[54] Z. Yang, W. Gao, Applications of Machine Learning in Alloy Catalysts: Rational Selection and Future Development of Descriptors, Adv Sci 9 (2022), 2106043.

[55] J. Kim, H. Jung, S.M. Jung, J. Hwang, D.Y. Kim, N. Lee, K.S. Kim, H. Kwon, Y. T. Kim, J.W. Han, et al., Tailoring Binding Abilities by Incorporating Oxophilic Transition Metals on 3D Nanostructured Ni Arrays for Accelerated Alkaline Hydrogen Evolution Reaction, J Am Chem Soc 143 (2021) 1399–1408.

[56] J. Wang, S. Xin, Y. Xiao, Z. Zhang, Z. Li, W. Zhang, C. Li, R. Bao, J. Peng, J. Yi, et al., Manipulating the Water Dissociation Electrocatalytic Sites of Bimetallic Nickel-Based Alloys for Highly Efficient Alkaline Hydrogen Evolution, Angew Chem Int Edit 61 (2022), e202202518.

[57] S. Kamali, M. Zhiani, H. Tavakol, Synergism effect of first row transition metals in experimental and theoretical activity of NiM/rGO alloys at hydrogen evolution reaction in alkaline electrolyzer, Renew Energ 154 (2020) 1122–1131.

[58] L. Zhao, Y. Zhang, Z.L. Zhao, Q.H. Zhang, L.B. Huang, L. Gu, G. Lu, J.S. Hu, L. J. Wan, Steering elementary steps towards efficient alkaline hydrogen evolution via size-dependent Ni/NiO nanoscale heterosurfaces, Natl Sci Rev 7 (2020) 27–36.

[59] Q. Xu, H. Jiang, H. Zhang, Y. Hu, C. Li, Heterogeneous interface engineered atomic configuration on ultrathin Ni $(OH)_2/Ni_3S_2$ nanoforests for efficient water splitting, Appl Catal B-Environ 242 (2019) 60–66.

[60] Y.S. Park, J. Jeong, Y. Noh, M.J. Jang, J. Lee, K.H. Lee, D.C. Lim, M.H. Seo, W. B. Kim, J.C. Yang, et al., Commercial anion exchange membrane water electrolyzer stack through non-precious metal electrocatalysts, Appl Catal B-Environ 292 (2021), 120170.

[61] D. Chanda, S. Basu, Electrochemical synthesis of Li-doped NiFeCo oxides for efficient catalysis of the oxygen evolution reaction in an alkaline environment, Int. J. Hydrog. Energy 43 (2018) 21999–22011.

[62] M.H. Wang, Z.X. Lou, X.F. Wu, Y.W. Liu, J.Y. Zhao, K.Z. Sun, W.X. Li, J.C. Chen, H. Y. Yuan, M.H. Zhu, et al., Operando High-Valence Cr-Modified NiFe Hydroxides for Water Oxidation, Small 18 (2022), 2200303.

[63] I. Vincent, E.C. Lee, H.M. Kim, Highly cost-effective platinum-free anion exchange membrane electrolysis for large scale energy storage and hydrogen production, Rsc Adv 10 (2020) 37429–37438.

[64] A.Y. Faid, A.O. Barnett, F. Seland, S. Sunde, NiCu mixed metal oxide catalyst for alkaline hydrogen evolution in anion exchange membrane water electrolysis, Electrochim Acta 371 (2021), 137837.

[65] H.M. Sun, Z.H. Yan, F.M. Liu, W.C. Xu, F.Y. Cheng, J. Chen, Self-Supported Transition-Metal-Based Electrocatalysts for Hydrogen and Oxygen Evolution, Adv Mater 32 (2020), 1806326.

[66] P.C. Wang, B.G. Wang, Designing Self-Supported Electrocatalysts for Electrochemical Water Splitting: Surface/Interface Engineering toward Enhanced Electrocatalytic Performance, Acs Appl Mater Inter 13 (2021) 59593–59617.

[67] T.Y. Ma, S. Dai, S.Z. Qiao, Self-supported electrocatalysts for advanced energy conversion processes, Mater Today 19 (2016) 265–273.

[68] J.L. Liu, D.D. Zhu, Y. Zheng, A. Vasileff, S.Z. Qiao, Self-Supported Earth-Abundant Nanoarrays as Efficient and Robust Electrocatalysts for Energy-Related Reactions, Acs Catal 8 (2018) 6707–6732.

[69] E. Lopez-Fernandez, C. Gomez-Sacedon, J. Gil-Rostra, J.P. Espinos, A.R. Gonzalez-Elipe, F. Yubero, A. de Lucas-Consuegra, Ionomer-Free Nickel-Iron bimetallic electrodes for efficient anion exchange membrane water electrolysis, Chem. Eng. J 433 (2022), 133774.

[70] L. Wang, T. Weissbach, R. Reissner, A. Ansar, A.S. Gago, S. Holdcroft, K. A. Friedrich, High Performance Anion Exchange Membrane Electrolysis Using Plasma-Sprayed, Non-Precious-Metal Electrodes, Acs Appl Energ Mater 2 (2019) 7903–7912.

[71] P. Ganesan, A. Sivanantham, S. Shanmugam, Nanostructured Nickel-Cobalt-Titanium Alloy Grown on Titanium Substrate as Efficient Electrocatalyst for Alkaline Water Electrolysis, Acs Appl Mater Inter 9 (2017) 12416–12426.

[72] Y.S. Park, M.J. Jang, J. Jeong, S.M. Park, X. Wang, M.H. Seo, S.M. Choi, J. Yang, Hierarchical Chestnut-Burr Like Structure of Copper Cobalt Oxide Electrocatalyst Directly Grown on Ni Foam for Anion Exchange Membrane Water Electrolysis, Acs Sustain Chem Eng 8 (2020) 2344–2349.

[73] K. Ham, S. Hong, S. Kang, K. Cho, J. Lee, Extensive Active-Site Formation in Trirutile $CoSb_2O_6$ by Oxygen Vacancy for Oxygen Evolution Reaction in Anion Exchange Membrane Water Splitting, Acs Energy Lett 6 (2021) 364–370.

[74] J. Lee, H. Jung, Y.S. Park, S. Woo, N. Kwon, Y. Xing, S.H. Oh, S.M. Choi, J.W. Han, B Lim, Corrosion-engineered bimetallic oxide electrode as anode for high-efficiency anion exchange membrane water electrolyzer, Chem. Eng. J 420 (2021), 127670.

[75] K.Y. Zhu, F. Shi, X.F. Zhu, W.S. Yang, The roles of oxygen vacancies in electrocatalytic oxygen evolution reaction, Nano Energy 73 (2020), 104761.

[76] Q. Xu, H. Jiang, H. Zhang, H. Jiang, C. Li, Phosphorus-driven mesoporous Co_3O_4 nanosheets with tunable oxygen vacancies for the enhanced oxygen evolution reaction, Electrochim Acta 259 (2018) 962–967.

[77] J. Zhang, Q. Xu, J. Wang, Y. Li, H. Jiang, C. Li, Dual-defective Co_3O_4 nanoarrays enrich target intermediates and promise high-efficient overall water splitting, Chem. Eng. J 424 (2021), 130328.

[78] Y.S. Park, J. Yang, J. Lee, M.J. Jang, J. Jeong, W.-S. Choi, Y. Kim, Y. Yin, M.H. Seo, Z. Chen, et al., Superior performance of anion exchange membrane water electrolyzer: Ensemble of producing oxygen vacancies and controlling mass transfer resistance, Appl Catal B-Environ 278 (2020), 119276.

[79] J.J. Song, C. Wei, Z.F. Huang, C.T. Liu, L. Zeng, X. Wang, Z.C.J. Xu, A review on fundamentals for designing oxygen evolution electrocatalysts, Chem. Soc. Rev. 49 (2020) 2196–2214.

[80] J. Lee, H. Jung, Y.S. Park, S. Woo, J. Yang, M.J. Jang, J. Jeong, N. Kwon, B. Lim, J. W. Han, et al., High-Efficiency Anion-Exchange Membrane Water Electrolyzer Enabled by Ternary Layered Double Hydroxide Anode, Small 17 (2021), 2100639.

[81] J.E. Park, S. Park, M.-J. Kim, H. Shin, S.Y. Kang, Y.-H. Cho, Y.-E. Sung, Three-Dimensional Unified Electrode Design Using a NiFeOOH Catalyst for Superior Performance and Durable Anion-Exchange Membrane Water Electrolyzers, Acs Catal 12 (2022) 135–145.

[82] B.R. Wygant, K. Kawashima, C.B. Mullins, Catalyst or Precatalyst? The Effect of Oxidation on Transition Metal Carbide, Pnictide, and Chalcogenide Oxygen Evolution Catalysts, Acs Energy Lett 3 (2018) 2956–2966.

[83] C. Lei, F. Yang, N. Macauley, M. Spinetta, G. Purdy, J. Jankovic, D.A. Cullen, K. L. More, Y.S. Kim, H. Xu, Impact of Catalyst Ink Dispersing Solvent on PEM Fuel Cell Performance and Durability, J. Electrochem. Soc. 168 (2021), 044517.

[84] K.H. Yue, J.L. Liu, Y.T. Zhu, C.F. Xia, P. Wang, J.W. Zhang, Y. Kong, X.Y. Wang, Y. Yan, B.Y.In Xia, situ ion-exchange preparation and topological transformation of trimetal-organic frameworks for efficient electrocatalytic water oxidation, Energ Environ Sci 14 (2021) 6546–6553.

[85] Q.L. Wen, K. Yang, D.J. Huang, G. Cheng, X.M. Ai, Y.W. Liu, J.K. Fang, H.Q. Li, L. Yu, T.Y. Zhai, Schottky Heterojunction Nanosheet Array Achieving High-Current-Density Oxygen Evolution for Industrial Water Splitting Electrolyzers, Adv Energy Mater 11 (2021), 2102353.

[86] G.Q. Zhao, K. Rui, S.X. Dou, W.P Sun, Boosting electrochemical water oxidation: the merits of heterostructured electrocatalysts, J Mater Chem A 8 (2020) 6393–6405.

[87] Y. Zhao, S.Z. Wei, K.M. Pan, Z.L. Dong, B. Zhang, H.H. Wu, Q.B. Zhang, J.P. Lin, H Pang, Self-supporting transition metal chalcogenides on metal substrates for catalytic water splitting, Chem. Eng. J 421 (2021), 129645.

[88] Y.S. Park, J.H. Lee, M.J. Jang, J. Jeong, S.M. Park, W.S. Choi, Y. Kim, J. Yang, S. M. Choi, Co_3S_4 nanosheets on Ni foam via electrodeposition with sulfurization as highly active electrocatalysts for anion exchange membrane electrolyzer, Int. J. Hydrog. Energy 45 (2020) 36–45.

[89] W.W. Guo, J. Kim, H. Kim, S.H. Ahn, Direct electrodeposition of Ni-Co-S on carbon paper as an efficient cathode for anion exchange membrane water electrolysers, Int J Energ Res 45 (2021) 1918–1931.

[90] J.F. Callejas, C.G. Read, C.W. Roske, N.S. Lewis, R.E. Schaak, Synthesis, Characterization, and Properties of Metal Phosphide Catalysts for the Hydrogen-Evolution Reaction, Chem Mater 28 (2016) 6017–6044.

[91] Y.M. Shi, B. Zhang, Recent advances in transition metal phosphide nanomaterials: synthesis and applications in hydrogen evolution reaction, Chem. Soc. Rev. 45 (2016), 1781-1781.

[92] J.-C. Kim, J. Kim, J.C. Park, S.H. Ahn, D.-W. Kim, Ru_2P nanofibers for high-performance anion exchange membrane water electrolyzer, Chem. Eng. J 420 (2021), 130491.

[93] T. Liang, S. Lenus, A. Wang, T. Sakthivel, J. Xie, Z. Dai, Casting light on black phosphorus-based catalysts for water electrolysis: Approaches, promotion manners, and perspectives, J. Environ. Chem. Eng. 10 (2022), 108018.

[94] W. Guo, J. Kim, H. Kim, S.H. Ahn, Cu-Co-P electrodeposited on carbon paper as an efficient electrocatalyst for hydrogen evolution reaction in anion exchange membrane water electrolyzers, Int. J. Hydrog. Energy 46 (2021) 19789–19801.

[95] J. Lee, H. Jung, Y.S. Park, N. Kwon, S. Woo, N.C.S. Selvam, G.S. Han, H.S. Jung, P. J. Yoo, S.M. Choi, et al., Chemical transformation approach for high-performance ternary NiFeCo metal compound-based water splitting electrodes, Appl Catal B-Environ 294 (2021), 120246.

[96] L. Wan, Z. Xu, P.C. Wang, P.F. Liu, Q. Xu, B.G Wang, Dual regulation both intrinsic activity and mass transport for self-supported electrodes using in anion exchange membrane water electrolysis, Chem. Eng. J 431 (2022), 133942.

[97] H. Su, M.A. Soldatov, V. Roldugin, Q. Liu, Platinum single-atom catalyst with self-adjustable valence state for large-current-density acidic water oxidation, eScience 2 (2022) 102–109.

[98] X. Guo, X. Wan, Q. Liu, Y. Li, W. Li, J. Shui, Phosphated IrMo bimetallic cluster for efficient hydrogen evolution reaction, eScience 2 (2022) 304–310.

[99] Q. Xu, Y. Liu, H. Jiang, Y. Hu, H. Liu, C. Li, Unsaturated Sulfur Edge Engineering of Strongly Coupled MoS_2 Nanosheet–Carbon Macroporous Hybrid Catalyst for Enhanced Hydrogen Generation, Adv Energy Mater 9 (2019), 1802553.

[100] J. Zhang, H. Zhang, M. Liu, Q. Xu, H. Jiang, C. Li, Cobalt-stabilized oxygen vacancy of V_2O_5 nanosheet arrays with delocalized valence electron for alkaline water splitting, Chem. Eng. Sci. 227 (2020), 115915.
[101] C. Xie, D. Yan, W. Chen, Y. Zou, R. Chen, S. Zang, Y. Wang, X. Yao, S. Wang, Insight into the design of defect electrocatalysts: From electronic structure to adsorption energy, Mater Today 31 (2019) 47–68.
[102] X. Chen, M. Yu, Z. Yan, W. Guo, G. Fan, Y. Ni, J. Liu, W. Zhang, W. Xie, F. Cheng, et al., Boosting Electrocatalytic Oxygen Evolution by Cation Defect Modulation via Electrochemical Etching, CCS Chem 3 (2021) 675–685.
[103] Q. Xu, J. Zhang, H. Zhang, L. Zhang, L. Chen, Y. Hu, H. Jiang, C. Li, Atomic heterointerface engineering overcomes the activity limitation of electrocatalysts and promises highly-efficient alkaline water splitting, Energ Environ Sci 14 (2021) 5228–5259.

This work provided some insights about the heterointerface engineering of electrocatalyst

[104] H. Liu, Z. Yan, X. Chen, J. Li, L. Zhang, F. Liu, G. Fan, F. Cheng, Electrodeposition of Pt-Decorated $Ni(OH)_2/CeO_2$ Hybrid as Superior Bifunctional Electrocatalyst for Water Splitting, Research 2020 (2020), 9068270.
[105] E. Lopez-Fernandez, J. Gil-Rostra, J.P. Espinos, A.R. Gonzalez-Elipe, F. Yubero, A. de Lucas-Consuegra, $Cu_xCo_{3-x}O_4$ ultra-thin film as efficient anodic catalysts for anion exchange membrane water electrolysers, J. Power Sources 415 (2019) 136–144.
[106] E. Lopez-Fernandez, J. Gil-Rostra, C. Escudero, I.J. Villar-Garcia, F. Yubero, A. D. Consuegra, A.R. Gonzalez-Elipe, Active sites and optimization of mixed copper-cobalt oxide anodes for anion exchange membrane water electrolysis, J. Power Sources 485 (2021), 229217.
[107] D. Chanda, J. Hnat, T. Bystron, M. Paidar, K. Bouzek, Optimization of synthesis of the nickel-cobalt oxide based anode electrocatalyst and of the related membrane-electrode assembly for alkaline water electrolysis, J. Power Sources 347 (2017) 247–258.
[108] P. Thangavel, G. Kim, K.S Kim, Electrochemical integration of amorphous NiFe (oxy)hydroxides on surface-activated carbon fibers for high-efficiency oxygen evolution in alkaline anion exchange membrane water electrolysis, J Mater Chem A 9 (2021) 14043–14051.
[109] Y. Wang, Y. Zou, L. Tao, Y. Wang, G. Huang, S. Du, S. Wang, Rational design of three-phase interfaces for electrocatalysis, Nano Res 12 (2019) 2055–2066.
[110] J.K. Lee, A. Bazylak, Optimizing Porous Transport Layer Design Parameters via Stochastic Pore Network Modelling: Reactant Transport and Interfacial Contact Considerations, J. Electrochem. Soc. 167 (2020), 013541.
[111] J. Lopata, Z. Kang, J. Young, G. Bender, J.W. Weidner, S. Shimpalee, Effects of the Transport/Catalyst Layer Interface and Catalyst Loading on Mass and Charge Transport Phenomena in Polymer Electrolyte Membrane Water Electrolysis Devices, J. Electrochem. Soc. 167 (2020), 064507.
[112] Z. Kang, Y. Chen, H. Wang, S.M. Alia, B.S. Pivovar, G. Bender, Discovering and Demonstrating a Novel High-Performing 2D-Patterned Electrode for Proton-Exchange Membrane Water Electrolysis Devices, Acs Appl Mater Inter 14 (2022) 2335–2342.
[113] A. Ozden, S. Shahgaldi, X. Li, F. Hamdullahpur, A review of gas diffusion layers for proton exchange membrane fuel cells—With a focus on characteristics, characterization techniques, materials and designs, Prog Energ Combust 74 (2019) 50–102.
[114] R. Omrani, B. Shabani, Gas diffusion layer modifications and treatments for improving the performance of proton exchange membrane fuel cells and electrolysers: A review, Int. J. Hydrog. Energy 42 (2017) 28515–28536.
[115] S.M. Steen, J.K. Mo, Z.Y. Kang, G.Q. Yang, F.Y. Zhang, Investigation of titanium liquid/gas diffusion layers in proton exchange membrane electrolyzer cells, Int J Green Energy 14 (2017) 162–170.
[116] L. Chen, X. Feng, Enhanced catalytic reaction at an air-liquid-solid triphase interface, Chem Sci 11 (2020) 3124–3131.
[117] H. Zhang, G.Q. Shen, X.Y. Liu, B. Ning, C.X. Shi, L. Pan, X.W. Zhang, Z.F. Huang, J.J. Zou, Self-supporting NiFe LDH-MoS_x integrated electrode for highly efficient water splitting at the industrial electrolysis conditions, Chinese J Catal 42 (2021) 1732–1741.
[118] A. Kiessling, J.C. Fornaciari, G. Anderson, X. Peng, A. Gerstmayr, M.R. Gerhardt, S. McKinney, A. Serov, Y.S. Kim, B. Zulevi, et al., Influence of Supporting Electrolyte on Hydroxide Exchange Membrane Water Electrolysis Performance: Anolyte, J. Electrochem. Soc. 168 (2021), 084512.
[119] J.F. Lutsko, M.A. Duran-Olivencia, Classical nucleation theory from a dynamical approach to nucleation, J Chem Phys 138 (2013), 244908.
[120] F. Razmjooei, A. Farooqui, R. Reissner, A.S. Gago, S.A. Ansar, K.A. Friedrich, Elucidating the Performance Limitations of Alkaline Electrolyte Membrane Electrolysis: Dominance of Anion Concentration in Membrane Electrode Assembly, Chemelectrochem 7 (2020) 3951–3960.
[121] D. Niblett, A. Mularczyk, V. Niasar, J. Eller, S. Holmes, Two-phase flow dynamics in a gas diffusion layer - gas channel - microporous layer system, J. Power Sources 471 (2020), 228427.
[122] A. Nouri-Khorasani, E.T. Ojong, T. Smolinka, D.P. Wilkinson, Model of oxygen bubbles and performance impact in the porous transport layer of PEM water electrolysis cells, Int. J. Hydrog. Energy 42 (2017) 28665–28680.
[123] F. Yang, M.J. Kim, M. Brown, B.J. Wiley, Alkaline Water Electrolysis at 25 A cm^{-2} with a Microfibrous Flow-through Electrode, Adv Energy Mater 10 (2020), 2001174.
[124] Z. Kang, J. Mo, G. Yang, S.T. Retterer, D.A. Cullen, T.J. Toops, J.B. Green Jr, M. M. Mench, F.-Y Zhang, Investigation of thin/well-tunable liquid/gas diffusion layers exhibiting superior multifunctional performance in low-temperature electrolytic water splitting, Energ Environ Sci 10 (2017) 166–175.
[125] P. Lettenmeier, S. Kolb, N. Sata, A. Fallisch, L. Zielke, S. Thiele, A.S. Gago, K. A. Friedrich, Comprehensive investigation of novel pore-graded gas diffusion layers for high-performance and cost-effective proton exchange membrane electrolyzers, Energ Environ Sci 10 (2017) 2521–2533.
[126] M.A. Hoeh, T. Arlt, I. Manke, J. Banhart, D.L. Fritz, W. Maier, W. Lehnert, In operando synchrotron X-ray radiography studies of polymer electrolyte membrane water electrolyzers, Electrochem. Commun. 55 (2015) 55–59.
[127] Y.F. Li, Z.Y. Kang, J.K. Mo, G.Q. Yang, S.L. Yu, D.A. Talley, B. Han, F.Y. Zhang, In-situ investigation of bubble dynamics and two-phase flow in proton exchange membrane electrolyzer cells, Int. J. Hydrog. Energy 43 (2018) 11223–11233.
[128] J.K. Mo, Z.Y. Kang, G.Q. Yang, D. Talley, W. Barnhill, F.Y. Zhang, D. Talley, Visualization on Rapid and Micro-Scale Dynamics of Oxygen Bubble Evolution in PEMECs, in: 2017 IEEE Int Conf Nano Micro, 2017, pp. 101–105.
[129] S.A. Grigoriev, P. Millet, S.A. Volobuev, V.N. Fateev, Optimization of porous current collectors for PEM water electrolysers, Int. J. Hydrog. Energy 34 (2009) 4968–4973.
[130] H. Ito, T. Maeda, A. Nakano, A. Kato, T. Yoshida, Influence of pore structural properties of current collectors on the performance of proton exchange membrane electrolyzer, Electrochim Acta 100 (2013) 242–248.
[131] G. Lin, S. Liu, G. Qu, Y. Song, T. Li, F. Liu, Y. Hu, Effect of pore size distribution in the gas diffusion layer adjusted by composite carbon black on fuel cell performance, Int J Energ Res 45 (2020) 7689–7702.
[132] Q. Xu, S.Z. Oener, G. Lindquist, H. Jiang, C. Li, S.W. Boettcher, Integrated Reference Electrodes in Anion-Exchange-Membrane Electrolyzers: Impact of Stainless-Steel Gas-Diffusion Layers and Internal Mechanical Pressure, Acs Energy Lett 6 (2021) 305–312.
[133] S. Paliwal, D. Panda, S. Bhaskaran, N. Vorhauer-Huget, E. Tsotsas, V.K. Surasani, Lattice Boltzmann method to study the water-oxygen distributions in porous transport layer (PTL) of polymer electrolyte membrane (PEM) electrolyser, Int. J. Hydrog. Energy 46 (2021) 22747–22762.
[134] F. Razmjooei, T. Morawietz, E. Taghizadeh, E. Hadjixenophontos, L. Mues, M. Gerle, B.D. Wood, C. Harms, A.S. Gago, S.A. Ansar, et al., Increasing the performance of an anion-exchange membrane electrolyzer operating in pure water with a nickel-based microporous layer, Joule 5 (2021) 1776–1799.

This work provided some insights to develop high efficient liquid/gas-diffusion layer for pure-water AEM electrolysis

[135] T. Schuler, J.M. Ciccone, B. Krentscher, F. Marone, C. Peter, T.J. Schmidt, F. N. Büchi, Hierarchically Structured Porous Transport Layers for Polymer Electrolyte Water Electrolysis, Adv Energy Mater 10 (2019), 1903216.
[136] S. Stiber, N. Sata, T. Morawietz, S.A. Ansar, T. Jahnke, J.K. Lee, A. Bazylak, A. Fallisch, A.S. Gago, K.A. Friedrich, A high-performance, durable and low-cost proton exchange membrane electrolyser with stainless steel components, Energ Environ Sci 15 (2022) 109–122.
[137] D. Kulkarni, A. Huynh, P. Satjaritanun, M. O'Brien, S. Shimpalee, D. Parkinson, P. Shevchenko, F. DeCarlo, N. Danilovic, K.E. Ayers, et al., Elucidating effects of catalyst loadings and porous transport layer morphologies on operation of proton exchange membrane water electrolyzers, Appl Catal B-Environ 308 (2022), 121213.
[138] C.C. Sung, C.Y. Liu, A novel micro protective layer applied on a simplified PEM water electrolyser, Int. J. Hydrog. Energy 38 (2013) 10063–10067.
[139] C.Y. Liu, L.H. Hu, C.C. Sung, Micro-protective layer for lifetime extension of solid polymer electrolyte water electrolysis, J. Power Sources 207 (2012) 81–85.
[140] Z.Y. Kang, G.Q. Yang, J.K. Mo, S.L. Yu, D.A. Cullen, S.T. Retterer, T.J. Toops, M. P. Brady, G. Bender, B.S. Pivovar, et al., Developing titanium micro/nano porous layers on planar thin/tunable LGDLs for high-efficiency hydrogen production, Int. J. Hydrog. Energy 43 (2018) 14618–14628.
[141] H. Rabiee, L. Ge, X. Zhang, S. Hu, M. Li, Z. Yuan, Gas diffusion electrodes (GDEs) for electrochemical reduction of carbon dioxide, carbon monoxide, and dinitrogen to value-added products: a review, Energ Environ Sci 14 (2021) 1959–2008.
[142] Z. Kang, J. Mo, G. Yang, Y. Li, D.A. Talley, S.T. Retterer, D.A. Cullen, T.J. Toops, M.P. Brady, G. Bender, et al., Thin film surface modifications of thin/tunable liquid/gas diffusion layers for high-efficiency proton exchange membrane electrolyzer cells, Anal. Energy 206 (2017) 983–990.
[143] P. Lettenmeier, S. Kolb, F. Burggraf, A.S. Gago, K.A. Friedrich, Towards developing a backing layer for proton exchange membrane electrolyzers, J. Power Sources 311 (2016) 153–158.
[144] E. Leonard, A.D. Shum, N. Danilovic, C. Capuano, K.E. Ayers, L.M. Pant, A. Z. Weber, X. Xiao, D.Y. Parkinson, I.V. Zenyuk, Interfacial analysis of a PEM electrolyzer using X-ray computed tomography, Sust. Energ. Fuels 4 (2020) 921–931.
[145] T. Bystron, M. Vesely, M. Paidar, G. Papakonstantinou, K. Sundmacher, B. Bensmann, R. Hanke-Rauschenbach, K. Bouzek, Enhancing PEM water electrolysis efficiency by reducing the extent of Ti gas diffusion layer passivation, J Appl Electrochem 48 (2018) 713–723.
[146] Z.Y. Kang, S.M. Alia, J.L. Young, G. Bender, Effects of various parameters of different porous transport layers in proton exchange membrane water electrolysis, Electrochim Acta 354 (2020), 136641.

[147] M. Suermann, T. Gimpel, L.V. Buhre, W. Schade, B. Bensmann, R. Hanke-Rauschenbach, Femtosecond laser-induced surface structuring of the porous transport layers in proton exchange membrane water electrolysis, J Mater Chem A 8 (2020) 4898–4910.

[148] KNF Group. https://knf.com/en/us/solutions/pumps/series/diaphragm-liquid-pump-unf-125, (2022).

[149] X.Y. Yan, J. Biemolt, K. Zhao, Y. Zhao, X.J. Cao, Y. Yang, X.Y. Wu, G. Rothenberg, N. Yan, A membrane-free flow electrolyzer operating at high current density using earth-abundant catalysts for water splitting, Nat. Commun. 12 (2021) 4143.

[150] Dioxide Materials, electrolyzer handware. https://dioxidematerials.com/product/research-grade-5-cm2-aem-water-electrolyzer-hardware, (2022).

[151] A.S. Gago, A.S. Ansar, P. Gazdzicki, N. Wagner, J. Arnold, K.A. Friedrich, Low Cost Bipolar Plates for Large Scale PEM Electrolyzers, ECS Trans 64 (2014) 1039–1048.

[152] G.A. Lindquist, S.Z. Oener, R. Krivina, A.R. Motz, A. Keane, C. Capuano, K. E. Ayers, S.W. Boettcher, Performance and Durability of Pure-Water-Fed Anion Exchange Membrane Electrolyzers Using Baseline Materials and Operation, ACS Applied Materials & Interfaces 13 (2021) 51917–51924.

[153] K.E. Ayers, C. Capuano, E.B. Anderson, Recent Advances in Cell Cost and Efficiency for PEM-Based Water Electrolysis, ECS Trans 41 (2012) 15–22.

[154] H.Y. Jung, S.Y. Huang, P. Ganesan, B.N. Popov, Performance of gold-coated titanium bipolar plates in unitized regenerative fuel cell operation, J. Power Sources 194 (2009) 972–975.

[155] P. Millet, S.A. Grigoriev, V.I. Porembskiy, Development and characterisation of a pressurized PEM bi-stack electrolyser, Int J Energ Res 37 (2013) 449–456.

[156] C. Minnaar, F. De Beer, D. Bessarabov, Current Density Distribution of Electrolyzer Flow Fields: In Situ Current Mapping and Neutron Radiography, Energ Fuel 34 (2020) 1014–1023.

[157] S. Toghyani, E. Afshari, E. Baniasadi, S.A. Atyabi, Thermal and electrochemical analysis of different flow field patterns in a PEM electrolyzer, Electrochim Acta 267 (2018) 234–245.

[158] J.O. Majasan, J.I.S. Cho, I. Dedigama, D. Tsaoulidis, P. Shearing, D.J.L Brett, Two-phase flow behaviour and performance of polymer electrolyte membrane electrolysers: Electrochemical and optical characterisation, Int. J. Hydrog. Energy 43 (2018) 15659–15672.

[159] G. Chisholm, P.J. Kitson, N.D. Kirkaldy, L.G. Bloor, L. Cronin, 3D printed flow plates for the electrolysis of water: an economic and adaptable approach to device manufacture, Energ Environ Sci 7 (2014) 3026–3032.

[160] O.F. Selamet, M.C. Acar, M.D. Mat, Y. Kaplan, Effects of operating parameters on the performance of a high-pressure proton exchange membrane electrolyzer, Int J Energ Res 37 (2013) 457–467.

[161] H. Li, H. Nakajima, A. Inada, K. Ito, Effect of flow-field pattern and flow configuration on the performance of a polymer-electrolyte-membrane water electrolyzer at high temperature, Int. J. Hydrog. Energy 43 (2018) 8600–8610.

[162] S. Asghari, M.H. Shahsamandi, M.R.A. Khorasani, Design and manufacturing of end plates of a 5 kW PEM fuel cell, Int. J. Hydrog. Energy 35 (2010) 9291–9297.

[163] L. Chen, H.-B. Luan, W.-Q. Tao, Liquid Water Dynamic Behaviors in the Gdl and Gc of Pemfcs Using Lattice Boltzmann Method. *Front*, Heat Mass Transf 1 (2010), 023002.

[164] Sono-Tek Corporation. https://www.sono-tek.com/products/, (2022).

[165] R. Fernandez, P. Ferreira-Aparicio, L. Daza, PEMFC electrode preparation: Influence of the solvent composition and evaporation rate on the catalytic layer microstructure, J. Power Sources 151 (2005) 18–24.

[166] B. Britton, S. Holdcroft, The Control and Effect of Pore Size Distribution in AEMFC Catalyst Layers, J. Electrochem. Soc. 163 (2016) F353–F358.

[167] S. Cho, K. Tamoto, M. Uchida, Effect of an Electrospray-Generated Ionomer Morphology on Polymer Electrolyte Fuel Cell Performance, Energ Fuel 34 (2020) 14853–14863.

[168] A.Y. Faid, L. Xie, A.O. Barnett, F. Seland, D. Kirk, S. Sunde, Effect of anion exchange ionomer content on electrode performance in AEM water electrolysis, Int. J. Hydrog. Energy 45 (2020) 28272–28284.

[169] E. Cossar, A.O. Barnett, F. Seland, R. Safari, G.A. Botton, E.A. Baranova, Ionomer content optimization in nickel-iron-based anodes with and without ceria for anion exchange membrane water electrolysis, J. Power Sources 514 (2021), 230563.

[170] B.A.W. Mowbray, D.J. Dvorak, N. Taherimakhsousi, C.P. Berlinguette, How Catalyst Dispersion Solvents Affect CO_2 Electrolyzer Gas Diffusion Electrodes, Energ Fuel 35 (2021) 19178–19184.

[171] W. Ju, M. Heinz, D. Burnat, C. Battaglia, U.F. Vogt, Alkaline water electrolysis: membrane development & characterization, in: ICE2017, Copenhagen, 2017https://www.ice2017.net/-/media/sites/ice2017/uploads/ice2017_205_vogt.pdf.

[172] Enapter, EL 500. https://www.enapter.com/app/uploads/Enapter_whitepaper.pdf, (2022).

[173] A. Lim, M.K. Cho, S.Y. Lee, H.J. Kim, S.J. Yoo, Y.E. Sung, J.H. Jang, H.S. Park, A Review of Industrially Developed Components and Operation Conditions for Anion Exchange Membrane Water Electrolysis, J Electrochem Sci Te 8 (2017) 265–273.

[174] C.C. Pavel, F. Cecconi, C. Emiliani, S. Santiccioli, A. Scaffidi, S. Catanorchi, M. Comotti, Highly efficient platinum group metal free based membrane-electrode assembly for anion exchange membrane water electrolysis, Angew Chem Int Edit 53 (2014) 1378–1381.

[175] G. Gardner, J. Al-Sharab, N. Danilovic, Y.B. Go, K. Ayers, M. Greenblatt, G. C. Dismukes, Structural basis for differing electrocatalytic water oxidation by the cubic, layered and spinel forms of lithium cobalt oxides, Energ Environ Sci 9 (2016) 184–192.

[176] N. Lin, J. Zausch, 1D multiphysics modelling of PEM water electrolysis anodes with porous transport layers and the membrane, Chem. Eng. Sci. 253 (2022), 117600.

[177] A. Meena, P. Thangavel, D.S. Jeong, A.N. Singh, A. Jana, H. Im, D.A. Nguyen, K. S. Kim, Crystalline-amorphous interface of mesoporous Ni_2P@ $FePO_xH_y$ for oxygen evolution at high current density in alkaline-anion-exchange-membrane water-electrolyzer, Appl Catal B-Environ (2022), 121127.

[178] C.V. Pham, D. Escalera-López, K. Mayrhofer, S. Cherevko, S. Thiele, Essentials of High Performance Water Electrolyzers–From Catalyst Layer Materials to Electrode Engineering, Adv Energy Mater 11 (2021), 2101998.

[179] P. Holzapfel, M. Buhler, C.V. Pham, F. Hegge, T. Bohm, D. McLaughlin, M. Breitwieser, S. Thiele, Directly coated membrane electrode assemblies for proton exchange membrane water electrolysis, Electrochem. Commun. 110 (2020), 106640.

[180] S. Thanasilp, M. Hunsom, Effect of MEA fabrication techniques on the cell performance of Pt-Pd/C electrocatalyst for oxygen reduction in PEM fuel cell, Fuel 89 (2010) 3847–3852.

[181] B. Bladergroen, H. Su, S. Pasupathi, V. Linkov, Overview of membrane electrode assembly preparation methods for solid polymer electrolyte electrolyzer, InTech (2012).

[182] J. Hnát, M. Plevova, R.A. Tufa, J. Zitka, M. Paidar, K. Bouzek, Development and testing of a novel catalyst-coated membrane with platinum-free catalysts for alkaline water electrolysis, Int. J. Hydrog. Energy 44 (2019) 17493–17504.

[183] M. Stähler, A. Stähler, F. Scheepers, M. Carmo, D. Stolten, A completely slot die coated membrane electrode assembly, Int. J. Hydrog. Energy 44 (2019) 7053–7058.

[184] M. Chen, C. Zhao, F. Sun, J. Fan, H. Li, H. Wang, Research progress of catalyst layer and interlayer interface structures in membrane electrode assembly (MEA) for proton exchange membrane fuel cell (PEMFC) system, Etransportation 5 (2020), 100075.

[185] F. Hegge, F. Lombeck, E. Cruz Ortiz, L. Bohn, M. von Holst, M. Kroschel, J. Hübner, M. Breitwieser, P. Strasser, S. Vierrath, Efficient and Stable Low Iridium Loaded Anodes for PEM Water Electrolysis Made Possible by Nanofiber Interlayers, Acs Appl Energ Mater 3 (2020) 8276–8284.

[186] G. Jiang, H. Yu, Y. Li, D. Yao, J. Chi, S. Sun, Z. Shao, Low-Loading and Highly Stable Membrane Electrode Based on an Ir@WO_xNR Ordered Array for PEM Water Electrolysis, Acs Appl Mater Inter 13 (2021) 15073–15082.

[187] L. Wan, Z. Xu, Q. Xu, P. Wang, B. Wang, Overall design of novel 3D-ordered MEA with drastically enhanced mass transport for alkaline electrolyzers, Energ Environ Sci 15 (2022) 1882–1892.

[188] Z. Xie, T. Navessin, K. Shi, R. Chow, Q. Wang, D. Song, B. Andreaus, M. Eikerling, Z. Liu, S. Holdcroft, Functionally graded cathode catalyst layers for polymer electrolyte fuel cells: II. Experimental study of the effect of nafion distribution, J. Electrochem. Soc. 152 (2005) A1171.

[189] A.D. Taylor, E.Y. Kim, V.P. Humes, J. Kizuka, L.T. Thompson, Inkjet printing of carbon supported platinum 3-D catalyst layers for use in fuel cells, J. Power Sources 171 (2007) 101–106.

[190] Y. Qiu, H. Zhang, H. Zhong, F. Zhang, A novel cathode structure with double catalyst layers and low Pt loading for proton exchange membrane fuel cells, Int. J. Hydrog. Energy 38 (2013) 5836–5844.

[191] L. Wan, J. Liu, Z. Xu, Q. Xu, M. Pang, P. Wang, B. Wang, Construction of Integrated Electrodes with Transport Highways for Pure-Water-Fed Anion Exchange Membrane Water Electrolysis, Small (2022), 2200380.

[192] M.K. Debe, Tutorial on the Fundamental Characteristics and Practical Properties of Nanostructured Thin Film (NSTF) Catalysts, J. Electrochem. Soc. 160 (2013) F522–F534.

[193] F. Tassinari, K. Banerjee-Ghosh, F. Parenti, V. Kiran, A. Mucci, R Naaman, Enhanced hydrogen production with chiral conductive polymer-based electrodes, J. Phys. Chem. C 121 (2017) 15777–15783.

[194] E. Detsi, J.B. Cook, B.K. Lesel, C.L. Turner, Y.-L. Liang, S. Robbennolt, S. H. Tolbert, Mesoporous $Ni_{60}Fe_{30}Mn_{10}$-alloy based metal/metal oxide composite thick films as highly active and robust oxygen evolution catalysts, Energ Environ Sci 9 (2016) 540–549.

[195] K. Nagasawa, T. Ishida, H. Kashiwagi, Y. Sano, S. Mitsushima, Design and characterization of compact proton exchange membrane water electrolyzer for component evaluation test, Int. J. Hydrog. Energy 46 (2021) 36619–36628.

[196] T. Yigit, O.F. Selamet, Mathematical modeling and dynamic Simulink simulation of high-pressure PEM electrolyzer system, Int. J. Hydrog. Energy 41 (2016) 13901–13914.

[197] S. Al Shakhshir, F. Zhou, S.K. Kær, On the Effect of Clamping Pressure and Methods on the Current Distribution of a Proton Exchange Membrane Water Electrolyzer, ECS Trans 85 (2018) 995.

[198] I. Vincent, D. Bessarabov, Low cost hydrogen production by anion exchange membrane electrolysis: A review, Renew. Sust. Energ. Rev. 81 (2018) 1690–1704.

[199] N. Chen, S.Y. Paek, J.Y. Lee, J.H. Park, S.Y. Lee, Y.M. Lee, High-performance anion exchange membrane water electrolyzers with a current density of 7.68 A cm^{-2} and a durability of 1000 hours, Energ Environ Sci 14 (2021) 6338–6348.

[200] FSEC s Procedures For Performing PEM Single Cell Testing, US Department of Energy, Arlington, Virginia, 2009.

[201] A. Lim, H.-j. Kim, D. Henkensmeier, S. Jong Yoo, J. Young Kim, S. Young Lee, Y.-E. Sung, J.H. Jang, H.S. Park, A study on electrode fabrication and operation variables affecting the performance of anion exchange membrane water electrolysis, J Ind. Eng. Chem. 76 (2019) 410–418.

[202] J.E. Park, S.Y. Kang, S.-H. Oh, J.K. Kim, M.S. Lim, C.-Y. Ahn, Y.-H. Cho, Y.-E. Sung, High-performance anion-exchange membrane water electrolysis, Electrochim Acta 295 (2019) 99–106.

[203] H. Ito, N. Kawaguchi, S. Someya, T. Munakata, Pressurized operation of anion exchange membrane water electrolysis, Electrochim Acta 297 (2019) 188–196.
[204] H. Ito, N. Miyazaki, M. Ishida, A. Nakano, Stack Performance of Proton Exchange Membrane Based Unitized Reversible Fuel Cells, Int. J. Microgravity Sci. Appl. 33 (2016), 330305.
[205] Ayers, K., Capuano, C., Atanassov, P., Mukerjee, S., Hickner, M. High performance platinum group metal free membrane electrode assemblies through control of interfacial processes. Proton Energy Systems, Wallingford, CT (United States), 2017.
[206] J. Liu, Z. Kang, D. Li, M. Pak, S.M. Alia, C. Fujimoto, G. Bender, Y.S. Kim, A. Z. Weber, Elucidating the role of hydroxide electrolyte on anion-exchange-membrane water electrolyzer performance, J. Electrochem. Soc. 168 (2021), 054522.
[207] D. Li, A.R. Motz, C. Bae, C. Fujimoto, G. Yang, F.-Y. Zhang, K.E. Ayers, Y.S. Kim, Durability of anion exchange membrane water electrolyzers, Energ Environ Sci 14 (2021) 3393–3419.
[208] H. Ito, N. Kawaguchi, S. Someya, T. Munakata, N. Miyazaki, M. Ishida, A. Nakano, Experimental investigation of electrolytic solution for anion exchange membrane water electrolysis, Int. J. Hydrog. Energy 43 (2018) 17030–17039.
[209] S. Dresp, T. Ngo Thanh, M. Klingenhof, S. Brückner, P. Hauke, P. Strasser, Efficient direct seawater electrolysers using selective alkaline NiFe-LDH as OER catalyst in asymmetric electrolyte feeds, Energ Environ Sci 13 (2020) 1725–1729.

This work provided some insights about the direct seawater electrolysis

[210] P. Thangavel, M. Ha, S. Kumaraguru, A. Meena, A.N. Singh, A.M. Harzandi, K. S. Kim, Graphene-nanoplatelets-supported NiFe-MOF: high-efficiency and ultra-stable oxygen electrodes for sustained alkaline anion exchange membrane water electrolysis, Energ Environ Sci 13 (2020) 3447–3458.
[211] M.K. Cho, H.-Y. Park, H.J. Lee, H.-J. Kim, A. Lim, D. Henkensmeier, S.J. Yoo, J. Y. Kim, S.Y. Lee, H.S. Park, Alkaline anion exchange membrane water electrolysis: Effects of electrolyte feed method and electrode binder content, J. Power Sources 382 (2018) 22–29.
[212] A. Xie, S.C. Popat, Electrochemical ammonia stripping from non-nitrified animal rendering wastewater, ECS Meet, Abs 3 (2020). MA2021-2002 1532.
[213] A.K. Niaz, A. Akhtar, J.-Y. Park, H.-T. Lim, Effects of the operation mode on the degradation behavior of anion exchange membrane water electrolyzers, J. Power Sources 481 (2021), 229093.
[214] L.N. Stanislaw, M.R. Gerhardt, A.Z. Weber, Modeling electrolyte composition effects on anion-exchange-membrane water electrolyzer performance, ECS Trans 92 (2019) 767.
[215] M. Yu, J. Li, F. Liu, J. Liu, W. Xu, H. Hu, X. Chen, W. Wang, F. Cheng, Anionic formulation of electrolyte additive towards stable electrocatalytic oxygen evolution in seawater splitting, J. Energy Chem. 72 (2022) 361–369.
[216] N. Agmon, The Grotthuss mechanism, Chem. Phys. Lett. 244 (1995) 456–462.
[217] C. Chen, Y.-L.S. Tse, G.E. Lindberg, C. Knight, G.A. Voth, Hydroxide Solvation and Transport in Anion Exchange Membranes, J Am Chem Soc 138 (2016) 991–1000.
[218] J.O. Majasan, F. Iacoviello, P.R. Shearing, D.J. Brett, Effect of microstructure of porous transport layer on performance in polymer electrolyte membrane water electrolyser, Energy Procedia 151 (2018) 111–119.
[219] K.J. Choi, H. Kim, S.-K. Kim, Multicomponent nonprecious hydrogen evolution catalysts for high performance and durable proton exchange membrane water electrolyzer, J. Power Sources 506 (2021), 230200.
[220] L.A. Diaz, J. Hnát, N. Heredia, M.M. Bruno, F.A. Viva, M. Paidar, H.R. Corti, K. Bouzek, G.C. Abuin, Alkali doped poly (2, 5-benzimidazole) membrane for alkaline water electrolysis: Characterization and performance, J. Power Sources 312 (2016) 128–136.
[221] B. Mayerhöfer, K. Ehelebe, F.D. Speck, M. Bierling, J. Bender, J.A. Kerres, K. J. Mayrhofer, S. Cherevko, R. Peach, S Thiele, On the effect of anion exchange ionomer binders in bipolar electrode membrane interface water electrolysis, J Mater Chem A 9 (2021) 14285–14295.
[222] C.G. Arges, V. Ramani, Two-dimensional NMR spectroscopy reveals cation-triggered backbone degradation in polysulfone-based anion exchange membranes, P Natl Acad Sci USA 110 (2013) 2490–2495.
[223] A.D. Mohanty, S.E. Tignor, J.A. Krause, Y.-K. Choe, C. Bae, Systematic Alkaline Stability Study of Polymer Backbones for Anion Exchange Membrane Applications, Macromolecules 49 (2016) 3361–3372.
[224] S. Vengatesan, S. Santhi, S. Jeevanantham, G. Sozhan, Quaternized poly (styrene-co-vinylbenzyl chloride) anion exchange membranes for alkaline water electrolysers, J. Power Sources 284 (2015) 361–368.
[225] R. Soni, S. Miyanishi, H. Kuroki, T. Yamaguchi, Pure Water Solid Alkaline Water Electrolyzer Using Fully Aromatic and High-Molecular-Weight Poly(fluorene-alt-tetrafluorophenylene)-trimethyl Ammonium Anion Exchange Membranes and Ionomers, Acs Appl Energ Mater 4 (2021) 1053–1058.
[226] J.W. Xiao, A.M. Oliveira, L. Wang, Y. Zhao, T. Wang, J.H. Wang, B.P. Setzler, Y. S. Yan, Water-Fed Hydroxide Exchange Membrane Electrolyzer Enabled by a Fluoride-Incorporated Nickel-Iron Oxyhydroxide Oxygen Evolution Electrode, Acs Catal 11 (2021) 264–270.
[227] E. Cossar, A. Oyarce Barnett, F. Seland, E.A. Baranova, The performance of nickel and nickel-iron catalysts evaluated as anodes in anion exchange membrane water electrolysis, Catalysts 9 (2019) 814.
[228] B.J. Kim, X. Cheng, D.F. Abbott, E. Fabbri, F. Bozza, T. Graule, I.E. Castelli, L. Wiles, N. Danilovic, K.E. Ayers, Highly active nanoperovskite catalysts for oxygen evolution reaction: Insights into activity and stability of $Ba_{0.5}Sr_{0.5}Co_{0.8}Fe_{0.2}O_{2+\delta}$ and $PrBaCo_2O_{5+\delta}$, Adv Funct Mater 28 (2018), 1804355.
[229] D. Henkensmeier, M. Najibah, C. Harms, J. Žitka, J. Hnát, K. Bouzek, Overview: State-of-the art commercial membranes for anion exchange membrane water electrolysis, J. Electrochem. Energy Convers. Storage 18 (2021), 024001.
[230] S.Y. Kang, J.E. Park, G.Y. Jang, O.-H. Kim, O.J. Kwon, Y.-H. Cho, Y.-E. Sung, High-performance and durable water electrolysis using a highly conductive and stable anion-exchange membrane, Int. J. Hydrog. Energy (2022) 9115–9126.
[231] R.A. Krivina, Y. Ou, Q. Xu, L.P. Twight, T.N. Stovall, S.W. Boettcher, Oxygen electrocatalysis on mixed-metal oxides/oxyhydroxides: From fundamentals to membrane electrolyzer technology, Acc. Chem. Res. 2 (2021) 548–558.
[232] E. López-Fernández, C.G. Sacedón, J. Gil-Rostra, F. Yubero, A.R. González-Elipe, A. de Lucas-Consuegra, Recent Advances in Alkaline Exchange Membrane Water Electrolysis and Electrode Manufacturing, Molecules 26 (2021) 6326.
[233] J.J. Kaczur, H. Yang, Z. Liu, S.D. Sajjad, R.I. Masel, Carbon dioxide and water electrolysis using new alkaline stable anion membranes, Front Chem 6 (2018) 263.
[234] B. Motealleh, Z. Liu, R.I. Masel, J.P. Sculley, Z. Richard Ni, L. Meroueh, Next-generation anion exchange membrane water electrolyzers operating for commercially relevant lifetimes, Int. J. Hydrog. Energy 46 (2021) 3379–3386.
[235] E.T. Ojong, J.T.H. Kwan, A. Nouri-Khorasani, A. Bonakdarpour, D.P. Wilkinson, T. Smolinka, Development of an experimentally validated semi-empirical fully-coupled performance model of a PEM electrolysis cell with a 3-D structured porous transport layer, Int. J. Hydrog. Energy 42 (2017) 25831–25847.
[236] M.K. Cho, H.-Y. Park, S. Choe, S.J. Yoo, J.Y. Kim, H.-J. Kim, D. Henkensmeier, S. Y. Lee, Y.-E. Sung, H.S. Park, Factors in electrode fabrication for performance enhancement of anion exchange membrane water electrolysis, J. Power Sources 347 (2017) 283–290.
[237] T. Malkow, A. Pilenga, G. Tsotridis, EU harmonised test procedure: electrochemical impedance spectroscopy for water electrolysis cells, Publications Office of the European Union, 2018.
[238] T. Audichon, E. Mayousse, S. Morisset, C. Morais, C. Comminges, T.W. Napporn, K.B. Kokoh, Electroactivity of RuO_2–IrO_2 mixed nanocatalysts toward the oxygen evolution reaction in a water electrolyzer supplied by a solar profile, Int. J. Hydrog. Energy 39 (2014) 16785–16796.
[239] J. Wei, M. Zhou, A. Long, Y. Xue, H. Liao, C. Wei, Z.J. Xu, Heterostructured electrocatalysts for hydrogen evolution reaction under alkaline conditions, Nanomicro Lett 10 (2018) 1–15.
[240] S. Siracusano, S. Trocino, N. Briguglio, V. Baglio, A.S. Aricò, Electrochemical impedance spectroscopy as a diagnostic tool in polymer electrolyte membrane electrolysis, Materials 11 (2018) 1368.
[241] M. Maier, K. Smith, J. Dodwell, G. Hinds, P.R. Shearing, D.J.L. Brett, Mass transport in PEM water electrolysers: A review, Int. J. Hydrog. Energy 47 (2022) 30–56.
[242] G.A. Lindquist, Q. Xu, S.Z. Oener, S.W. Boettcher, Membrane electrolyzers for impure-water splitting, Joule 4 (2020) 2549–2561.

This work provided some perspectives for the impure-water electrolysis

[243] L. Xia, W. Jiang, H. Hartmann, J. Mayer, W. Lehnert, M. Shviro, Multistep Sulfur Leaching for the Development of a Highly Efficient and Stable $NiS_x/Ni(OH)_2$/NiOOH Electrocatalyst for Anion Exchange Membrane Water Electrolysis, Acs Appl Mater Inter 14 (2022) 19397–19408.
[244] S. Kang, K. Ham, J. Lee, Moderate oxophilic CoFe in carbon nanofiber for the oxygen evolution reaction in anion exchange membrane water electrolysis, Electrochim Acta 353 (2020), 136521.
[245] Y. Zhang, J. Parrondo, S. Sankarasubramanian, V. Ramani, Detection of reactive oxygen species in anion exchange membrane fuel cells using in situ fluorescence spectroscopy, ChemSusChem 10 (2017) 3056–3062.
[246] K.F.L. Hagesteijn, S. Jiang, B.P. Ladewig, A review of the synthesis and characterization of anion exchange membranes, J. Mater. Sci. 53 (2018) 11131–11150.
[247] J. Parrondo, Z. Wang, M.-S.J. Jung, V. Ramani, Reactive oxygen species accelerate degradation of anion exchange membranes based on polyphenylene oxide in alkaline environments, Phys. Chem. Chem. Phys. 18 (2016) 19705–19712.
[248] E.J. Park, S. Maurya, M.R. Hibbs, C.H. Fujimoto, K.-D. Kreuer, Y.S. Kim, Alkaline Stability of Quaternized Diels–Alder Polyphenylenes, Macromolecules 52 (2019) 5419–5428.
[249] R.A. Krivina, G.A. Lindquist, M.C. Yang, A.K. Cook, C.H. Hendon, A.R. Motz, C. Capuano, K.E. Ayers, J.E. Hutchison, S.W. Boettcher, Three-Electrode Study of Electrochemical Ionomer Degradation Relevant to Anion-Exchange-Membrane Water Electrolyzers, Acs Appl Mater Inter 14 (2022) 18261–18274.
[250] W. Tong, M. Forster, F. Dionigi, S. Dresp, R. Sadeghi Erami, P. Strasser, A. J. Cowan, P. Farràs, Electrolysis of low-grade and saline surface water, Nat. Energy 5 (2020) 367–377.
[251] P. Gayen, S. Saha, V. Ramani, Selective Seawater Splitting Using Pyrochlore Electrocatalyst, Acs Appl Energ Mater 3 (2020) 3978–3983.
[252] L.R. Czarnetzki, L.J.J Janssen, Formation of hypochlorite, chlorate and oxygen during NaCl electrolysis from alkaline solutions at an RuO_2/TiO_2 anode, J Appl Electrochem 22 (1992) 315–324.
[253] O. Kasian, S. Geiger, K.J. Mayrhofer, S. Cherevko, Electrochemical on-line ICP-MS in electrocatalysis research, Chem. Rec. 19 (2019) 2130–2142.
[254] J. Ampurdanés, M. Chourashiya, A. Urakawa, Cobalt oxide-based materials as non-PGM catalyst for HER in PEM electrolysis and in situ XAS characterization of its functional state, Catal.Today 336 (2019) 161–168.

[255] W. Wang, K. Li, L. Ding, S. Yu, Z. Xie, D.A. Cullen, H. Yu, G. Bender, Z. Kang, J. A. Wrubel, Exploring the Impacts of Conditioning on Proton Exchange Membrane Electrolyzers by In Situ Visualization and Electrochemistry Characterization, Acs Appl Mater Inter 14 (2022) 9002–9012.
[256] Z. Xu, L. Wan, Y. Liao, P. Wang, K. Liu, B Wang, Anisotropic anion exchange membranes with extremely high water uptake for water electrolysis and fuel cells, J Mater Chem A 9 (2021) 23485–23496.
[257] K. Ehelebe, J. Knöppel, M. Bierling, B. Mayerhöfer, T. Böhm, N. Kulyk, S. Thiele, K.J. Mayrhofer, S. Cherevko, Platinum dissolution in realistic fuel cell catalyst layers, Angew Chem Int Edit 133 (2021) 8964–8970.
[258] A.Y. Faid, A.O. Barnett, F. Seland, S. Sunde, Ni/NiO nanosheets for alkaline hydrogen evolution reaction: In situ electrochemical-Raman study, Electrochim Acta 361 (2020), 137040.
[259] E. López-Fernández, J. Gil-Rostra, J. Espinós, A. González-Elipe, A. de Lucas Consuegra, F. Yubero, Chemistry and electrocatalytic activity of nanostructured nickel electrodes for water electrolysis, Acs Catal 10 (2020) 6159–6170.
[260] C. Yang, G. Rousse, K. Louise Svane, P.E. Pearce, A.M. Abakumov, M. Deschamps, G. Cibin, A.V. Chadwick, D.A. Dalla Corte, Anton Hansen, H. Cation insertion to break the activity/stability relationship for highly active oxygen evolution reaction catalyst, Nat. Commun. 11 (2020) 1–10.
[261] M. Suermann, A. Pătru, T.J. Schmidt, F.N. Büchi, High pressure polymer electrolyte water electrolysis: Test bench development and electrochemical analysis, Int. J. Hydrog. Energy 42 (2017) 12076–12086.
[262] M.W. Fowler, R.F. Mann, J.C. Amphlett, B.A. Peppley, P.R. Roberge, Incorporation of voltage degradation into a generalised steady state electrochemical model for a PEM fuel cell, J. Power Sources 106 (2002) 274–283.
[263] S. Franz, H. Arab, G.L. Chiarello, M. Bestetti, E. Selli, Single-Step Preparation of Large Area TiO_2 Photoelectrodes for Water Splitting, Adv Energy Mater 10 (2020).
[264] J.E. Park, M.-J. Kim, M.S. Lim, S.Y. Kang, J.K. Kim, S.-H. Oh, M. Her, Y.-H. Cho, Y.-E. Sung, Graphitic carbon nitride-carbon nanofiber as oxygen catalyst in anion-exchange membrane water electrolyzer and rechargeable metal–air cells, Appl Catal B-Environ 237 (2018) 140–148.
[265] O. Toussi, White Paper: Hydrogen Production cost by AEM electrolysis, Ionomr Innovations Inc, 2021, pp. 1–12.
[266] E.L. Miller, S.T. Thompson, K. Randolph, Z. Hulvey, N. Rustagi, S. Satyapal, US Department of Energy hydrogen and fuel cell technologies perspectives, MRS Bulletin 45 (2020) 57–64.
[267] T. Ramsden, D. Steward, B. James, M. Reed, D. Allen, F. Joseck, Hydrogen Technology Analysis: H2A Production Model Update, National Renewable Energy Laboratory, 2007.
[268] S. Dresp, F. Dionigi, M. Klingenhof, P. Strasser, Direct Electrolytic Splitting of Seawater: Opportunities and Challenges, Acs Energy Lett 4 (2019) 933–942.
[269] D. Li, E.J. Park, W. Zhu, Q. Shi, Y. Zhou, H. Tian, Y. Lin, A. Serov, B. Zulevi, E. D. Baca, et al., Highly quaternized polystyrene ionomers for high performance anion exchange membrane water electrolysers, Nat. Energy 5 (2020) 378–385.
[270] R.A. Krivina, G.A. Lindquist, S.R. Beaudoin, T.N. Stovall, W.L. Thompson, L. P. Twight, D. Marsh, J. Grzyb, K. Fabrizio, J.E. Hutchison, et al., Anode Catalysts in Anion-Exchange-Membrane Electrolysis Without Supporting Electrolyte: Conductivity, Dynamics, and Ionomer Degradation, Adv Mater (2022), https://doi.org/10.1002/adma.202203033.
[271] X. Lu, C. Zhu, Z. Wu, J. Xuan, J.S. Francisco, H. Wang, In situ observation of the pH gradient near the gas diffusion electrode of CO_2 reduction in alkaline electrolyte, J Am Chem Soc 142 (2020) 15438–15444.
[272] L. An, T.S. Zhao, Z.H. Chai, P. Tan, L. Zeng, Mathematical modeling of an anion-exchange membrane water electrolyzer for hydrogen production, Int. J. Hydrog. Energy 39 (2014) 19869–19876.

Qiucheng Xu acquired his Ph.D. in materials science and engineering from the East China University of Science and Technology (supervised by Prof. Jiang and Prof. Li), and had a 1-year joint Ph.D. experience at the University of Oregon (supervised by Prof. Boettcher). He is currently a postdoctoral fellow in the Surface Physics and Catalysis (Surf Cat) Section, Technical University of Denmark. His research interests include the synthesis of novel electrode materials and the development of membrane-based electrochemical devices.

Liyue Zhang received her B.S. in composite materials and engineering from the East China University of Science and Technology (ECUST) in 2020. She is currently a Ph.D. candidate in materials science and engineering under the supervision of Prof. Hao Jiang at the ECUST. Her research focuses on the anion-exchange membrane-based water electrolysis.

Hao Jiang is a full professor of the Key Laboratory for Ultrafine Materials of Ministry of Education at the East China University of Science and Technology (ECUST). Prof. Jiang received his Ph.D. in materials science and engineering from the ECUST in 2009, and was also a postdoctoral fellow at the Temasek Laboratories, Nanyang Technological University (NTU) until 2011. His research interests mainly focus on the design and synthesis of nanomaterials in the application of electrochemical energy storage and conversion.

Chunzhong Li is a Cheung Kong Chair Professor at the East China University of Science and Technology (ECUST). He is also the dean of the School of Chemical Engineering at ECUST. Prof. Li received his B.S. (1989), M.S. (1992), and Ph.D. (1997) in chemical engineering from the ECUST. His research interests are highly interdisciplinary, including the accurate construction and application of nanoenergy materials, synthesis, and processing of polymer-based nanohybrids, and the chemical basis and scale-up of nanomaterials production.